ASSESSING TREATMENT RESPONSE OF HER2+ BREAST CANCER XENOGRAFTS WITH PET AND MRI

By

Jennifer Gray Whisenant

Dissertation

Submitted to the Faculty of the

Graduate School of Vanderbilt University

in partial fulfillment of the requirements

for the degree of

DOCTOR OF PHILOSOPHY

in

Chemical and Physical Biology

August, 2013

Nashville, Tennessee

Approved:

Professor Thomas E. Yankeelov

Professor John C. Gore

Professor J. Oliver McIntyre

Professor H. Charles Manning

Professor Todd E. Peterson

DEDICATION

I would like to dedicate this dissertation to my Granddaddy, JM Gilbert. He always inspired me to work hard and "get your degree". I truly wish you were here to share in this wonderful accomplishment. I know you are with me in spirit.

I also dedicate this dissertation in loving memory of my grandmother, Peggy Gilbert, and in honor of my great aunt, Betty Gray, who are both breast cancer survivors. You inspire and encourage me to continue the fight against cancer.

To Paul: Thank you for the much-needed support during the last few months. You definitely kept me from boarding the "insane train".

ACKNOWLEDGMENT

There are not enough words to express my gratitude for all of those that have helped me throughout my graduate training at Vanderbilt. I would first like to thank my family (dad, mom, Marilyn, and Ted), who were always there to support me, whether it was with encouraging words or much needed hugs. Thank you for believing in me and telling me through the rough times, “hang in there, you can do it!”

I would also like to thank my mentor, Tom. He definitely is one-of-a-kind. Thank you for your patience and understanding, and sharing your knowledge and expertise with me. I truly feel lucky to have trained under such a smart, caring, and wonderful person.

And to my committee, Dr. Gore, Dr. McIntyre, Dr. Manning, and Dr. Peterson: I thank you for your insight during planning, implementation, and analysis of this dissertation. Thank you for your commitment to this dissertation project, and the advice to make it the best it can be.

This work would not have been completed without the help from my colleagues, whom I now call friends: Jack, Eliot, Mary, Stephanie, Liz, Chris, Ashley, Henry, George, Jarrod, Saikat, and Nancy.

And finally, I would like to thank my funding sources for their support during the investigation of this work: National Cancer Institute - NCI R01 CA138599, NCI U24 CA126588 (Small Animal Imaging Resource Program), NCI P50 CA98131 (Breast SPORE), and NCI P30 CA068485 (VICC Cancer Center Support Grant), - and the National Center for Research Resources – NCRR 1S10 RR17858.

LIST OF FIGURES

LIST OF TABLES

TABLE OF CONTENTS

CHAPTER I

INTRODUCTION

Current radiographic analysis of therapeutic response uses changes in tumor size. With the development of anticancer therapies that specifically target molecular and physiological processes of the tumor and the tumor's microenvironment, solely assessing response on changes in tumor morphology might not be the most sensitive approach. Thus, the development of imaging techniques that can noninvasively estimate specific vascular, cellular, and molecular aspects of the tumor are of great interest. Much progress has been made to improve the quality of information available from functional and molecular imaging techniques in order to noninvasively measure tumor growth, assess tumor status, and predict treatment response. These studies have been performed in preclinical animal models as well as clinical trials, but with mixed results due to the lack of standardized imaging protocols, inadequate understanding of whether changes in imaging biomarkers predict clinical outcomes related to therapy, and lack of validation to assist in the interpretation of imaging data. Consequently, these obstacles have inhibited translation of many functional and molecular imaging techniques into routine clinical practice. Thus, a need exists to further develop quantitative imaging techniques that can report on specific characteristics of cancer in order to improve patient care.

The goals of this dissertation work were to unravel some of the issues that inhibit clinical translation by systematically evaluating clinically relevant imaging modalities to determine which technique (or set of techniques) can assess tumor response early during the course of therapy. Our research plan consisted of evaluating treatment response in a

major category of breast cancer with an established therapy, HER2-positive (HER2+) tumors exposed to trastuzumab. We performed longitudinal positron emission tomography (PET) and magnetic resonance imaging (MRI) studies to observe treatment-induced changes in vascular, cellular, and molecular characteristics of breast cancer. We also correlated the imaging data with histology to elucidate the relationship between each imaging metric and the underlying biological mechanisms of response.

The goal of Specific Aim 1 was to assess the reproducibility of several current and emerging PET and MRI techniques in a xenograft model of HER2+ breast cancer. These studies provided a measure of the imaging protocol variability, as well as a threshold value where changes greater than this value would reflect treatment-induced physiological changes distinct from measurement error. Moving forward, reproducibility measurements are useful in, for example, quantifying the required sample size to achieve a desired level of statistical power in an experimental study.

The goal of Specific Aim 2 was to evaluate the ability of several PET and techniques to provide early assessments of response to trastuzumab in HER2+ xenograft models that are either sensitive or resistant to trastuzumab. Quantitative parameters derived from the imaging data were compared to explicitly determine which imaging techniques can assess early response in trastuzumab-sensitive mice. The ability of these imaging techniques to differentiate xenografts with different trastuzumab sensitivities was also investigated. These studies have significant clinical impact as the development of imaging methods that can separate responders from nonresponders earlier during the course of therapy would minimize negative systemic effects caused by ineffective therapies.

The goal of Specific Aim 3 was to investigate the correlation between the parameters quantified from each in vivo imaging technique with histology. The objective of these comparisons was to elucidate the relationship between the imaging parameters and the underlying biology in order to aid in the interpretation of the imaging results, and potentially validate the quantified parameters.

Successfully achieving these aims will define a set of imaging techniques that are most accurate at predicting breast cancer response to treatment in a murine model of HER2+ breast cancer. In addition, it will validate the imaging data through correlation with histology. Furthermore, this work will provide a paradigm by which other imaging protocols as well as current and emerging breast cancer treatments might be evaluated.

CHAPTER II

BIOLOGICAL BACKGROUND OF HER2+ BREAST CANCER

Introduction

Breast cancer is the most common type of cancer among women in the United States, other than skin cancer. According to the most recent National Cancer Institute's Surveillance, Epidemiology, and End Results (SEER) Cancer Statistics Review (1), it is estimated that 1 in 8 women will be diagnosed with breast cancer sometime during their lifetime. Although the lifetime risk of developing breast cancer is high, the US mortality rates have steadily decreased from 33.14 per 100,000 in 1990 to 22.21 per 100,000 in 2009 (1). This decrease has thought to be the result of advances in anticancer therapies, earlier detection through screening, and increased awareness for the disease.

The development of molecular tests, especially gene expression profiling, has increased the accuracy of tumor classification and enhanced our understanding of the disease (2). Over the last several years, the development of gene expression profiling methodologies has improved the accuracy of classifying breast cancer subgroups. These advances hold great promise in improving estimation of prognosis as well as assigning appropriate treatment strategies.

The four most common subtypes of breast cancer are categorized by the expression (or lack thereof) of specific cellular receptors: luminal subtype A (estrogen and/or progesterone receptor positive), luminal subtype B (estrogen and/or progesterone receptor positive and human epidermal growth factor receptor 2 (HER2) overexpression),

HER2-overexpressed, and basal-like/triple-negative (see Table II-1). This section highlights some of the appropriate treatment strategies as well as prognostic information for each subtype. A more detailed description of the molecular signatures as well as mechanisms of action and potential resistance of an anticancer therapy (i.e., trastuzumab) that specifically targets HER2-positive (HER2+) breast cancer is also discussed.

Table II-1. Summary of Breast Cancer Molecular Subgroups (3-5)

	Luminal subtype A	Luminal subtype B	HER2+	Basal-like/TN
Breast cancer (%)	42-59%	6-19%	7-12%	14-20%
ER expression	✓	✓	x	x
HER2 overexpression	x	✓	✓	x
Prognosis	Good	Intermediate	Poor	Poor

ER: estrogen receptor; TN: triple-negative; ✓, ER expression or HER2 overexpression; x, ER not expressed or normal expression of HER2

Hormone/Receptor Status Guiding Therapy

Almost two-thirds of patients diagnosed with breast cancer in the United States have tumors that are positive for either the estrogen or progesterone (or both) receptors (6). Correctly identifying these breast cancers is important, as this subgroup could potentially benefit from endocrine therapy. Several therapies that target hormonal activity are available, and each has a different mechanism of action. Selective estrogen-receptor response modulators (SERMs) bind to the estrogen receptor (ER) and partially block its function. Tamoxifen, the most widely used SERM for the past two decades, has achieved a 39% reduction in disease recurrence and a 31% reduction in mortality rate associated with ER positive (ER+) early stage breast cancer (7). Aromatase inhibitors (AIs) are a class of anti-hormonal therapies that function to decrease estrogen levels. Current third-

generation AIs (such as anastrozole) prescribed in the adjuvant setting for postmenopausal patients improved disease-free survival and time-to-recurrence compared to tamoxifen (8). A third class of therapies, represented by fulvestrant, blocks the effects of estrogen in breast tissue through receptor downregulation and eventual degradation. The success of fulvestrant in the adjuvant setting remains to be seen, however it is currently approved for the treatment of hormone receptor-positive metastatic breast cancer in postmenopausal women who have disease progression following previous anti-estrogen therapy (9).

Types of breast cancer are also defined by the expression of HER2. HER2 (erbB2/neu) is a protein found on the cell membrane, and diagnostic tests reveal that some breast cancers either have an overexpression of the protein or too many copies of its gene. Breast cancers that are HER2+ usually receive targeted therapy, which are a subset of anticancer drugs that identify and attack specific cancer cells. Trastuzumab and lapatinib are two examples of targeted therapies prescribed for patients diagnosed with HER2+ breast cancer, as they bind to HER2 and inhibit the downstream cell signaling pathways that lead to cell proliferation and survival. Trastuzumab treatment has resulted in improved survival in the first-line setting with chemotherapy in patients with advanced disease (10,11), as well as improved recurrence-free survival and overall survival in the adjuvant setting with and sequentially following chemotherapy (12,13). Lapatinib is a small molecule tyrosine kinase inhibitor that, when prescribed with the chemotherapeutic drug capecitabine, has been shown to increase survival in patients with advanced HER2+ breast cancer that recurred following previous anthracycline, taxane, and trastuzumab treatment regimens (14).

Pathology reports may also indicate that breast tumors test negative for ER, PR, and HER2, thus classifying these tumors as triple-negative and/or basal-like. The growth of these tumors is not stimulated by estrogen or progesterone receptors, or by the overexpression of HER2. Triple-negative breast cancers (TNBCs) will not respond to anti-hormonal therapies (such as tamoxifen) or HER2-targeted therapies (such as trastuzumab), a fact that in part accounts for the unfavorable clinical outcome. There are several emerging therapies being investigated in clinical trials for the treatment and management of TNBC. For example, the addition of iniparib (a polyADP-ribose polymerase inhibitor that interferes with chemotherapy-induced DNA damage) to traditional chemotherapy improved all measurements of efficacy, including response rate, progression-free survival, and overall survival (15). Platinum compounds (e.g., cisplatin) are a group of therapies that induce DNA cross-linking that ultimately leads to apoptosis, and when used in combination with traditional chemotherapies (epifubicin+paclitaxel) achieved a 62% pathological complete response (16).

Prognosis Based on Subgroup Classification

Identifying breast cancers into subgroups based on hormone receptor status or HER2 receptor expression also provides information on prognosis (see Table II-1). A meta-analysis performed by Wirapati et al. with data from 2,833 breast cancer patients across multiple institutions revealed that proliferation rates (assessed by proliferation module score) varied between tumors categorized into subtypes based on receptor status (17). This study showed that both triple-negative and HER2+ breast cancers have higher proliferation rates compared to the other subgroups, which (in part) leads to a lower

disease-regression free survival percentage. Another study investigated clinical outcome based on the molecular profile in 412 patients who had breast conservation surgery as well as adjuvant chemotherapy and/or endocrine therapy and local radiation. This study concluded that patients with breast cancers identified as HER2+ or triple-negative had lower recurrence-free survival and overall survival percentages (5).

Molecular Signatures of HER2

HER2 (erbB2) is a member of the human epidermal growth factor receptor (HER) family of receptor tyrosine kinases that include HER1 (epidermal growth factor receptor [EGFR]), HER3 (erbB3), and HER4 (erbB4). All members have an extracellular ligand binding region, a transmembrane region, and an intracellular tyrosine kinase domain. With the exception of HER2, the HER proteins exist in an inactivated state that is activated upon ligand binding. The ligand-bound protein will undergo a conformational change that allows for the formation of homo- or heterodimers and activation of the intrinsic kinase domain resulting in phosphorylation of specific tyrosine residues. These residues serve as docking stations for adaptor proteins that link the receptor with downstream signaling pathways leading to survival and proliferation, e.g., *via* mitogen-activated protein kinase (MAPK). Since HER2 can undergo ligand-independent dimerization, it is always in a constitutively extended, open conformation and therefore is the preferred partner for other HER proteins (18).

Normal dimerization with HER2 activates signaling networks leading to cell survival and proliferation, cell cycle progression, and cytoskeletal organization (Figure II.1, adapted from reference (19)). The role of HER2 during development and adult

physiology becomes evident through genetically modified mouse studies (19). HER2 has an essential role in heart development, and embryos without the receptor die due to malformation of ventricular wall muscle fibers that are responsible for maintaining blood flow (20). Conditional ablation of HER2 in postnatal cardiac muscle resulted in ventricular enlargement of both chambers, which is consistent with dilated cardiomyopathy (21).

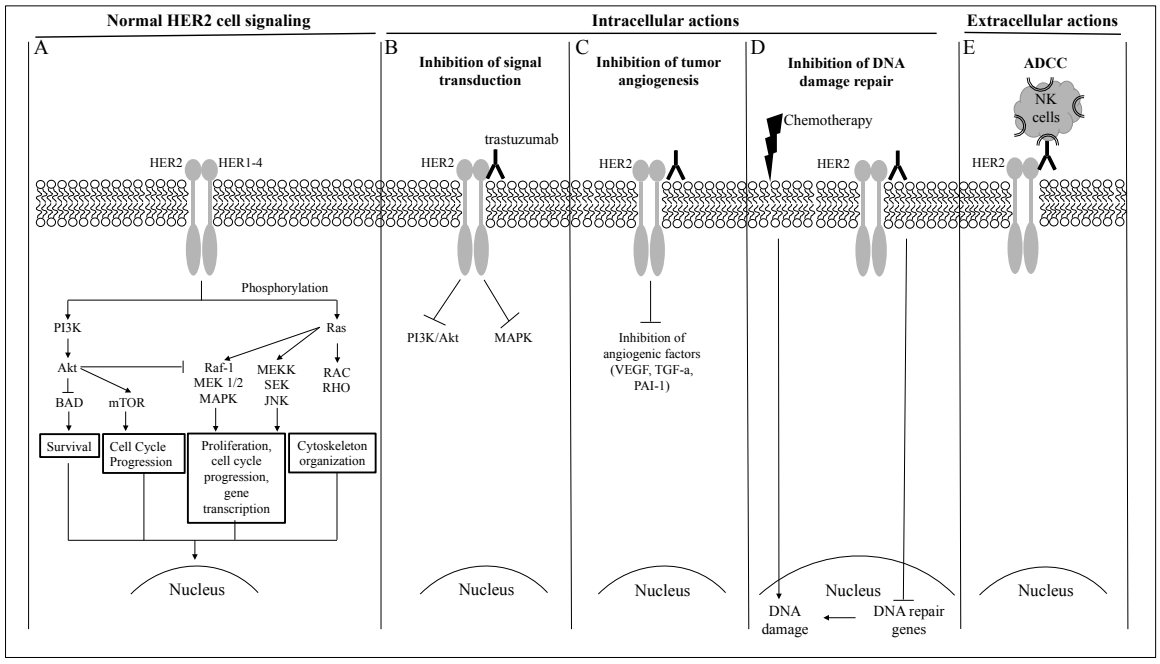

Figure II-1. Normal HER2 signaling pathways and potential intracellular and extracellular mechanisms of action of trastuzumab. Normal HER2 cell signaling networks lead to cell cycle progression, proliferation, and survival, as well as cytoskeleton organization (A). Exact mechanisms of action for trastuzumab are unclear, however several intracellular and extracellular mechanisms have been observed (B-E). Intracellular actions block HER2 cell signaling networks leading to cell proliferation and survival (B), inhibit specific angiogenic factors (C), and inhibit the ability of the cell to repair DNA damage after chemotherapy (D). Trastuzumab is a monoclonal antibody and can potentially interact with receptors on immune cells, specifically natural killer (NK) cells, and thus target the cell for degradation (E).

Even though HER2 signaling has a role in normal development and adult physiology, receptor overexpression and thus aberrant signaling have been implicated in

the development of breast cancer. HER2 overexpression leads to an upregulation of the phosphatidylinositol 3-kinase/protein kinase B (PI3K/Akt) survival pathway and of nuclear factor kB (a potent inhibitor of apoptotic stimuli) (22,23). Blocking HER2 inhibited colony formation by temporarily inhibiting PI3K/Akt activity *in vitro* in breast cancer cells that overexpressed HER2 (24). This result was not observed in cell lines with basal levels of the receptor (24).

Trastuzumab: HER2+ Breast Cancer Targeted Therapy

HER2 is an attractive target of therapy for many reasons. It is estimated that 20% to 25% of human breast cancers have HER2/neu gene amplification or receptor overexpression (19). Since half a million cases of new breast cancers are diagnosed annually in the United States, HER2+ tumors represent a significant patient population. Furthermore, as mentioned previously, HER2 overexpression correlates with a more aggressive disease phenotype and poor prognosis (25,26).

Trastuzumab (Herceptin®; Genentech, San Francisco) was the first FDA-approved HER2-targeted therapy for the treatment of HER2+ metastatic breast cancer (27). Trastuzumab was first identified by screening monoclonal antibodies that bind to the extracellular domain (ECD) of HER2; subsequent development resulted in a humanized version of the murine antibody 4D5 (28). Initial clinical trials tested trastuzumab as a monotherapy in patients with HER2+ metastatic breast cancer, and observed response rates ranging from 12% to 34% for a median duration of 9 months (29-31). A phase III clinical trial evaluated response of trastuzumab in combination with paclitaxel and observed increased response rates (50% versus 32%), longer time to

disease progression (median, 7.4 versus 4.6 months), and longer survival (median, 25.1 versus 20.3 months) compared to single-agent trastuzumab treatment (10).

Although the exact mechanisms of action of trastuzumab are unknown, evidence for several possibilities have been observed, which are depicted in Figure II-1: 1) inhibition of intracellular signaling pathways, 2) inhibition of tumor-associated angiogenesis, 3) inhibition of DNA damage repair initiated by anticancer therapy, and 4) activation of antibody-dependent cell-mediated cytotoxicity. These mechanisms of action are described in more detail below.

Inhibition of Intracellular Signaling Pathways

PI3K/Akt and MAPK pathways are both enhanced when HER2 is overexpressed leading to abnormal regulation of cell proliferation and survival signaling networks (32). In HER2-overexpressing cells, trastuzumab inhibited HER2 activation/phosphorylation, which had a consequential effect on PI3K/Akt and MAPK intracellular signaling pathways that regulate cell cycle progression and apoptosis (33). In a preclinical mouse model, tumor regression was observed after treatment with trastuzumab, owing to the inhibition of both PI3K/Akt and MAPK signaling pathways (34).

Inhibition of Tumor Associated Angiogenesis

Tumor cells secrete growth factors, such as the vascular endothelial growth factor (VEGF), which induces angiogenesis to support tumor growth. In a preclinical mouse model of HER2+ human breast cancer, trastuzumab treatment caused normalization and regression of tumor blood vessels (35). A significant reduction was observed in the

diameter (approximately 65%) and volume (approximately 85%) of blood vessels, as well as vascular permeability (approximately 66%) compared with controls at three weeks after therapy initiation ($p < 0.05$) (35). Another preclinical study observed decreased microvessel density (mean ± standard deviation) in the trastuzumab treated (35 ± 7) group compared to controls (44 ± 12) (36). Gene expression *in vitro* from both studies revealed a decrease in pro-angiogenic factors such as VEGF, transforming growth factor a (TGFa), and plasminogen activator inhibitor 1 (PAI-1) (35,36). In contrast, the anti-angiogenic factor thrombospondin 1 was upregulated after trastuzumab treatment (35).

Inhibition of DNA Damage Repair Initiated by Chemotherapy

Chemotherapy and radiotherapy induce DNA damage, and cells respond by activating genes of cell cycle arrest and apoptosis. HER2-mediated signaling pathways are important for DNA damage repair and survival, namely the PI3K and MAPK pathways. Thus, inhibiting HER2 cellular signaling also disrupts the DNA repair process. The cyclin-dependent kinase inhibitor p21 has been implicated in cellular response after DNA damage. Trastuzumab has been shown to inhibit p21 expression at 2 hours and 24 hours after exposure to the chemotherapeutic drug cisplatin (37).

Activation of Antibody-Dependent Cell-Mediated Cytotoxicity

Trastuzumab is a monoclonal antibody and thus contains an immunoglobulin G1 (IgG1) Fc structure capable of interacting with the Fcg receptor on immune effector cells, namely natural-killer (NK) cells. This interaction initiates recruitment of immune effector cells to attack the targeted cell (i.e., the cell with bound trastuzumab) (19). This process is

termed Antibody-Dependent Cell-mediated Cytotoxicity (ADCC). There are both preclinical and clinical studies supporting the role of trastuzumab-initiated ADCC, suggesting this to be a key mechanism of action. Trastuzumab-induced tumor regression was reduced in xenograft models where the Fcg receptor was deleted (38). A clinical study evaluated the role of different immune effector cells after trastuzumab treatment. Pre- and post-operative breast tissue samples were obtained from patients receiving neoadjuvant docetaxol and trastuzumab treatment and study-matched controls comprising of patients who received only docetaxol or non-trastuzumab, non-docetaxol systemic therapy. The samples from patients receiving trastuzumab treatment had a significant infiltration of NK cells and increased lymphocyte activity compared with the controls (39). Immunohistochemical analysis also resulted in a significant difference in NK cell-related staining between the trastuzumab treated and control groups ($p = 0.003$), which is consistent with trastuzumab recruitment of NK cells to the tumor.

Trastuzumab: Molecular Mechanisms of Resistance

In the adjuvant setting, trastuzumab treatment following or in combination with chemotherapy improves disease-free and overall survival rates in patients with early stage breast cancer (12,13). Yet, a portion of those patients who initially responded eventually experienced disease progression. Furthermore, many patients with HER2+ breast cancer do not respond to trastuzumab, suggesting both *de novo* and acquired mechanisms of resistance (40). Therefore, elucidating the molecular mechanisms of trastuzumab resistance is still an active area of investigation. While trastuzumab is effective at blocking HER2 homodimers, it is not effective against ligand-induced heterodimers.

Specifically, HER1-HER2 and HER2-HER3 interactions are important in driving HER2+ breast cancer cells, as well as bypassing the trastuzumab-induced inhibition of cell proliferation. Evidence to support many potential resistance mechanisms related to HER2 and HER2 interactions with other HER proteins have been reported, including: increased HER1 expression (33); increased ligand expression for either HER1 (TGFa, (33)) or HER3 (neuregulin 1, (33)); steric hindrance of HER2-antibody interaction by membrane-associated glycoproteins (41); and binding competition with circulating HER2 cleaved ECD fragments (42).

Resistance to trastuzumab might also be due to alternate downstream signaling pathways. Trastuzumab resistant cells developed *in vivo* from the BT474 human breast cancer cell line had elevated levels of phosphorylated PI3K/Akt and MAPK compared to parental cells after treatment (33). Additional studies showed that the inability of trastuzumab to block mTOR signaling is a key mechanism of resistance, and treatment with mTOR inhibitors significantly inhibited growth in trastuzumab resistant cells (43). Nagata et al. observed that a decrease in phosphatase and tensin homolog (PTEN) increased PI3K/Akt phosphorylation and blocked growth suppression mediated by trastuzumab in HER2+ breast cancer cells (44). They also showed that PTEN-deficient HER2+ breast tumors had a poorer clinical response after trastuzumab treatment. Furthermore, they observed that PI3K inhibitors rescued trastuzumab resistance of PTEN deficient cells *in vitro* and *in vivo*.

Conclusion

HER2+ breast tumors represent a large subset of all diagnosed breast cancers thereby initiating the development of many HER2 targeted therapies. Trastuzumab was the first targeted therapy approved for clinical use in patients with HER2+ metastatic breast cancer, and remains the only HER2 specific adjuvant treatment for patients with HER2+ early stage breast cancer (45). Despite the clinical success of trastuzumab, relapses still occur after adjuvant therapy resulting in disease progression invariably due to acquired trastuzumab resistance. Despite the many studies suggesting different mechanisms of resistance, currently there are very few biomarker(s) that predict the lack of clinical response or resistance to trastuzumab. Therefore, quantitative and reliable methods to assess response early during treatment would greatly benefit patient care.

References

1. Howlader N NA, Krapcho M, Neyman N, Aminou R, Altekruse SF, Kosary CL, Ruhl J, Tatalovich Z, Cho H, Mariotto A, Eisner MP, Lewis DR, Chen HS, Feuer EJ, Cronin KA (eds). SEER Cancer Statistics Review, 1975-2009 (Vintage 2009 Populations). 2011.
2. Wesolowski R, Ramaswamy B. Gene expression profiling: changing face of breast cancer classification and management. Gene Expr 2011;15(3):105-115.
3. Fornier M, Fumoleau P. The paradox of triple negative breast cancer: novel approaches to treatment. Breast J 2012;18(1):41-51.
4. Carey LA, Perou CM, Livasy CA, Dressler LG, Cowan D, Conway K, Karaca G, Troester MA, Tse CK, Edmiston S, Deming SL, Geradts J, Cheang MC, Nielsen TO, Moorman PG, Earp HS, Millikan RC. Race, breast cancer subtypes, and survival in the Carolina Breast Cancer Study. JAMA 2006;295(21):2492-2502.
5. Calza S, Hall P, Auer G, Bjohle J, Klaar S, Kronenwett U, Liu ET, Miller L, Ploner A, Smeds J, Bergh J, Pawitan Y. Intrinsic molecular signature of breast cancer in a population-based cohort of 412 patients. Breast Cancer Res 2006;8(4):R34.
6. Li CI, Daling JR, Malone KE. Incidence of invasive breast cancer by hormone receptor status from 1992 to 1998. J Clin Oncol 2003;21(1):28-34.
7. Effects of chemotherapy and hormonal therapy for early breast cancer on recurrence and 15-year survival: an overview of the randomised trials. Lancet 2005;365(9472):1687-1717.
8. Howell A, Cuzick J, Baum M, Buzdar A, Dowsett M, Forbes JF, Hoctin-Boes G, Houghton J, Locker GY, Tobias JS. Results of the ATAC (Arimidex, Tamoxifen, Alone or in Combination) trial after completion of 5 years' adjuvant treatment for breast cancer. Lancet 2005;365(9453):60-62.
9. Howell A, Robertson JF, Quaresma Albano J, Aschermannova A, Mauriac L, Kleeberg UR, Vergote I, Erikstein B, Webster A, Morris C. Fulvestrant, formerly ICI 182,780, is as effective as anastrozole in postmenopausal women with advanced breast cancer progressing after prior endocrine treatment. J Clin Oncol 2002;20(16):3396-3403.
10. Slamon DJ, Leyland-Jones B, Shak S, Fuchs H, Paton V, Bajamonde A, Fleming T, Eiermann W, Wolter J, Pegram M, Baselga J, Norton L. Use of chemotherapy plus a monoclonal antibody against HER2 for metastatic breast cancer that overexpresses HER2. N Engl J Med 2001;344(11):783-792.
11. Marty M, Cognetti F, Maraninchi D, Snyder R, Mauriac L, Tubiana-Hulin M, Chan S, Grimes D, Anton A, Lluch A, Kennedy J, O'Byrne K, Conte P, Green M, Ward C, Mayne K, Extra JM. Randomized phase II trial of the efficacy and safety of trastuzumab combined with docetaxel in patients with human epidermal growth factor receptor 2-positive metastatic breast cancer administered as first-line treatment: the M77001 study group. J Clin Oncol 2005;23(19):4265-4274.
12. Piccart-Gebhart MJ, Procter M, Leyland-Jones B, Goldhirsch A, Untch M, Smith I, Gianni L, Baselga J, Bell R, Jackisch C, Cameron D, Dowsett M, Barrios CH, Steger G, Huang CS, Andersson M, Inbar M, Lichinitser M, Lang I, Nitz U, Iwata H, Thomssen C, Lohrisch C, Suter TM, Ruschoff J, Suto T, Greatorex V, Ward C,

Straehle C, McFadden E, Dolci MS, Gelber RD. Trastuzumab after adjuvant chemotherapy in HER2-positive breast cancer. N Engl J Med 2005;353(16):1659-1672.

13. Romond EH, Perez EA, Bryant J, Suman VJ, Geyer CE, Jr., Davidson NE, Tan-Chiu E, Martino S, Paik S, Kaufman PA, Swain SM, Pisansky TM, Fehrenbacher L, Kutteh LA, Vogel VG, Visscher DW, Yothers G, Jenkins RB, Brown AM, Dakhil SR, Mamounas EP, Lingle WL, Klein PM, Ingle JN, Wolmark N. Trastuzumab plus adjuvant chemotherapy for operable HER2-positive breast cancer. N Engl J Med 2005;353(16):1673-1684.
14. Geyer CE, Forster J, Lindquist D, Chan S, Romieu CG, Pienkowski T, Jagiello-Gruszfeld A, Crown J, Chan A, Kaufman B, Skarlos D, Campone M, Davidson N, Berger M, Oliva C, Rubin SD, Stein S, Cameron D. Lapatinib plus capecitabine for HER2-positive advanced breast cancer. N Engl J Med 2006;355(26):2733-2743.
15. O'Shaughnessy J, Osborne C, Pippen JE, Yoffe M, Patt D, Rocha C, Koo IC, Sherman BM, Bradley C. Iniparib plus chemotherapy in metastatic triple-negative breast cancer. N Engl J Med 2011;364(3):205-214.
16. Frasci G, Comella P, Rinaldo M, Iodice G, Di Bonito M, D'Aiuto M, Petrillo A, Lastoria S, Siani C, Comella G, D'Aiuto G. Preoperative weekly cisplatin-epirubicin-paclitaxel with G-CSF support in triple-negative large operable breast cancer. Ann Oncol 2009;20(7):1185-1192.
17. Wirapati P, Sotiriou C, Kunkel S, Farmer P, Pradervand S, Haibe-Kains B, Desmedt C, Ignatiadis M, Sengstag T, Schutz F, Goldstein DR, Piccart M, Delorenzi M. Meta-analysis of gene expression profiles in breast cancer: toward a unified understanding of breast cancer subtyping and prognosis signatures. Breast Cancer Res 2008;10(4):R65.
18. Graus-Porta D, Beerli RR, Daly JM, Hynes NE. ErbB-2, the preferred heterodimerization partner of all ErbB receptors, is a mediator of lateral signaling. EMBO J 1997;16(7):1647-1655.
19. Spector NL, Blackwell KL. Understanding the mechanisms behind trastuzumab therapy for human epidermal growth factor receptor 2-positive breast cancer. J Clin Oncol 2009;27(34):5838-5847.
20. Lee KF, Simon H, Chen H, Bates B, Hung MC, Hauser C. Requirement for neuregulin receptor erbB2 in neural and cardiac development. Nature 1995;378(6555):394-398.
21. Hart KA, Reiss-Levy EA, Trew PA. Listeria monocytogenes peritonitis associated with CAPD. Med J Aust 1991;154(1):59-60.
22. Makino K, Day CP, Wang SC, Li YM, Hung MC. Upregulation of IKKalpha/IKKbeta by integrin-linked kinase is required for HER2/neu-induced NF-kappaB antiapoptotic pathway. Oncogene 2004;23(21):3883-3887.
23. Bacus SS, Altomare DA, Lyass L, Chin DM, Farrell MP, Gurova K, Gudkov A, Testa JR. AKT2 is frequently upregulated in HER-2/neu-positive breast cancers and may contribute to tumor aggressiveness by enhancing cell survival. Oncogene 2002;21(22):3532-3540.
24. Yakes FM, Chinratanalab W, Ritter CA, King W, Seelig S, Arteaga CL. Herceptin-induced inhibition of phosphatidylinositol-3 kinase and Akt Is required

for antibody-mediated effects on p27, cyclin D1, and antitumor action. Cancer Res 2002;62(14):4132-4141.
25. Ross JS, Fletcher JA. The HER-2/neu oncogene in breast cancer: prognostic factor, predictive factor, and target for therapy. Stem Cells 1998;16(6):413-428.
26. Slamon DJ, Clark GM, Wong SG, Levin WJ, Ullrich A, McGuire WL. Human breast cancer: correlation of relapse and survival with amplification of the HER-2/neu oncogene. Science 1987;235(4785):177-182.
27. Nahta R, Esteva FJ. HER2 therapy: molecular mechanisms of trastuzumab resistance. Breast Cancer Res 2006;8(6):215.
28. Carter P, Presta L, Gorman CM, Ridgway JB, Henner D, Wong WL, Rowland AM, Kotts C, Carver ME, Shepard HM. Humanization of an anti-p185HER2 antibody for human cancer therapy. Proc Natl Acad Sci U S A 1992;89(10):4285-4289.
29. Cobleigh MA, Vogel CL, Tripathy D, Robert NJ, Scholl S, Fehrenbacher L, Wolter JM, Paton V, Shak S, Lieberman G, Slamon DJ. Multinational study of the efficacy and safety of humanized anti-HER2 monoclonal antibody in women who have HER2-overexpressing metastatic breast cancer that has progressed after chemotherapy for metastatic disease. J Clin Oncol 1999;17(9):2639-2648.
30. Baselga J, Tripathy D, Mendelsohn J, Baughman S, Benz CC, Dantis L, Sklarin NT, Seidman AD, Hudis CA, Moore J, Rosen PP, Twaddell T, Henderson IC, Norton L. Phase II study of weekly intravenous recombinant humanized anti-p185HER2 monoclonal antibody in patients with HER2/neu-overexpressing metastatic breast cancer. J Clin Oncol 1996;14(3):737-744.
31. Vogel CL, Cobleigh MA, Tripathy D, Gutheil JC, Harris LN, Fehrenbacher L, Slamon DJ, Murphy M, Novotny WF, Burchmore M, Shak S, Stewart SJ, Press M. Efficacy and safety of trastuzumab as a single agent in first-line treatment of HER2-overexpressing metastatic breast cancer. J Clin Oncol 2002;20(3):719-726.
32. Neve RM, Holbro T, Hynes NE. Distinct roles for phosphoinositide 3-kinase, mitogen-activated protein kinase and p38 MAPK in mediating cell cycle progression of breast cancer cells. Oncogene 2002;21(29):4567-4576.
33. Ritter CA, Perez-Torres M, Rinehart C, Guix M, Dugger T, Engelman JA, Arteaga CL. Human breast cancer cells selected for resistance to trastuzumab in vivo overexpress epidermal growth factor receptor and ErbB ligands and remain dependent on the ErbB receptor network. Clin Cancer Res 2007;13(16):4909-4919.
34. Moulder SL, Yakes FM, Muthuswamy SK, Bianco R, Simpson JF, Arteaga CL. Epidermal growth factor receptor (HER1) tyrosine kinase inhibitor ZD1839 (Iressa) inhibits HER2/neu (erbB2)-overexpressing breast cancer cells in vitro and in vivo. Cancer Res 2001;61(24):8887-8895.
35. Izumi Y, Xu L, di Tomaso E, Fukumura D, Jain RK. Tumour biology: herceptin acts as an anti-angiogenic cocktail. Nature 2002;416(6878):279-280.
36. Klos KS, Zhou X, Lee S, Zhang L, Yang W, Nagata Y, Yu D. Combined trastuzumab and paclitaxel treatment better inhibits ErbB-2-mediated angiogenesis in breast carcinoma through a more effective inhibition of Akt than either treatment alone. Cancer 2003;98(7):1377-1385.

37. Pietras RJ, Pegram MD, Finn RS, Maneval DA, Slamon DJ. Remission of human breast cancer xenografts on therapy with humanized monoclonal antibody to HER-2 receptor and DNA-reactive drugs. Oncogene 1998;17(17):2235-2249.
38. Clynes RA, Towers TL, Presta LG, Ravetch JV. Inhibitory Fc receptors modulate in vivo cytotoxicity against tumor targets. Nat Med 2000;6(4):443-446.
39. Arnould L, Gelly M, Penault-Llorca F, Benoit L, Bonnetain F, Migeon C, Cabaret V, Fermeaux V, Bertheau P, Garnier J, Jeannin JF, Coudert B. Trastuzumab-based treatment of HER2-positive breast cancer: an antibody-dependent cellular cytotoxicity mechanism? Br J Cancer 2006;94(2):259-267.
40. Piccart M. Circumventing de novo and acquired resistance to trastuzumab: new hope for the care of ErbB2-positive breast cancer. Clin Breast Cancer 2008;8 Suppl 3:S100-113.
41. Nagy P, Friedlander E, Tanner M, Kapanen AI, Carraway KL, Isola J, Jovin TM. Decreased accessibility and lack of activation of ErbB2 in JIMT-1, a herceptin-resistant, MUC4-expressing breast cancer cell line. Cancer Res 2005;65(2):473-482.
42. Zabrecky JR, Lam T, McKenzie SJ, Carney W. The extracellular domain of p185/neu is released from the surface of human breast carcinoma cells, SK-BR-3. J Biol Chem 1991;266(3):1716-1720.
43. Miller TW, Forbes JT, Shah C, Wyatt SK, Manning HC, Olivares MG, Sanchez V, Dugger TC, de Matos Granja N, Narasanna A, Cook RS, Kennedy JP, Lindsley CW, Arteaga CL. Inhibition of mammalian target of rapamycin is required for optimal antitumor effect of HER2 inhibitors against HER2-overexpressing cancer cells. Clin Cancer Res 2009;15(23):7266-7276.
44. Nagata Y, Lan KH, Zhou X, Tan M, Esteva FJ, Sahin AA, Klos KS, Li P, Monia BP, Nguyen NT, Hortobagyi GN, Hung MC, Yu D. PTEN activation contributes to tumor inhibition by trastuzumab, and loss of PTEN predicts trastuzumab resistance in patients. Cancer Cell 2004;6(2):117-127.
45. Arteaga CL, Sliwkowski MX, Osborne CK, Perez EA, Puglisi F, Gianni L. Treatment of HER2-positive breast cancer: current status and future perspectives. Nat Rev Clin Oncol 2012;9(1):16-32.

CHAPTER III

FUNCTIONAL AND MOLECULAR IMAGING OF CANCER

Introduction

The current radiographic assessment of tumor response is based on the Response Evaluation Criteria in Solid Tumors (RECIST), which uses one-dimensional changes in tumor size to indicate response (1). These response criteria offer standardized methods to evaluate the longest diameter for all target lesions from anatomical imaging data. Under these criteria, definitions of treatment response are divided into four categories, which are summarized in Table III-1

Table III-1. RECIST response categories

Response Categories	**Description**
Complete Response	all target lesions have disappeared
Partial Response	at least 30% decrease in sum of the longest diameter from all target lesions, using the baseline sum as a reference point
Progressive Disease	at least 20% increase in sum of the longest diameter from all target lesions, using the smallest sum of the longest diameter recorded since the treatment started or the appearance of one or more new lesions as reference
Stable Disease	neither sufficient increase or decrease to satisfy the above categories

Although RECIST has been used extensively since its introduction in 2000, some concerns about the method have not been addressed (2), even with the most recent updates in 2009, RECIST 1.1 (3). One fundamental statistical issue is the reduction of

continuous tumor size and response to a series of four categories (i.e., Table III-1). Additionally, with emerging and developing therapies that are frequently cytostatic, long-term stable disease could be a beneficial outcome. For example, in tumors where size shrinks slowly after treatment, such as gastrointestinal stromal tumors (4), patients live for long periods with stable disease. Another limiting issue is that the results from RECIST are based on linear changes along one-dimension, where tumors are most certainly changing along three dimensions. These one-dimensional measurements are based on anatomical and morphological changes that are temporally delayed behind molecular and physiological changes (5). Thus, imaging techniques with the sensitivity to quantify changes in molecular characteristics of cancer would potentially offer earlier and more specific assessments of treatment response.

Indeed, a supplement recently published in *The Journal of Nuclear Medicine* (2) was devoted to the development of metabolic response criteria to assess treatment response using positron emission tomography (PET). Wahl et al. introduce new criteria called "PERCIST" – Positron Emission tomography Response Criteria in Solid Tumors (2). The idea of PERCIST is that PET, with the ^{18}F-labeled glucose analog 2-deoxy-2-^{18}F-fluoro-D-glucose (^{18}F-FDG), more accurately assesses the continuous and time-dependent nature of cancer response compared to RECIST, as well as, provides estimates of the metabolic changes of the tumor. The effort to develop quantitative PET methods to monitor tumor response in the preclinical and clinical settings has been remarkable (6-19). Additionally, efforts to improve the quality of quantitative information from magnetic resonance imaging (MRI) techniques for use in assessing treatment response are also increasing (20-32). This section highlights several current and emerging PET and MRI

techniques that are being investigated as biomarkers of cancer treatment response. The basic fundamentals, biological basis, and several quantitative parameters for each imaging method are also discussed. Example applications in cancer are also presented.

Positron Emission Tomography

PET imaging in principle is the spatial location of radiation emitted from a positron-electron annihilation event (33). An injected radiopharmaceutical distributed throughout the subject emits positrons as a by-product of radioactive decay. An emitted positron will then travel a short distance before it encounters an electron and annihilates to form two 511-keV photons (traveling approximately 180° apart) that are detected

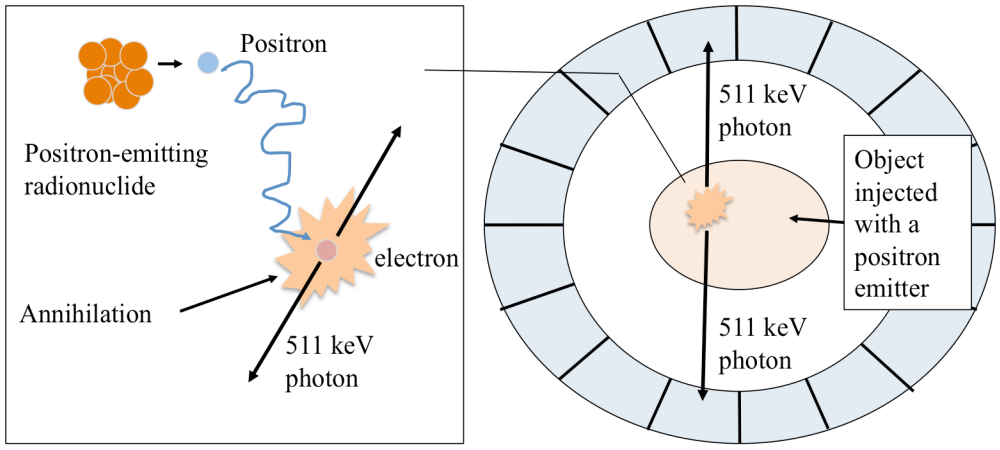

Figure III-1. Basic physics of Positron Emission Tomography. A positron-emitting radionuclide is injected into a subject. The positron will travel a short distance before it encounters an electron and annihilates to form two 511-keV photons that travel approximately 180° apart. When a pair of detectors on opposite sides of the subject registers two photons simultaneously (e.g., within 10^{-9} seconds), the positron emission is thought to occur along a line between the two detectors.

during PET acquisition (34). PET imaging depends on the coincidence detection of two within a detector pair located on opposite sides of the subject being imaged (see Figure III-1). When detectors on opposite sides of the subject register photons within 10^{-9}

seconds of one another, the annihilation event is thought to have occurred along a line between the detectors. Thus, the resulting PET image is a distribution of the number of positron decays or "counts" spatially localized within the subject.

Data Analysis

PET scans are intrinsically quantitative, and using a quantitative metric to assess early treatment-induced changes is an attractive tool to measure subclinical responses (2). Two main classes of PET data analysis exist: semi-quantitative and quantitative. The standardized uptake value (SUV) is the most widely used semi-quantitative parameter, and is calculated either voxel-wise or over a region of interest (ROI). The SUV of a dynamic series of time points t is calculated as:

$$\mathrm{SUV}(t) = \frac{\mathrm{c}(t)\ (\mathrm{MBq/kg})}{\text{injected dose (MBq)} / \text{body weight (kg)}}, \qquad \text{(III-1)}$$

where c(t) is tissue radioactivity concentration at time t. For small animals, such as mice, the percent-injected dose per gram (%ID/g) is often reported instead of the SUV as the weight is usually similar between animals (35):

$$\%\mathrm{ID/g}(t) = \frac{\mathrm{c}(t)\ (\mathrm{MBq/kg})}{\text{injected dose (MBq)}} \times 100. \qquad \text{(III-2)}$$

PERCIST recommends that the SUV be normalized to lean body mass (SUL), which is less dependent on body habitus across populations (2). Additionally, SUL is typically more consistent than SUV between subjects and imaging time points. The main advantage of the semi-quantitative methods compared to the quantitative methods is the relative ease of data acquisition (importantly, these measurements do not require a blood sample) and analysis.

While the semi-quantitative parameters are easier to determine, they only quantify the radiotracer uptake within a tissue at a snapshot in time. In order to fully characterize radiotracer pharmacokinetics, a quantitative analysis of dynamically acquired data is required. The standard three-compartment model used to analyze dynamic PET data is shown in Figure III-2, with rate constants K_1-k_4 that represent the rate of transport between plasma and tissue, rate of outflow from the tissue to plasma, radiotracer phosphorylation rate, and the dephosphorylation rate, respectively (36).

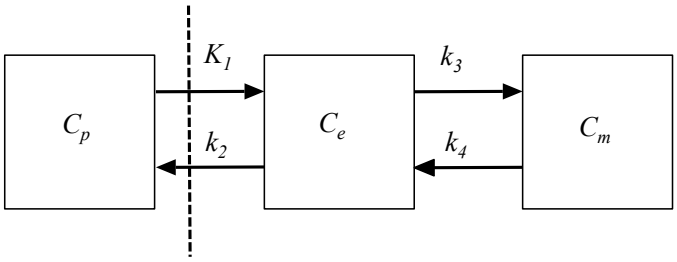

Figure III-2. A standard, 3-compartment, 4-rate constant model used to analyze dynamic PET data. C_p represents the radiotracer activity concentration in the plasma. The tissue is composed of two compartments, the exchangeable compartment, C_e, and the metabolized or trapped compartment, C_m. The parameters K_1-k_4 represent rate constants that describe transport between compartments.

At anytime after injection, the total radiotracer concentration in the tissue, C_t, equals the sum of the amounts of free and phosphorylated radiotracer in the exchangeable compartment, C_e, and metabolized compartment, C_m, respectively (36):

$$C_t = (C_e + C_m + V_b \cdot C_p)\rho, \tag{III-3}$$

where V_b is the blood volume fraction and r is the tissue specific gravity. The rate of change in the amount of exchangeable radiotracer in the tissue, dC_e/d_t, is described by:

$$\frac{dC_e}{dt} = K_1 C_p - k_2 C_e - k_3 C_e + k_4 C_m. \tag{III-4}$$

The rate of change in the amount of tracer that is phosphorylated, dC_m/d_t, is:

$$\frac{dC_m}{dt} = k_3 C_e - k_4 C_m. \qquad \text{(III-5)}$$

Equations (III-3) – (III-5) provide the basis for the determination of the rate constants K_1-k_4, and describe the time course of the radioactivity in the tissue as a function of time. The time rate of change of tracer concentration predicted by the model (C_t) is fit to the measured dynamic time course (example from a tumor illustrated in Figure III-3B) using a nonlinear least-squares optimization method. The estimated rate constants (i.e., K_1-k_4), can then be used to calculate the net tracer flux, K_i, for any tracer i:

$$K_i = \frac{K_1 \cdot k_3}{k_2 + k_3}. \qquad \text{(III-6)}$$

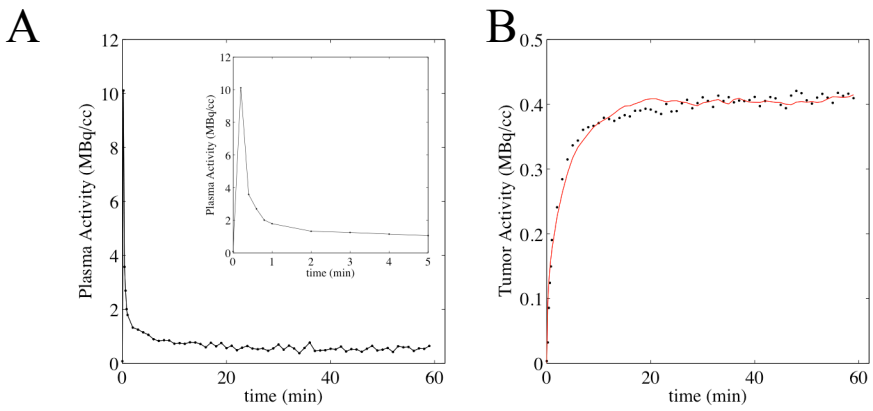

Figure III-3. Example time activity curves from the left ventricle (A) and tumor (B). To show the fast wash-in/wash-out and peak concentration for the left ventricle time activity, the first five minutes is graphed in the inset figure to panel A. The time activity curves from the left ventricle and tumor are fit to the three compartment model to generate the line of best fit, which is illustrated as the red line in panel B.

To perform fully quantitative pharmacokinetic modeling, an accurate blood plasma time activity curve that serves as the model input function is typically required. The gold standard for making this measurement is blood sampling (37), which can be quite challenging and often labor intensive. Several noninvasive methods to estimate the

blood plasma time activity curve have been proposed (including, factor analysis methods (38), standardized input functions (39), and simultaneous estimation (40)); however, image-derived input functions (IDIFs) are most commonly used (41). IDIFs are collected from PET image data by drawing ROIs around a large blood pool, which is often a major artery in the field of view or the left ventricle of the heart. An example of an IDIF from a left ventricle of a mouse is illustrated in Figure III-3A. The size of the tissues used to generate plasma time activity curves are often small relative to the imaging voxel and therefore the resulting time activity curves are a combination of the blood concentration and surrounding tissues; the terms given to this issue are spillover and partial-voluming. Corrections for spillover and partial-volume effects are often applied *via* a recovery coefficient, which is defined as the ratio between the measured activity and true activity (37,42,43). Most often, the recovery coefficient is determined from PET images of a phantom acquired under similar conditions as the experimental data (37,42,43).

Current and Emerging PET Radiotracers

The most commonly used radiotracer for breast cancer imaging is the ^{18}F-labeled glucose analog, ^{18}F-FDG. ^{18}F-FDG is actively taken up in cells *via* the Glut-1 and Glut-3 transporters and phosphorylated by hexokinase to ^{18}F-FDG-6-PO_4. Once phosphorylated, ^{18}F-FDG-6-PO_4 is not metabolized further in the glycolytic pathway and remains trapped in the cell. The rate of phosphorylation is proportional to the metabolic rate of the cell, thus cells with high metabolic rates will accumulate more ^{18}F-FDG. High glycolytic index is a hallmark of cancer (44), thus tumor cells will accumulate more ^{18}F-FDG compared to healthy tissue.

The limited utility of ^{18}F-FDG PET for use in tissues with high background signal (e.g., the brain), has led to the development of other ^{18}F-labeled tracers that probe other molecular processes that might be altered in cancer. Two emerging ^{18}F-labeled radiotracers for PET imaging are 3'-deoxy-3'-^{18}F-fluorothymidine (^{18}F-FLT) and ^{18}F-fluoromisonidazole (^{18}F-FMISO), which are designed to reflect tumor proliferation (8) and hypoxia (12), respectively.

The increased proliferative activity of tumor cells is a well known characteristic of cancer (44). Alterations in cellular proliferation occur, by definition, before changes in tumor size; thus, it is reasonable to hypothesize that imaging techniques reporting on cell proliferation could offer an early indication of therapeutic response. ^{18}F-FLT is a thymidine analog, and has emerged as a promising PET tracer for estimating cell proliferation. Cells undergoing proliferation are actively transporting extracellular thymidine into the cell *via* the salvage pathway, which is then phosphorylated by thymidine kinase 1 (TK1) which is upregulated during the DNA synthesis phase. ^{18}F-FLT works in an analogous fashion: ^{18}F-FLT is introduced into the bloodstream and transported form the blood into the cytosol *via* the same nucleoside transporters as thymidine, where it is phosphorylated by TK1 into ^{18}F-FLT-monophosphate and is retained in tissues. While ^{18}F-FLT-monophosphate may continue to be phosphorylated into ^{18}F-FLT-diphosphate and ^{18}F-FLT-triphosphate, phosphorylated ^{18}F-FLT cannot be incorporated into the growing DNA chain (as the 3' position was substituted by ^{18}F) thus there will be an accumulation of ^{18}F-FLT-mono-, di-, and triphosphate in the cell. Cells that have an increased amount and activity of TK1 (e.g., tumor cells) will accumulate more ^{18}F-FLT than normal tissues.

A tumor will quickly outgrow its blood supply as it proliferates, resulting in pockets of hypoxia that are heterogeneously spaced throughout the tumor. A specific PET radiotracer designed to accumulate in regions of low oxygen content is ^{18}F-FMISO, which is lipophilic and freely diffuses through the cell membrane; however, retention is determined by the local oxygen tension (45). ^{18}F-FMISO is a radiolabeled nitroimidazole that, once in the cell, is immediately reduced to R-NO_2 radicals, regardless of intracellular oxygen concentration (8). If the cell has normal oxygen levels (> 4 mmHg (46)), the radical is reoxidized and can diffuse out of the cell. However, if intracellular oxygen is low, the R-NO_2 radical is further reduced and will covalently bind to intracellular macromolecules and become trapped. ^{18}F-FMISO has a unique characteristic in that it is not retained in necrotic cells as the electron transport chain that reduces ^{18}F-FMISO into a bioreductive alkylating agent is only active in viable cells (45).

Applications in Cancer

^{18}F-FDG PET has been well characterized for the use of differentiating benign versus malignant lesions, preoperative staging, and detecting recurrent disease and metastasis (2,47). Efforts to expand the use of ^{18}F-FDG PET in detection of cancer and evaluation of treatment response are ongoing (48,49). For example, Schmitz et al. recently reported that ^{18}F-FDG PET provided an early marker of treatment response in patients with squamous cell carcinoma of the head and neck (48). Additionally, the maximum SUV correlated with residual tumor cellularity on surgical specimens.

While there are a number of studies reporting the clinical utility of ^{18}F-FDG, there are also a growing number of studies that observe the opposite outcome (7,15,18). For

example, Shah et al. observed similar SUV values from ^{18}F-FDG PET between responders and nonresponders in a mouse model of HER2+ breast cancer (18). For these reasons, radiotracers that reflect molecular processes other than tumor metabolism are of great interest (19,50).

The clinical utility of ^{18}F-FLT PET for diagnosing and staging cancer as well as assessing therapeutic response has previously been investigated (16,51,52). In preclinical studies, ^{18}F-FLT PET is also being used to evaluate treatment efficacy of novel targeted anticancer drugs (53,54). Although these studies highlight ^{18}F-FLT PET as a promising early biomarker of treatment response, recent studies have also shown the limited utility of ^{18}F-FLT PET (9,55). Herrmann et al. acquired ^{18}F-FLT PET and ^{18}F-FDG PET data on patients with pancreatic tumors, and observed that ^{18}F-FLT PET had lower sensitivity in differentiating pancreatic tumors than ^{18}F-FDG PET (9). Additionally, a preclinical study by McKinley et al. provides evidence that suggests ^{18}F-FLT PET may not always be a surrogate biomarker of the proliferative index of specific tumors (55). These outcomes thus emphasize the need to perform a systematic evaluation (e.g., similar to the work performed in this dissertation) with ^{18}F-FLT PET in a variety of cancer types and treatment regimens. These types of studies are imperative if ^{18}F-FLT PET is to be employed in routine clinical care of cancer.

^{18}F-FMISO PET is another emerging radiotracer that has been investigated to determine if the parameters derived from the image data can assess treatment efficacy in rodent cancer models. (21,56). Bokacheva et al. performed longitudinal ^{18}F-FMISO PET with a rat model of colorectal cancer, and observed a decrease in tumor hypoxia after treatment with an antiangiogenic agent (21). Valable et al. also observed a subsequent

decrease in tumor hypoxia as assessed *via* ^{18}F-FMISO PET after antiangiogenic treatment in a rat glioma model (56).

Magnetic Resonance Imaging

In addition to ^{18}F-FDG PET imaging, the use of MRI in diagnosing and staging cancer, as well as assessing treatment efficacy is well established. This dissertation employs two MR techniques that have been successful in the clinic: diffusion-weighted MRI (DW-MRI) and dynamic contrast enhanced MRI (DCE-MRI). For clarity and understanding of DW-MRI and DCE-MRI, this first section highlights the basic fundamentals of NMR in the context of how image contrast is generated, in general, before moving on to the specifics about the DW-MRI and DCE-MRI techniques. For a more detailed description, please see (for example) reference (57).

The signal from a typical MRI session is derived from the magnetic properties of ^{1}H nuclei. Each ^{1}H nucleus possesses a magnetic moment that has both a magnitude and direction. These magnetic dipole moments, or "spins", have random alignment (Figure III-4A); however, when nuclei with magnetic moments are placed within an external

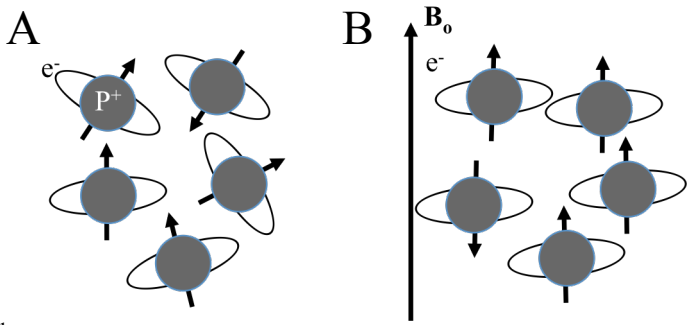

Figure III-4. ^{1}H nuclei spins in a system usually have random alignment (A). However, in the presence of an external magnetic field, the spins will align either parallel or antiparallel to the external field $\boldsymbol{B_o}$ (B).

magnetic field B_0, the spins will seek to align in a low energy state that is either parallel or antiparallel to the external magnetic field (Figure III-4B).

If external energy is applied, in the form, for example, of a radiofrequency (RF) pulse, the resulting proton signal is time varying due to the nature of the tissue, the interactions within the tissue, and the applied, external forces (58). Thus, the time-varying signal and extent to which the signal varies is dependent on the tissue type. The term given to describe how the signal varies in time is called relaxation. One of the most important principles in MRI is that the magnetization in different tissues gives rise to different relaxation and thus different observed proton signals. This is the basis for MR image contrast.

As described above, the spins will seek to align (either parallel or antiparallel) to the external field B_0 creating a net magnetic moment M, as illustrated in Figure III-5A. When the net magnetization along the z-axis is perturbed, the magnetic moment is tipped away from parallel (Figure III-5B); however, the net magnetic moment will seek to regain the equilibrium state and eventually relax back to alignment with B_0. This process is described as longitudinal relaxation and is characterized by the time constant T_1.

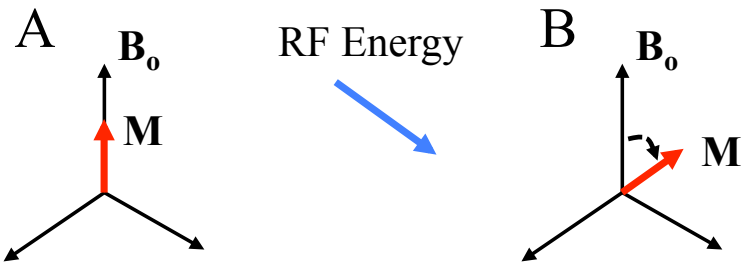

Figure III-5. The "spins" are summed to form a net magnetization M that at equilibrium is aligned with the external magnetic field B_o (A). As RF energy is applied, M will tip away from equilibrium (B); however, M will seek to regain equilibrium state and "relax" back; a term defined as longitudinal relaxation.

The longitudinal relaxation is not the only type of relaxation occurring within the system. When the net magnetization is tipped away from its equilibrium state (i.e., parallel to B_0), the transverse components (x, y) of M will rotate about B_0 with a certain frequency. However, the spins exist in environments that are not completely homogeneous, and the local field inhomogeneities experienced by the spins will result in a dispersion of precession. In other words, the spins are initially coherently aligned after RF energy is applied (Figure III-6A). With time the coherent collection of spins experience local field fluctuations leading to the exponential loss of their coherence (Figure III-6 B and C), and are said to relax. This is called transverse relaxation, which is characterized by the time constant T_2.

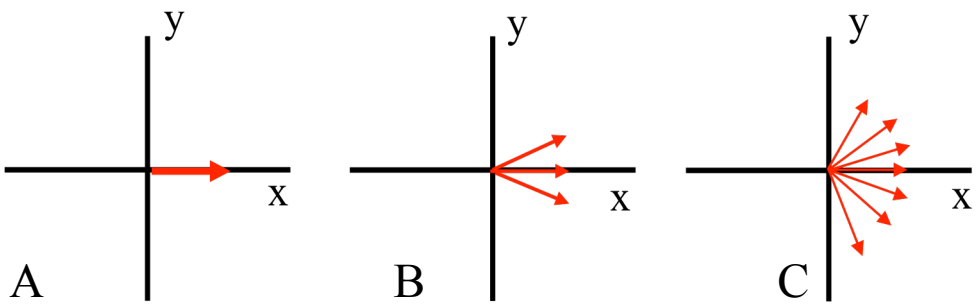

Figure III-6. Initially after the RF pulse, the spins in the transverse plane (perpendicular to the external magnetic field $\boldsymbol{B_o}$) will coherently align (A). Due to local field fluctuations, the spins will begin to lose their coherence (B), and are said to relax (C). This is defined as the transverse relaxation.

By manipulating the timing and the strength of the radiofrequency pulses, sequences can be developed to better exploit these T_1 or T_2 relaxation properties to differentiate between tissue types and disease states. The two most common MR experiments are the spin echo and gradient echo acquisitions. A spin echo sequence is most often used in diffusion-weighted MRI to investigate water diffusion in a tissue of

interest. A gradient echo pulse sequence is most often used to acquire dynamic images after contrast agent injection for a DCE-MRI analysis. These two sequences in the context of the specific imaging modalities (i.e., DW-MRI and DCE-MRI) are discussed in more detail below.

Diffusion-Weighted MRI

Self-diffusion or Brownian motion is the microscopic thermally induced behavior of water molecules moving in a random pattern. Diffusion measurements reflect the effective displacement of water molecules within a certain time interval. The diffusion path length r^2 of a free water molecule is governed by the Einstein equation:

$$r^2 = 2Dt \tag{III-7}$$

where D is the diffusivity and t is the time interval. For example, the average displacement of a free water molecule at body temperature (~37 °C) with a diffusivity of 3.0 mm^2/ms during a 20 ms time interval is approximately 11 mm. Because this is comparable to the diameter of most cells, there is a high probability that a water molecule will interact with intact cellular components such as the hydrophobic cell membrane, intracellular organelles, and macromolecules, thereby impeding their motion (30,59). The observed rate of diffusion in cellular tissues will therefore be less than free water, which is often described by an apparent diffusion coefficient (ADC). Imaging techniques such as DW-MRI have been developed to quantify ADC and, in well-controlled situations, variations in ADC have been correlated with cellularity (60).

Data Acquisition and Analysis

MRI is able to measure water diffusion by applying a pair of diffusion-sensitizing gradients to any MRI pulse sequence, the most common being the pulsed-gradient spin echo (PGSE) where the diffusion gradients are applied on opposite sides of the 180° RF pulse (see Figure III-7). The total diffusion weighting imparted to the tissue of interest is indicated by the "*b*-value", which is calculated as:

$$b = \gamma^2 \delta^2 G^2 \left(\Delta - \delta / 3\right), \tag{III-8}$$

where *g is* the gyromagnetic ratio of water, and *d, G,* and *D* are the gradient duration, amplitude, and time between application, respectively.

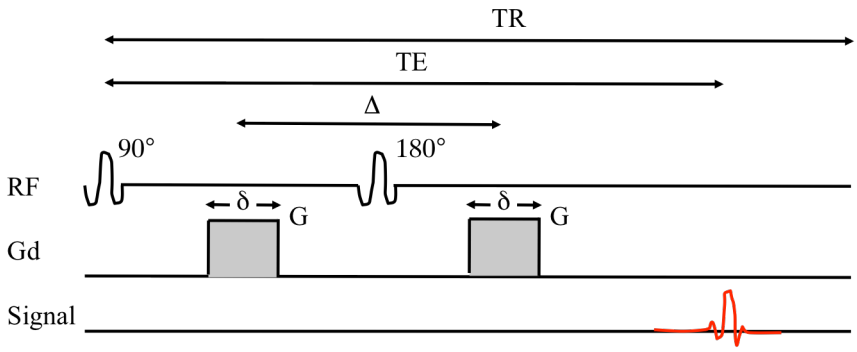

Figure III-7. Typical pulsed-gradient spin echo pulse sequence used for diffusion-weighted MR imaging. Two diffusion gradients with amplitude G and duration δ separated by the diffusion time Δ are equally spaced around the 180° RF pulse.

The signal from a standard spin echo pulse sequence depends on the proton density *r*, T_1, and T_2. However, during a diffusion-weighted experiment, the signal will also depend on the amount of diffusion weighting. Thus, the spin echo signal equation is amended to include a diffusion term:

$$S = S_0 \rho \cdot (1 - e^{TR/T_1}) \cdot e^{-TE/T_2} \cdot e^{-ADC \cdot b}, \tag{III-9}$$

where *TR* and *TE* are the repetition time and echo time, respectively, and *b* is defined in Eq. (III-8). By varying the amplitude and duration of the diffusion-sensitizing gradients (thereby varying the *b*-value) and acquiring multiple diffusion-weighted images, the resulting data is exponentially fit to Eq. (III-9) to calculate ADC. ADC can be calculated for a ROI or each image voxel to generate ADC parametric maps; illustrations of each are shown in Figure III-8.

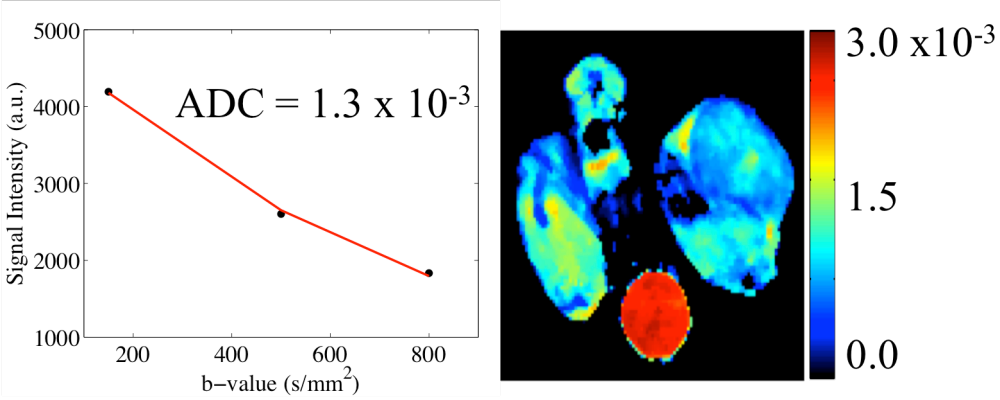

Figure III-8. Diffusion-weighted data can be fit for an ROI to return one ADC value (*left*), or fit for every image voxel to calculate a parametric map (*right*). Units of ADC are in mm^2/s.

Applications in Cancer

Since a hallmark of cancer is uncontrolled cell proliferation leading to high cell density and loss of normal cytoarchitecture (27), DW-MRI could provide an early biomarker of pathology. Recent work has provided convincing data that DW-MRI can be used to characterize malignancy and determine lesion aggressiveness (61,62). For example, a study collected DW-MRI data from 136 female patients with 162 breast lesions (149 invasive lesions and 13 ductal carcinomas *in situ*) and then correlated ADC with histological grade (61). The results revealed a significant ($p < 0.001$) inverse

correlation between tumor ADC and histological grade. Additionally, the mean ADC of the "less aggressive" group (grade 1 and *in situ* lesions) was 1.19×10^{-3} mm^2/s, which was higher than the mean ADC (0.96×10^{-3} mm^2/s) of the "more aggressive" group (grade 2-3 invasive carcinomas).

In addition to characterizing tumor aggressiveness, the clinical utility of DW-MRI to assess treatment response has been shown (25,32). A study performed by Yankeelov et al. acquired DW-MRI data from 11 patients with locally advanced breast cancer prior to and post chemotherapy but before surgery (32). This work observed a significant increase ($p < 0.005$) in ADC from 1.61×10^{-3} mm^2/s before treatment to 2.0×10^{-3} mm^2/s post-treatment. In another study involving 15 patients with locally advanced breast cancer, Jensen et al. also observed a significant increase ($p = 0.008$) in mean ADC after one cycle of neoadjuvant chemotherapy (25).

Dynamic Contrast Enhanced MRI

DCE-MRI is an imaging technique that characterizes the pharmacokinetics of an injected contrast agent (CA) as it enters and leaves a region of tissue. As the CA passes through a tissue, it will interact with the hydrogen nuclei of water and shorten the tissue's native longitudinal relaxation rates (i.e., both T_1 and T_2; though DCE-MRI is focused entirely on T_1 changes induced by the contrast agent). The ability of a CA to alter relaxation is quantified by its "relaxivity", which relates to what extent the relaxation rate R_1 ($\equiv 1/T_1$) is changed with respect to the concentration of the CA. The most common relationship between these parameters is described as (63):

$$R_1 = r_1 \cdot [CA] + R_{10}, \tag{III-10}$$

where r_1 is the CA-specific relaxivity (in units of $mM^{-1}s^{-1}$), [CA] is the concentration of the CA in the tissue, and R_{10} is the baseline longitudinal relaxation rate.

A characteristic of an ideal MR CA is a high number of unpaired electrons, as the unpaired electrons have a larger magnetic moment than the nuclei. Thus, MR contrast agents are designed with a large number of unpaired electrons in order to dominate the magnetic moment produced by the CA nuclei. Another ideal characteristic of MR contrast agents is an appropriate correlation time. Molecules in a liquid will rotate freely, and the inverse of their rotation frequency is known as the correlation time. Molecules with an optimum correlation time can interact with surrounding molecules more frequently causing the relaxation times to change.

Typical, clinically employed, MRI CAs are composed of gadolinium (Gd) within an appropriate chelate; gadolinium diethylenetriaminepentaacetic acid (Gd-DTPA) is one such molecule. Gd-DTPA is a small (~0.6 kDa) hydrophilic, barrier-limited molecule that is stable *in vivo* and has minimal toxicity. (Toxicity issues have recently been reported in patients with certain types of kidney disease. For more detail, see reference (64). The effect of the CA results in an increase in signal intensity, to a degree determined by the accumulation of the CA, on a T_1-weighted image. Serial acquisition of T_1-weighted MR images before, during, and after CA administration generates a signal intensity time course (see Figure III-9) that can then be analyzed quantitatively in order to characterize various physiological features of the tissue vasculature including blood flow, vessel permeability, and tissue volume fractions (58).

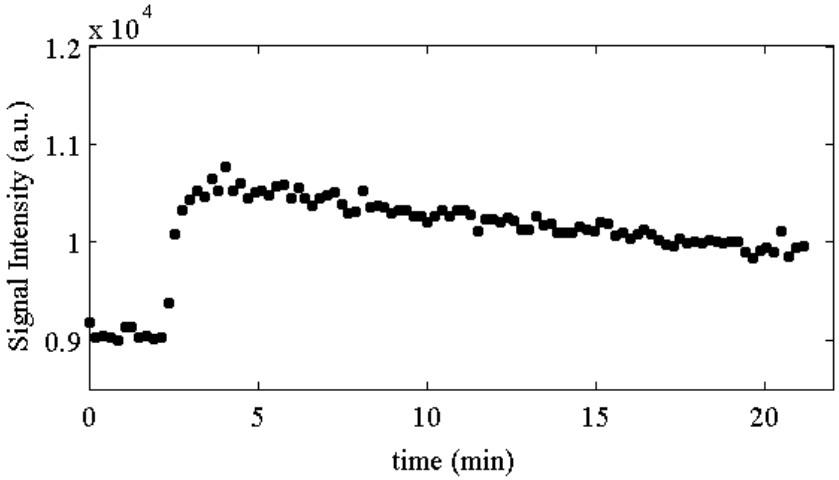

Figure III-9. An example of the change in signal intensity within a tissue of interest after contrast agent injection.

Data Acquisition

The three main components needed to perform an analysis of DCE-MRI data are: 1) a series of T_1-weighted images during CA injection, 2) native T_1 ($\equiv 1/R_{10}$) prior to the injection of the CA, and 3) the vascular or arterial input function (VIF/AIF). Each of these components is discussed in more detail below.

T_1-Weighted Dynamic Images

To observe the T_1 changes induced by the CA, T_1-weighted MR images must be acquired before, during, and after CA injection. Similar to any MR imaging experiment, trade-offs exist between temporal resolution and spatial resolution. For example, if the main objective is to characterize rapid kinetics of the CA, then high temporal resolution (on the order of a few seconds) should be acquired. However, if the experiment must assess tissue heterogeneity and cover a large field of view, as in most oncological applications, then high spatial resolution is required. The latter requirement necessitates a reduction in temporal resolution (64). Thus, when designing a DCE-MRI protocol it is

imperative to first consider the temporal resolution and spatial resolution requirements in the context of the study objectives.

Once the temporal and spatial resolution needs are determined, serial T_1-weighted images are typically acquired using a gradient echo pulse sequence. Dynamic gradient echo images are acquired for a set acquisition time, which is typically 10-20 minutes in the preclinical setting and 5-10 minutes in the clinical setting. The signal equation for a standard gradient echo pulse sequence is:

$$S = S_0 \cdot \frac{(1 - e^{-TR/T_1}) \cdot \sin(\alpha) \cdot e^{-TE/T_2^*}}{1 - \cos(\alpha) \cdot e^{-TR/T_1}}, \qquad \text{(III-11)}$$

where a is the flip angle of the RF pulse and T_2^* represents the combination of T_2 and T_2', which is a quantity that represents magnetic field inhomogeneity. The parameters *TR*, *TE*, and *a* can be manipulated such that the resulting image can be either T_1- or T_2-weighted. For T_1-weighted sequences commonly used in DCE-MRI experiments, a short *TR* relative to T_1 and a very short *TE* (i.e., TE << T_2^* so that exp(-*TE*/T_2^*) → 1) are used.

T_1 Mapping Techniques

Pharmacokinetic analysis of DCE-MRI data requires a measure of the native T_1 of the tissue (T_{10}). In a typical DCE-MRI experiment, there is not enough time to quantify the T_1 at each sample point during a dynamic acquisition after CA injection. Thus, a pre-contrast T_1 map is critical for calibrating the observed changes in signal intensity due to entrance and exit of the CA. Several methods have been employed in DCE-MRI studies, including spin echo or gradient echo with varied flip angle (a) or repetition time (*TR*) (57,65), and inversion recovery with varied inversion times (TI) (66,67). The latter

technique is employed in this dissertation, and thus a more detailed description is presented below.

In an inversion recovery sequence, the net magnetization is flipped 180° and is sampled along the magnetization recovery at different times, which are called inversion times, *TI*. The signal intensity after the inversion pulse is:

$$S = S_0 \cdot \left| 1 - 2 \cdot e^{-TI/T_1} + e^{-TR/T_1} \right|. \qquad \text{(III-12)}$$

An example of the absolute value of the signal intensity at multiple inversion times is graphically presented in Figure III-10A. The data is then fit to Eq. (III-12) to produce an estimation of T_1. This can be performed for a ROI or every image voxel resulting in a T_1 parametric map; illustrations of each are displayed in Figure III-10.

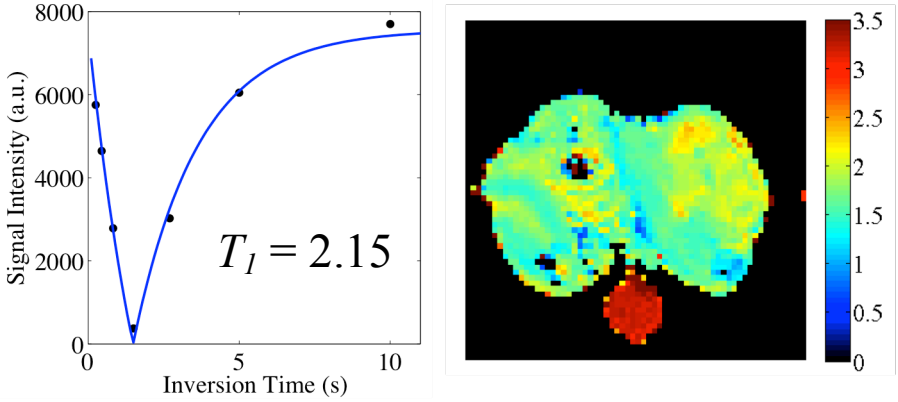

Figure III-10. Representative examples of data fit to the inversion recovery sequence equation to calculate T_1 are displayed for a tumor ROI (*left*) or for every voxel creating a parametric map (*right*). The line of best fit from Eq. (III-12) is the blue, solid line in panel A. The units of T_1 are seconds.

Arterial Input Function

Knowledge of the time rate of change of the CA concentration in the blood pool, the so-called arterial input function (AIF), is required for most quantitative DCE-MRI

analyses. The AIF after a bolus injection is typically characterized by a steep wash-in, followed by a short-lived peak concentration, and a subsequent longer washout period. The current "gold standard" for making this measurement, as mentioned previously in the PET section, is blood sampling (68). However, the difficulty of collecting blood samples at a sufficient temporal resolution, particularly in small animals, limits the efficiency of this method. Another method of estimating the AIF is derived directly from the MR imaging data. A ROI can be placed within a large vessel located in the field of view or left ventricle of the heart, then the signal intensity time course from the blood can be converted to concentration using Eq. (III-10). In some applications, however, a blood pool large enough to characterize the AIF may not always coincide within the imaging field of view. Thus, a population-derived AIF (67,69) or reference tissue (66,70) have been proposed as alternatives for measuring an AIF for each subject. This dissertation employed a population-derived AIF from a gender and aged matched population of mice that was previously published by Loveless et al. (67); an illustration of the population-derived AIF is presented in Figure III-11.

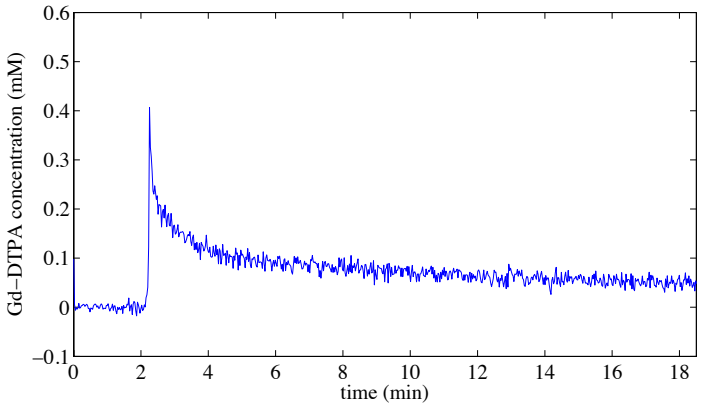

Figure III-11. Population-derived arterial input function used in all DCE-MRI data analyses in this Dissertation.

Data Analysis

There are two main classes of DCE-MRI data analyses: semi-quantitative and quantitative. A semi-quantitative analysis returns parameters that are calculated based on the shape characteristics of the dynamic time course. Typical semi-quantitative parameters are the initial area under the curve (iAUC), enhancement, time to peak, and wash-in/wash-out slope (64), as depicted in Figure III-12 (adapted from reference (64)). The iAUC is calculated as the area under the signal intensity time course from the time of CA injection to a designated time after injection. Enhancement is quantified as the percent change in signal intensity from the peak to baseline divided by the baseline signal intensity value. The time to peak is the time between CA injection and maximum value of the signal intensity curve. The wash-in and wash-out slopes are the slope of the line between the injection time and the peak of the curve and the peak of the curve until the end of data acquisition, respectively. While semi-quantitative analyses of DCE-MRI data have several advantages, a significant disadvantage is that the parameters might not

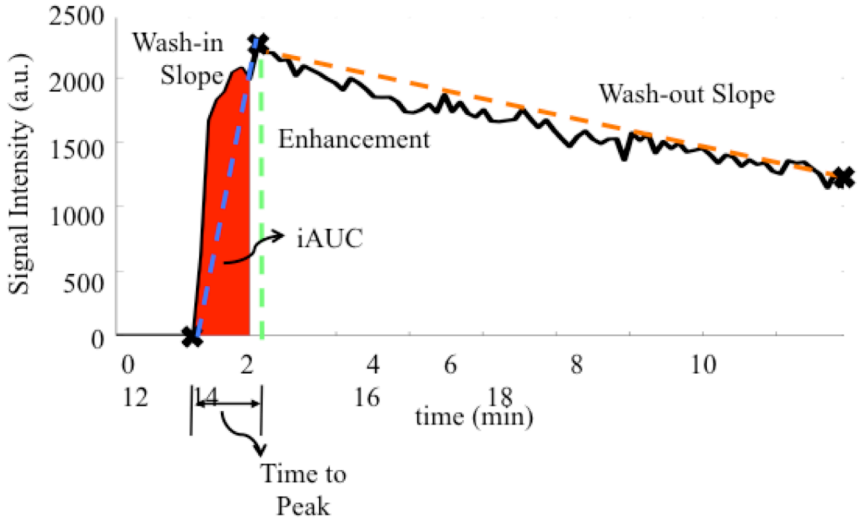

Figure III-12. Several semi-quantitative parameters derived from DCE-MRI analyses are illustrated. All of these parameters are based on the characteristic shape of the dynamic signal intensity time course.

directly relate to the underlying physiology. Thus, at times, the parameter interpretation in the context of assessing treatment response, for example, might be challenging.

Quantitative DCE-MRI uses mathematical models in order to understand and quantify parameters that directly reflect underlying physiology. The most commonly used model is the Kety-Tofts model where the concentration of the CA resides in two compartments, the blood/plasma (denoted by C_p) and the tissue space (denoted by C_t) as shown in Figure III-13 (71,72).

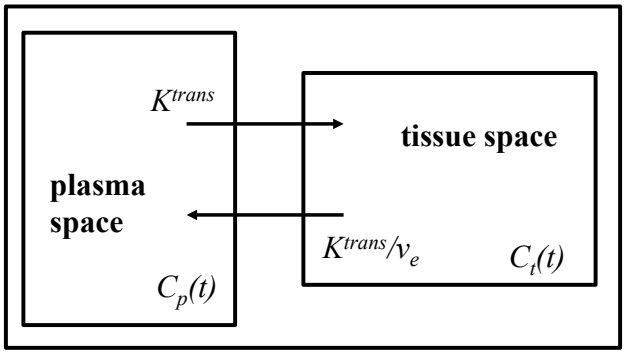

Figure III-13. Two-compartment model showing compartments representing the plasma (C_p) space and the tissue (C_t) space. The contrast agent leaves from the tissue at a rate represented by K^{trans} (volume transfer constant), and returns to the plasma from the tissue space at a rate represented by K^{trans}/v_e (efflux constant).

Using the standard DCE-MRI notation presented by Tofts et al. in 1999, K^{trans} is the volume transfer constant between the plasma and tissue space, and v_e is the extravascular-extracellular volume fraction ((71,72), see Figure III-13). If the CA agent distribution is assumed to be homogeneous in both tissue compartments, then the concentration change within the tissue, $\frac{dC_t(t)}{dt}$, is described by:

$$\frac{dC_t(t)}{dt} = K^{trans} \cdot C_p(t) - \frac{K^{trans}}{v_e} C_t(t), \qquad \text{(III-13)}$$

for which the solution is given by:

$$C_t(t) = K^{trans} \int_0^t C_p(u) \cdot e^{-(K^{trans}/v_e)(t-u)} du. \quad \text{(III-14)}$$

This model neglects any fraction of the tissue that may contain vascular space; however, previous studies have shown that the contribution from vascular space may not be negligible in tumors (73,74). Therefore, Eq. (III-14) has been amended to included a third parameter that reflects the fraction of vascular space (v_p) (75):

$$C_t(t) = K^{trans} \int_0^t C_p(u) \cdot e^{-(K^{trans}/v_e)(t-u)} du + v_p C_p(t). \quad \text{(III-15)}$$

In these forms, if $C_p(t)$ and $C_t(t)$ are measured, then these data can be fit to Eq. (III-14) or (III-15) using a nonlinear least squares method to extract estimates of K^{trans} and v_e (also v_p) for a given tissue of interest on either a voxel by voxel or ROI basis.

Compared to the semi-quantitative parameters, this class of DCE-MRI analysis generates parameters that have the clearest correlation to the underlying physiology. It should be noted, however, that K^{trans} has several physiological interpretations depending on the balance between blood flow and vessel permeability (71). In high-permeability situations, K^{trans} is equal to the blood plasma flow (F) per unit volume: $K^{trans} = F \cdot \rho \cdot (1 - hct)$, where ρ is the density of the tissue and hct is the blood hematocrit. In the other limiting case of low permeability, the CA flux is permeability limited, and thus K^{trans} is equal to the permeability surface area product (PS) between the blood plasma and the extravascular-extracellular space: $K^{trans} = PS \cdot \rho$. There are also situations of mixed flow and PS where neither flow nor permeability is the main limiting factor, but rather a combination of the two. In the mixed case, K^{trans} is equal to the extraction fraction E $(= 1 - e^{-PS/F(1-hct)}) \times F \cdot \rho \cdot (1 - hct)$.

Applications in Cancer

Antivascular and antiangiogenic drugs are two classes of cancer therapeutics that are designed to alter tumor vasculature. Antivascular agents target the vascular endothelium, resulting in reduced vasculature, perfusion, and blood volume. Antiangiogenic agents target specific proteins along the angiogenic pathway, ultimately inhibiting tumor neovascularization. Since DCE-MRI has been shown to be sensitive to physiological changes in tumor vasculature including perfusion and vessel permeability, as well as vascular and extravascular volume fractions (71,76), it has the potential to provide surrogate biomarkers of both antivascular and antiangiogenic therapies.

Although the semi-quantitative parameters may not always directly reflect the underlying physiology, their ability to assess the effect of antivascular agents have been reported. Robinson et al. quantified iAUC for the first 150 seconds after injection and observed a marked shift in the histogram of voxel-based iAUC values after antivascular therapy, indicating reduced perfusion, in a rat model of thyroid cancer (31). Another study performed by Marzola et al. used the iAUC to evaluate the effect of a tyrosine kinase inhibitor in a murine model of colon cancer (77). The authors observed a significant decrease ($p < 0.05$) in the iAUC at 92 seconds post injection between the pre-treatment and 24-hour post-treatment acquisitions (77).

Quantitative parameters have also been successfully used to assess longitudinal treatment response (22,29,78). For example, Loveless et al. quantified longitudinal changes in K^{trans} after antiangiogenic therapy in a mouse model of lung cancer (29). The work indicated a significant ($p < 0.05$) post-treatment reduction in K^{trans}. Checkley et al. investigated therapeutic efficacy of a VEGF inhibitor on prostate adenocarcinoma

xenografts using both K^{trans} and v_e (22). The work showed a decrease in both K^{trans} and v_e for all doses of the drug, with significant decreases in K^{trans} for doses ≥ 25 mg/kg and v_e for doses ≥ 50 mg/kg.

The clinical utility of quantitative DCE analyses has also been reported. Li et al. evaluated the ability of DCE-MRI parameters to predict early response of breast cancer to neoadjuvant chemotherapy (28). This work resulted in a significant decrease in the extravasation rate constant k_{ep} ($\equiv K^{trans} / v_e$) between responders and nonresponders after one cycle of therapy, thus suggesting that k_{ep} is an early predictor of tumor response. Another study monitoring the effects of chemoradiotherapy using DCE-MRI in patients with oral cancer observed significant increases in K^{trans} and v_e between pre- and post-treatment in the responders, suggesting that increases in vessel permeability and extravascular-extracellular space are indicative of good tumor response (23).

Conclusion

Much progress has been made to improve the quality of information from the functional and molecular imaging techniques described in this Chapter. However, effective translation of most of these techniques into routine clinical practice has yet to be realized. This can be attributed to the paucity of standardized imaging protocols, inadequate understanding of whether imaging protocols can predict therapeutic efficacy, and the lack of validation to assist in the interpretation of imaging data (5,59). Nevertheless, functional and molecular imaging techniques can have a fundamental role in oncology as they have the ability to measure treatment-induced changes without perturbing the physiological system.

References

1. Therasse P, Arbuck SG, Eisenhauer EA, Wanders J, Kaplan RS, Rubinstein L, Verweij J, Van Glabbeke M, van Oosterom AT, Christian MC, Gwyther SG. New guidelines to evaluate the response to treatment in solid tumors. European Organization for Research and Treatment of Cancer, National Cancer Institute of the United States, National Cancer Institute of Canada. J Natl Cancer Inst 2000;92(3):205-216.
2. Wahl RL, Jacene H, Kasamon Y, Lodge MA. From RECIST to PERCIST: Evolving Considerations for PET response criteria in solid tumors. J Nucl Med 2009;50 Suppl 1:122S-150S.
3. Eisenhauer EA, Therasse P, Bogaerts J, Schwartz LH, Sargent D, Ford R, Dancey J, Arbuck S, Gwyther S, Mooney M, Rubinstein L, Shankar L, Dodd L, Kaplan R, Lacombe D, Verweij J. New response evaluation criteria in solid tumours: revised RECIST guideline (version 1.1). Eur J Cancer 2009;45(2):228-247.
4. Benjamin RS, Choi H, Macapinlac HA, Burgess MA, Patel SR, Chen LL, Podoloff DA, Charnsangavej C. We should desist using RECIST, at least in GIST. J Clin Oncol 2007;25(13):1760-1764.
5. Harry VN, Semple SI, Parkin DE, Gilbert FJ. Use of new imaging techniques to predict tumour response to therapy. Lancet Oncol 2010;11(1):92-102.
6. Aide N, Kinross K, Cullinane C, Roselt P, Waldeck K, Neels O, Dorow D, McArthur G, Hicks RJ. 18F-FLT PET as a surrogate marker of drug efficacy during mTOR inhibition by everolimus in a preclinical cisplatin-resistant ovarian tumor model. J Nucl Med 2010;51(10):1559-1564.
7. Chen W, Cloughesy T, Kamdar N, Satyamurthy N, Bergsneider M, Liau L, Mischel P, Czernin J, Phelps ME, Silverman DH. Imaging proliferation in brain tumors with 18F-FLT PET: comparison with 18F-FDG. J Nucl Med 2005;46(6):945-952.
8. Dunphy MP, Lewis JS. Radiopharmaceuticals in preclinical and clinical development for monitoring of therapy with PET. J Nucl Med 2009;50 Suppl 1:106S-121S.
9. Herrmann K, Erkan M, Dobritz M, Schuster T, Siveke JT, Beer AJ, Wester HJ, Schmid RM, Friess H, Schwaiger M, Kleeff J, Buck AK. Comparison of 3'-deoxy-3'-[(1)(8)F]fluorothymidine positron emission tomography (FLT PET) and FDG PET/CT for the detection and characterization of pancreatic tumours. Eur J Nucl Med Mol Imaging 2012;39(5):846-851.
10. Hoeben BA, Troost EG, Span PN, van Herpen CM, Bussink J, Oyen WJ, Kaanders JH. 18F-FLT PET during radiotherapy or chemoradiotherapy in head and neck squamous cell carcinoma is an early predictor of outcome. J Nucl Med 2013;54(4):532-540.
11. Idema AJ, Hoffmann AL, Boogaarts HD, Troost EG, Wesseling P, Heerschap A, van der Graaf WT, Grotenhuis JA, Oyen WJ. 3'-Deoxy-3'-18F-fluorothymidine PET-derived proliferative volume predicts overall survival in high-grade glioma patients. J Nucl Med 2012;53(12):1904-1910.

12. Koh WJ, Rasey JS, Evans ML, Grierson JR, Lewellen TK, Graham MM, Krohn KA, Griffin TW. Imaging of hypoxia in human tumors with [F-18]fluoromisonidazole. Int J Radiat Oncol Biol Phys 1992;22(1):199-212.
13. Mason NS, Lopresti BJ, Ruszkiewicz J, Dong X, Joyce S, Leef G, Sen M, Wahed AS, Mathis CA, Grandis JR, Thomas SM. Utility of 3'-[(18)F]fluoro-3'-deoxythymidine as a PET tracer to monitor response to gene therapy in a xenograft model of head and neck carcinoma. Am J Nucl Med Mol Imaging 2013;3(1):16-31.
14. McKinley ET, Bugaj JE, Zhao P, Guleryuz S, Mantis C, Gokhale PC, Wild R, Manning HC. 18FDG-PET predicts pharmacodynamic response to OSI-906, a dual IGF-1R/IR inhibitor, in preclinical mouse models of lung cancer. Clin Cancer Res 2011;17(10):3332-3340.
15. McKinley ET, Smith RA, Zhao P, Fu A, Saleh SA, Uddin MI, Washington MK, Coffey RJ, Manning HC. 3'-Deoxy-3'-18F-fluorothymidine PET predicts response to (V600E)BRAF-targeted therapy in preclinical models of colorectal cancer. J Nucl Med 2013;54(3):424-430.
16. Mileshkin L, Hicks RJ, Hughes BG, Mitchell PL, Charu V, Gitlitz BJ, Macfarlane D, Solomon B, Amler LC, Yu W, Pirzkall A, Fine BM. Changes in 18F-fluorodeoxyglucose and 18F-fluorodeoxythymidine positron emission tomography imaging in patients with non-small cell lung cancer treated with erlotinib. Clin Cancer Res 2011;17(10):3304-3315.
17. Muzi M, Spence AM, O'Sullivan F, Mankoff DA, Wells JM, Grierson JR, Link JM, Krohn KA. Kinetic analysis of 3'-deoxy-3'-18F-fluorothymidine in patients with gliomas. J Nucl Med 2006;47(10):1612-1621.
18. Shah C, Miller TW, Wyatt SK, McKinley ET, Olivares MG, Sanchez V, Nolting DD, Buck JR, Zhao P, Ansari MS, Baldwin RM, Gore JC, Schiff R, Arteaga CL, Manning HC. Imaging biomarkers predict response to anti-HER2 (ErbB2) therapy in preclinical models of breast cancer. Clin Cancer Res 2009;15(14):4712-4721.
19. Tang D, Hight MR, McKinley ET, Fu A, Buck JR, Smith RA, Tantawy MN, Peterson TE, Colvin DC, Ansari MS, Nickels M, Manning HC. Quantitative preclinical imaging of TSPO expression in glioma using N,N-diethyl-2-(2-(4-(2-18F-fluoroethoxy)phenyl)-5,7-dimethylpyrazolo[1,5-a]pyrimi din-3-yl)acetamide. J Nucl Med 2012;53(2):287-294.
20. Aliu SO, Wilmes LJ, Moasser MM, Hann BC, Li KL, Wang D, Hylton NM. MRI methods for evaluating the effects of tyrosine kinase inhibitor administration used to enhance chemotherapy efficiency in a breast tumor xenograft model. J Magn Reson Imaging 2009;29(5):1071-1079.
21. Bokacheva L, Kotedia K, Reese M, Ricketts SA, Halliday J, Le CH, Koutcher JA, Carlin S. Response of HT29 colorectal xenograft model to cediranib assessed with 18 F-fluoromisonidazole positron emission tomography, dynamic contrast-enhanced and diffusion-weighted MRI. NMR Biomed 2013;26(2):151-163.
22. Checkley D, Tessier JJ, Kendrew J, Waterton JC, Wedge SR. Use of dynamic contrast-enhanced MRI to evaluate acute treatment with ZD6474, a VEGF signalling inhibitor, in PC-3 prostate tumours. Br J Cancer 2003;89(10):1889-1895.

23. Chikui T, Kitamoto E, Kawano S, Sugiura T, Obara M, Simonetti AW, Hatakenaka M, Matsuo Y, Koga S, Ohga M, Nakamura K, Yoshiura K. Pharmacokinetic analysis based on dynamic contrast-enhanced MRI for evaluating tumor response to preoperative therapy for oral cancer. J Magn Reson Imaging 2012;36(3):589-597.
24. Galbraith SM, Rustin GJ, Lodge MA, Taylor NJ, Stirling JJ, Jameson M, Thompson P, Hough D, Gumbrell L, Padhani AR. Effects of 5,6-dimethylxanthenone-4-acetic acid on human tumor microcirculation assessed by dynamic contrast-enhanced magnetic resonance imaging. J Clin Oncol 2002;20(18):3826-3840.
25. Jensen LR, Garzon B, Heldahl MG, Bathen TF, Lundgren S, Gribbestad IS. Diffusion-weighted and dynamic contrast-enhanced MRI in evaluation of early treatment effects during neoadjuvant chemotherapy in breast cancer patients. J Magn Reson Imaging 2011;34(5):1099-1109.
26. Karroum O, Mignion L, Kengen J, Karmani L, Leveque P, Danhier P, Magat J, Bol A, Labar D, Gregoire V, Bouzin C, Feron O, Gallez B, Jordan BF. Multimodal imaging of tumor response to sorafenib combined with radiation therapy: comparison between diffusion-weighted MRI, choline spectroscopy and (18) F-FLT PET imaging. Contrast Media Mol Imaging 2013;8(3):274-280.
27. Li SP, Padhani AR. Tumor response assessments with diffusion and perfusion MRI. J Magn Reson Imaging 2012;35(4):745-763.
28. Li X, Arlinghaus LR, Ayers GD, Chakravarthy AB, Abramson RG, Abramson VG, Atuegwu N, Farley J, Mayer IA, Kelley MC, Meszoely IM, Means-Powell J, Grau AM, Sanders M, Bhave SR, Yankeelov TE. DCE-MRI analysis methods for predicting the response of breast cancer to neoadjuvant chemotherapy: Pilot study findings. Magn Reson Med 2013.
29. Loveless ME, Lawson D, Collins M, Nadella MV, Reimer C, Huszar D, Halliday J, Waterton JC, Gore JC, Yankeelov TE. Comparisons of the efficacy of a Jak1/2 inhibitor (AZD1480) with a VEGF signaling inhibitor (cediranib) and sham treatments in mouse tumors using DCE-MRI, DW-MRI, and histology. Neoplasia 2012;14(1):54-64.
30. Padhani AR, Khan AA. Diffusion-weighted (DW) and dynamic contrast-enhanced (DCE) magnetic resonance imaging (MRI) for monitoring anticancer therapy. Target Oncol 2010;5(1):39-52.
31. Robinson SP, McIntyre DJ, Checkley D, Tessier JJ, Howe FA, Griffiths JR, Ashton SE, Ryan AJ, Blakey DC, Waterton JC. Tumour dose response to the antivascular agent ZD6126 assessed by magnetic resonance imaging. Br J Cancer 2003;88(10):1592-1597.
32. Yankeelov TE, Lepage M, Chakravarthy A, Broome EE, Niermann KJ, Kelley MC, Meszoely I, Mayer IA, Herman CR, McManus K, Price RR, Gore JC. Integration of quantitative DCE-MRI and ADC mapping to monitor treatment response in human breast cancer: initial results. Magn Reson Imaging 2007;25(1):1-13.
33. William R. Hendee ERR. Medical Imaging Physics. New York, NY: Wiley-Liss, Inc.; 2002.

34. Yankeelov TE, Peterson TE, Abramson RG, Garcia-Izquierdo D, Arlinghaus LR, Li X, Atuegwu NC, Catana C, Manning HC, Fayad ZA, Gore JC. Simultaneous PET-MRI in oncology: a solution looking for a problem? Magn Reson Imaging 2012;30(9):1342-1356.
35. Dandekar M, Tseng JR, Gambhir SS. Reproducibility of 18F-FDG microPET studies in mouse tumor xenografts. J Nucl Med 2007;48(4):602-607.
36. Muzi M, Mankoff DA, Grierson JR, Wells JM, Vesselle H, Krohn KA. Kinetic modeling of 3'-deoxy-3'-fluorothymidine in somatic tumors: mathematical studies. J Nucl Med 2005;46(2):371-380.
37. Fang YH, Muzic RF, Jr. Spillover and partial-volume correction for image-derived input functions for small-animal 18F-FDG PET studies. J Nucl Med 2008;49(4):606-614.
38. Kim J, Herrero P, Sharp T, Laforest R, Rowland DJ, Tai YC, Lewis JS, Welch MJ. Minimally invasive method of determining blood input function from PET images in rodents. J Nucl Med 2006;47(2):330-336.
39. Meyer PT, Circiumaru V, Cardi CA, Thomas DH, Bal H, Acton PD. Simplified quantification of small animal [18F]FDG PET studies using a standard arterial input function. Eur J Nucl Med Mol Imaging 2006;33(8):948-954.
40. Wong KP, Feng D, Meikle SR, Fulham MJ. Simultaneous estimation of physiological parameters and the input function--in vivo PET data. IEEE Trans Inf Technol Biomed 2001;5(1):67-76.
41. van der Weerdt AP, Klein LJ, Boellaard R, Visser CA, Visser FC, Lammertsma AA. Image-derived input functions for determination of MRGlu in cardiac (18)F-FDG PET scans. J Nucl Med 2001;42(11):1622-1629.
42. Whisenant JG, Peterson TE, Fluckiger JU, Tantawy MN, Ayers GD, Yankeelov TE. Reproducibility of static and dynamic (18)F-FDG, (18)F-FLT, and (18)F-FMISO MicroPET studies in a murine model of HER2+ breast cancer. Mol Imaging Biol 2013;15(1):87-96.
43. Tantawy MN, Peterson TE. Simplified [18F]FDG image-derived input function using the left ventricle, liver, and one venous blood sample. Mol Imaging 2010;9(2):76-86.
44. Hanahan D, Weinberg RA. Hallmarks of cancer: the next generation. Cell 2011;144(5):646-674.
45. Padhani AR, Krohn KA, Lewis JS, Alber M. Imaging oxygenation of human tumours. Eur Radiol 2007;17(4):861-872.
46. Bartlett RM, Beattie BJ, Naryanan M, Georgi JC, Chen Q, Carlin SD, Roble G, Zanzonico PB, Gonen M, O'Donoghue J, Fischer A, Humm JL. Image-guided PO2 probe measurements correlated with parametric images derived from 18F-fluoromisonidazole small-animal PET data in rats. J Nucl Med 2012;53(10):1608-1615.
47. Glunde K, Pathak AP, Bhujwalla ZM. Molecular-functional imaging of cancer: to image and imagine. Trends Mol Med 2007;13(7):287-297.
48. Schmitz S, Hamoir M, Reychler H, Magremanne M, Weynand B, Lhommel R, Hanin FX, Duprez T, Michoux N, Rommel D, Lonneux M, Cappoen N, Gillain A, Machiels JP. Tumour response and safety of cetuximab in a window pre-operative

study in patients with squamous cell carcinoma of the head and neck. Ann Oncol 2013.
49. Muylle K, Castaigne C, Flamen P. 18F-fluoro-2-deoxy-D-glucose positron emission tomographic imaging: recent developments in head and neck cancer. Curr Opin Oncol 2005;17(3):249-253.
50. Rice SL, Roney CA, Daumar P, Lewis JS. The next generation of positron emission tomography radiopharmaceuticals in oncology. Semin Nucl Med 2011;41(4):265-282.
51. Kahraman D, Holstein A, Scheffler M, Zander T, Nogova L, Lammertsma AA, Boellaard R, Neumaier B, Dietlein M, Wolf J, Kobe C. Tumor lesion glycolysis and tumor lesion proliferation for response prediction and prognostic differentiation in patients with advanced non-small cell lung cancer treated with erlotinib. Clin Nucl Med 2012;37(11):1058-1064.
52. Kahraman D, Scheffler M, Zander T, Nogova L, Lammertsma AA, Boellaard R, Neumaier B, Ullrich RT, Holstein A, Dietlein M, Wolf J, Kobe C. Quantitative analysis of response to treatment with erlotinib in advanced non-small cell lung cancer using 18F-FDG and 3'-deoxy-3'-18F-fluorothymidine PET. J Nucl Med 2011;52(12):1871-1877.
53. Perumal M, Pillai RG, Barthel H, Leyton J, Latigo JR, Forster M, Mitchell F, Jackman AL, Aboagye EO. Redistribution of nucleoside transporters to the cell membrane provides a novel approach for imaging thymidylate synthase inhibition by positron emission tomography. Cancer Res 2006;66(17):8558-8564.
54. Lee SJ, Kim EJ, Lee HJ, Kim SY, Oh SJ, Ryu JS, Moon DH, Ahn JH, Kim SW. A pilot study for the early assessment of the effects of BMS-754807 plus gefitinib in an H292 tumor model by [(18)F]fluorothymidine-positron emission tomography. Invest New Drugs 2013;31(3):506-515.
55. McKinley ET, Ayers GD, Smith RA, Saleh SA, Zhao P, Washington MK, Coffey RJ, Manning HC. Limits of [18F]-FLT PET as a biomarker of proliferation in oncology. PLoS One 2013;8(3):e58938.
56. Valable S, Petit E, Roussel S, Marteau L, Toutain J, Divoux D, Sobrio F, Delamare J, Barre L, Bernaudin M. Complementary information from magnetic resonance imaging and (18)F-fluoromisonidazole positron emission tomography in the assessment of the response to an antiangiogenic treatment in a rat brain tumor model. Nucl Med Biol 2011;38(6):781-793.
57. Haacke M BR, Thompson M, Venkatesan R. Magnetic Resonance Imaging: Physical Principles and Sequence Design: Wiley-Liss; 1999.
58. Yankeelov TE, Pickens, D.R., Price R.R. Quantitative MRI in Cancer. Hendee WR, editor. Boca Raton, FL: Taylor & Francis Group, LLC; 2012.
59. Padhani AR, Liu G, Koh DM, Chenevert TL, Thoeny HC, Takahara T, Dzik-Jurasz A, Ross BD, Van Cauteren M, Collins D, Hammoud DA, Rustin GJ, Taouli B, Choyke PL. Diffusion-weighted magnetic resonance imaging as a cancer biomarker: consensus and recommendations. Neoplasia 2009;11(2):102-125.
60. Anderson AW, Xie J, Pizzonia J, Bronen RA, Spencer DD, Gore JC. Effects of cell volume fraction changes on apparent diffusion in human cells. Magn Reson Imaging 2000;18(6):689-695.

61. Costantini M, Belli P, Rinaldi P, Bufi E, Giardina G, Franceschini G, Petrone G, Bonomo L. Diffusion-weighted imaging in breast cancer: relationship between apparent diffusion coefficient and tumour aggressiveness. Clin Radiol 2010;65(12):1005-1012.
62. Goyal A, Sharma R, Bhalla AS, Gamanagatti S, Seth A, Iyer VK, Das P. Diffusion-weighted MRI in renal cell carcinoma: a surrogate marker for predicting nuclear grade and histological subtype. Acta Radiol 2012;53(3):349-358.
63. Landis CS, Li X, Telang FW, Molina PE, Palyka I, Vetek G, Springer CS, Jr. Equilibrium transcytolemmal water-exchange kinetics in skeletal muscle in vivo. Magn Reson Med 1999;42(3):467-478.
64. Thomsen HS. Gadolinium-based contrast media may be nephrotoxic even at approved doses. Eur Radiol 2004;14(9):1654-1656.
65. Barnes SL, Whisenant JG, Loveless ME, Yankeelov TE. Practical Dynamic Contrast Enhanced MRI in Small Animal Models of Cancer: Data Acquisition, Data Analysis, and Interpretation. Pharmaceutics 2012;4(3):442-478.
66. Loveless ME, Whisenant JG, Wilson K, Lyshchik A, Sinha TK, Gore JC, Yankeelov TE. Coregistration of ultrasonography and magnetic resonance imaging with a preliminary investigation of the spatial colocalization of vascular endothelial growth factor receptor 2 expression and tumor perfusion in a murine tumor model. Mol Imaging 2009;8(4):187-198.
67. Yankeelov TE, Cron GO, Addison CL, Wallace JC, Wilkins RC, Pappas BA, Santyr GE, Gore JC. Comparison of a reference region model with direct measurement of an AIF in the analysis of DCE-MRI data. Magn Reson Med 2007;57(2):353-361.
68. Loveless ME, Halliday J, Liess C, Xu L, Dortch RD, Whisenant J, Waterton JC, Gore JC, Yankeelov TE. A quantitative comparison of the influence of individual versus population-derived vascular input functions on dynamic contrast enhanced-MRI in small animals. Magn Reson Med 2012;67(1):226-236.
69. Fritz-Hansen T, Rostrup E, Larsson HB, Sondergaard L, Ring P, Henriksen O. Measurement of the arterial concentration of Gd-DTPA using MRI: a step toward quantitative perfusion imaging. Magn Reson Med 1996;36(2):225-231.
70. Parker GJ, Roberts C, Macdonald A, Buonaccorsi GA, Cheung S, Buckley DL, Jackson A, Watson Y, Davies K, Jayson GC. Experimentally-derived functional form for a population-averaged high-temporal-resolution arterial input function for dynamic contrast-enhanced MRI. Magn Reson Med 2006;56(5):993-1000.
71. Yankeelov TE, Luci JJ, Lepage M, Li R, Debusk L, Lin PC, Price RR, Gore JC. Quantitative pharmacokinetic analysis of DCE-MRI data without an arterial input function: a reference region model. Magn Reson Imaging 2005;23(4):519-529.
72. Tofts PS, Brix G, Buckley DL, Evelhoch JL, Henderson E, Knopp MV, Larsson HB, Lee TY, Mayr NA, Parker GJ, Port RE, Taylor J, Weisskoff RM. Estimating kinetic parameters from dynamic contrast-enhanced T(1)-weighted MRI of a diffusable tracer: standardized quantities and symbols. J Magn Reson Imaging 1999;10(3):223-232.
73. Kety SS. The theory and applications of the exchange of inert gas at the lungs and tissues. Pharmacol Rev 1951;3(1):1-41.

74. Shames DM, Kuwatsuru R, Vexler V, Muhler A, Brasch RC. Measurement of capillary permeability to macromolecules by dynamic magnetic resonance imaging: a quantitative noninvasive technique. Magn Reson Med 1993;29(5):616-622.
75. Faranesh AZ, Kraitchman DL, McVeigh ER. Measurement of kinetic parameters in skeletal muscle by magnetic resonance imaging with an intravascular agent. Magn Reson Med 2006;55(5):1114-1123.
76. Daldrup H, Shames DM, Wendland M, Okuhata Y, Link TM, Rosenau W, Lu Y, Brasch RC. Correlation of dynamic contrast-enhanced MR imaging with histologic tumor grade: comparison of macromolecular and small-molecular contrast media. AJR Am J Roentgenol 1998;171(4):941-949.
77. Yankeelov TE, Gore JC. Dynamic Contrast Enhanced Magnetic Resonance Imaging in Oncology: Theory, Data Acquisition, Analysis, and Examples. Curr Med Imaging Rev 2009;3(2):91-107.
78. Marzola P, Degrassi A, Calderan L, Farace P, Nicolato E, Crescimanno C, Sandri M, Giusti A, Pesenti E, Terron A, Sbarbati A, Osculati F. Early antiangiogenic activity of SU11248 evaluated in vivo by dynamic contrast-enhanced magnetic resonance imaging in an experimental model of colon carcinoma. Clin Cancer Res 2005;11(16):5827-5832.
79. Haney CR, Fan X, Markiewicz E, Mustafi D, Karczmar GS, Stadler WM. Monitoring anti-angiogenic therapy in colorectal cancer murine model using dynamic contrast-enhanced MRI: comparing pixel-by-pixel with region of interest analysis. Technol Cancer Res Treat 2013;12(1):71-78.

CHAPTER IV

REPRODUCIBILITY OF STATIC AND DYNAMIC ^{18}F-FDG, ^{18}F-FLT, AND ^{18}F-FMISO MICROPET STUDIES IN A MURINE MODEL OF HER2+ BREAST CANCER

Introduction

Current radiographic analysis for monitoring anticancer treatments is based on the response evaluation criteria in solid tumors (RECIST), which measures response using changes in a unidimensional measurement (1). With the development of novel therapeutics that target specific molecular pathways of breast cancer and the microenvironment (2), RECIST may not be the most sensitive or accurate approach (3). Three techniques that have been investigated as surrogate biomarkers of tumor response are 2-deoxy-2-^{18}F-fluoro-D-glucose (^{18}F-FDG), 3'-deoxy-3'-^{18}F-fluorothymidine (^{18}F-FLT), and ^{18}F-fluoromisonidazole (^{18}F-FMISO) positron emission tomography (PET), the specifics of which are described with more detail in Chapter III. Briefly, ^{18}F-FDG provides an assessment of glucose metabolism as its accumulation is regulated by glucose transporters and hexokinase activity (3). As ^{18}F-FLT accumulation is regulated by the cell-cycle dependent thymidine salvage pathway and activity of thymidine kinase 1, it reflects DNA synthesis and thus cell proliferation (4). ^{18}F-FMISO is a radiolabeled nitroimidazole that accumulates in regions of low oxygen content, and thus provides a measurement of hypoxia (4). These molecular imaging techniques may provide more insight than RECIST into the assessment of disease response, as high glycolytic index,

increased proliferative activity, and regions with elevated hypoxia are hallmarks of malignant tumors (5). Indeed, PERCIST, or PET response evaluation criteria in solid tumors, was developed as a potentially more sensitive method to assess response to treatments that are cytostatic rather than cytocidal (1). PERCIST assesses response using the change from baseline in the standardized uptake value normalized to a reference tissue from ^{18}F-FDG PET scans. With the increasing use of these techniques in preclinical studies to measure response to targeted therapies (6,7), investigating reproducibility is important to understand whether changes in imaging metrics during therapeutic interventions reflect changes in underlying biology rather than measurement error (8-10). The objectives of this study were to characterize static reproducibility of ^{18}F-FDG, ^{18}F-FLT, and ^{18}F-FMISO, as well as dynamic ^{18}F-FLT and ^{18}F-FMISO microPET studies in a murine model of HER2+ breast cancer. A portion of this chapter was previously published by Whisenant et al. in Molecular Imaging and Biology in 2012 (11).

Materials and Methods

Cell Culture

Trastuzumab-resistant breast cancer cells (HR6; gifted from Dr. Carlos Arteaga at Vanderbilt University) were harvested from BT474 xenografts that initially responded but then recurred in the presence of maintained trastuzumab treatment as described previously (12). HR6 cells were cultured in improved minimal essential medium (IMEM, Invitrogen, Carlsbad, CA) supplemented with 10% fetal bovine serum at 37 ^{o}C in a humidified, 5% CO_2 incubator. To maintain trastuzumab resistance, HR6 cells were co-

cultured with 10 mg/ml trastuzumab as previously described (12). Cells were harvested with trypsin at approximately 85% confluence.

Tumor Xenograft Model

Female athymic nude mice (n = 13, 4-6 weeks, Harlan, Indianapolis, IN) were implanted with 0.72 mg, 60-day release, 17β-estradiol pellets (Innovative Research of America, Sarasota, FL). Twenty-four hours later, approximately 10^7 HR6 cells, suspended in a 1:10 ratio of growth factor-reduced Matrigel and IMEM, were injected subcutaneously into the right flank. A 26-gauge jugular catheter was surgically implanted for radiotracer delivery. The mean tumor volume at start of imaging was 223 mm^3 [range: 103 mm^3 – 312 mm^3], and the average mouse weight during imaging was 22.0 g [range: 18 g – 25 g]. Mice were anesthetized with 2% isoflurane in pure oxygen for all surgical procedures. All animal procedures were approved by Vanderbilt University's Animal Care and Use Committee.

Radiotracer Synthesis

PETNET synthesized ^{18}F-FDG with a specific activity greater than 37 TBq/mmol. ^{18}F-FLT and ^{18}F-FMISO were prepared as a service by the radiochemistry core with average specific activities of 128.76 TBq/mmol and 66.6 TBq/mmol, respectively, following standard protocols (13,14).

Imaging Sessions

Test-retest scans were performed on 12 mice for each radiotracer. All mice except one were imaged with all three radiotracers. (A minimum of 48 hours occurred between test-retest scans using different radiotracers.) Mice were anesthetized using 2% isoflurane in pure oxygen, and animal body temperature was maintained by a heated water pad and heat lamp. List-mode data were collected for 60 minutes using a microPET Focus 220 system (Concorde Microsystems Inc., Knoxville, TN (14)) before, during, and after injection of 11.0 ± 2.0 MBq of ^{18}F-FDG, ^{18}F-FLT, or ^{18}F-FMISO diluted in 100 μL of sterile saline, and reconstructed into a 64-frame dynamic sequence (5x12 s, 59x60 s). A second scan with a repeat injection was performed approximately six hours after the first injection. Six hours was chosen such that the radioactivity of the first scan would decay at least three half-lives; it was assumed that minimal tumor changes occurred during this period (8,9). A five-minute static scan was acquired just prior to the second injection to correct for residual activity, as a 2-fold decrease in coefficient of variation between repeated scans was previously observed using this method (9).

All microPET images were reconstructed using the 3D ordered-subsets expectation maximization (OSEM3D) (nine subsets) followed by a maximum a posteriori (MAP), 18 iterations, beta value 0.038. As the amount of attenuation in microPET studies of mice is small compared to human studies and significant differences between animals are not expected (14), attenuation and scatter correction were not performed.

Animals were fasted four hours (8) and warmed one hour (15) prior to each ^{18}F-FDG injection. After the first scan, animals recovered from anesthesia, were given access to food for one hour, then fasted another four hours prior to the second scan (8). It was

not necessary to fast prior to ^{18}F-FLT imaging as significant differences in radiotracer accumulation between a fed or fasted state have not been observed in mice (9); we assumed this condition held true for ^{18}F-FMISO, thus animals were not fasted for those studies either.

Image Analysis

Regions of interest (ROIs) were drawn around the entire tumor volume using MATLAB (The MathWorks, Natick, MA, USA). The mean ROI activity from the last 10 minutes of each dynamic scan was normalized by the injected dose to calculate percent-injected dose per gram (%ID/g). Average activity from tumor voxels was calculated at each dynamic frame to construct time-activity curves (TACs). The ROI activities and TACs from scan 2 were adjusted by subtracting the activity from the five-minute static scan to eliminate residual activity.

Compartmental modeling requires the time rate of change of radiotracer activity concentration in the blood plasma. As the gold-standard for making this measurement, blood sampling (16), is not feasible for repeat studies in mice due to their small blood volume, we used the method developed by Kim et al. to obtain image-derived input functions (IDIFs) from ^{18}F-FLT dynamic data (17). This method generates TACs from the left ventricle and corrects for partial-volume effects using a recovery coefficient (RC). In our implementation, we obtained TACs from cylindrical ROIs across three slices. A RC of 0.72 was determined from phantom studies acquired under similar acquisition conditions as described previously (18). An identical procedure was followed for ^{18}F-FMISO. To the best of our knowledge, validation of an IDIF for ^{18}F-FMISO

microPET studies in mice has not been published; a point we return to in the Discussion.

Due to the relatively low spatial resolution, coupled with myocardial spillover and partial-volume effects, the IDIF from user-defined ROIs cannot be used for ^{18}F-FDG. (16). Several groups have developed mathematical models to derive the input function from ^{18}F-FDG image data (16,19) or use hybrid TACs from other organs (18); however, these methods require at least one blood sample. Blood samples were not collected in this study, thus we were unable to assess ^{18}F-FDG dynamic reproducibility.

Kinetic Modeling

We employed a 3-compartment model (shown in Figure IV-1) with rate constants K_1-k_4, that for ^{18}F-FLT represent the rate of transport between plasma and tissue, rate of outflow from the tissue to plasma, thymidine kinase 1 phosphorylation rate, and the dephosphorylation rate, respectively. Similar definitions apply for the ^{18}F-FMISO kinetic parameters except k_3 and k_4 represent rates of reduction/retention and re-oxidation, respectively.

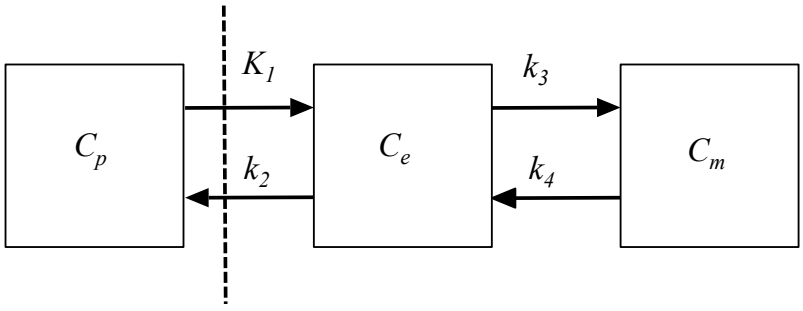

Figure IV-1. A standard, 3-compartment, 4-rate constant model used to analyze PET dynamic data. C_p represents the radiotracer activity concentration in the plasma. The tissue is composed of two compartments, the exchangeable compartment, C_e, and the metabolized or trapped compartment, C_m. The parameters K_1-k_4 represent rate constants that describe transport between compartments.

As sensitivity assessments performed by Muzi et al. showed high covariance between K_1 and k_2 in tumors (15), we combined those parameters and performed model fitting with K_1, V_d (=K_1/k_2, the initial volume of distribution), k_3, and k_4. Data were analyzed using four parameters assuming reversible phosphorylation ($k_4 \neq 0$) and three parameters assuming irreversible phosphorylation ($k_4 = 0$). Modeling also included the blood volume fraction (V_b). Model fitting used a nonlinear least-squares method with the governing differential equations, parameter ranges, and initial guesses described previously (also listed in Table IV-1) (15). We also calculated the net tracer influx constant (K_i):

$$K_i = \frac{K_1 \cdot k_3}{\frac{K_1}{V_d} + k_3}. \qquad \text{(IV-1)}$$

Table IV-1. Initial guesses and parameter ranges for PET kinetic modeling

Parameter (units)	Initial Guess	Parameter Range
K_1 (mL/min/g)	0.1	0.0 - 0.5
V_d (K_1/k_2) (mL/g)	1	0.1 - 5.0
k_3 (min^{-1})	0.1	0.001 - 1.0
k_4 (min^{-1})	0.02	0.001 - 0.2
V_b (mL/g)	0.05	0.0 - 0.1

The Akaike Information Criterion (AIC) was calculated to determine the most parsimonious kinetic model for ^{18}F-FLT and ^{18}F-FMISO (16). For the least-squares case, the AIC with a bias correction for small samples is:

$$\mathrm{AIC} = \mathrm{n} \cdot \ln\left(\frac{\mathrm{RSS}}{\mathrm{n}}\right) + 2\mathrm{k} + \frac{2\mathrm{k}(\mathrm{k}+1)}{\mathrm{n}-\mathrm{k}-1}, \qquad \text{(IV-2)}$$

where *RSS* is the residual sum of squares, *n* number dynamic frames, and *k* number of model parameters. Average AIC was calculated for each model, and reproducibility was assessed for the model with the lowest AIC.

Reproducibility Statistics

Statistical methods for evaluating reproducibility follow Bland and Altman (17) as implemented by Galbraith et al. (18). For each mouse, the difference between parameter measurements (*d)* was calculated. The distribution of *d* was tested for normality with the Shapiro-Wilk test, and the Kendall's tau test was used to determine if *d* correlated with the mean. A Wilcoxon signed-rank test was performed to test the null hypothesis of no bias between repeated measurements. A significance value of $p < 0.05$ was used for all statistical tests.

The following statistical calculations were performed:

1. Mean squared difference (dsd) is computed as the standard deviation of *d*. The dsd is then used to calculate the 95% confidence interval (CI), which provides a threshold of measurement error in a group of *n* mice:

$$\mathrm{CI} = \pm \frac{\mathrm{tstat} \cdot \mathrm{dsd}}{\sqrt{\mathrm{n}}}, \tag{IV-3}$$

   where tstat is the appropriate t-statistic corresponding to the sample size. Any change in the population greater than this value would reflect changes in the underlying biology.

2. Within-subject standard deviation (wSD) is:

$$\mathrm{wSD} = \frac{\mathrm{dsd}}{\sqrt{2}}. \tag{IV-4}$$

3. Repeatability coefficient (r) is:

$$r = 2.77 \cdot wSD, \quad \text{(IV-5)}$$

and indicates that the difference between two measurements will be less than this value for 95% of observation pairs.

If the mean parameter difference is correlated with the mean (Kendall's tau, $p < 0.05$), the data would need to be transformed to a $\log_{10}$ scale and Eqs. (IV-3) - (IV-5) would need to be modified accordingly (18).

To compare our results with previous reproducibility studies (8,9), we calculated the coefficient of variation (CV) by dividing the standard deviation of the two measurements by the mean. Statistical analyses were performed using Microsoft Excel (Redmond, WA) and statistical toolbox in MATLAB.

Results

Static Reproducibility

Twelve data sets were analyzed for ^{18}F-FDG; one animal was removed from each of the ^{18}F-FLT and ^{18}F-FMISO data sets due to a large variation in injected activity between scans. Examples of repeated %ID/g parametric images are shown in Figure IV-2. No parameter had a mean difference significantly different from normal except ^{18}F-FLT ($p = 0.011$). However, the conclusion that a population does or does not follow a Gaussian distribution may be incorrect for small sample sizes due to insufficient power of the normality test (19); thus, reproducibility statistics were still performed for ^{18}F-FLT %ID/g. No parameter had a dependence of d on the mean, thus a logarithmic transformation was not required.

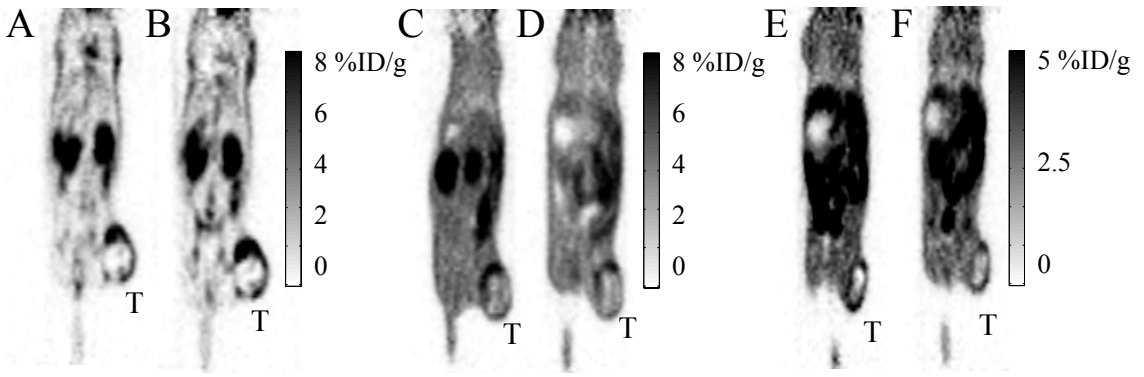

Figure IV-2. Coronal sections of HR6 xenografts (T) showing static reproducibility of ^{18}F-FDG (panels A, B), ^{18}F-FLT (panels C, D), and ^{18}F-FMISO (panels E, F). Please note how the HER2+ xenografts are clearly visible for accurate tumor segmentation.

Reproducibility statistics for %ID/g are listed in Table IV-2. Bland-Altman plots for each radiotracer are displayed in Figure IV-3, with each panel plotting the mean difference between repeated scans against the mean %ID/g. The mean difference (solid line) is also shown with 95% CIs (dotted line) that represent the required change to surpass the expected measurement variability for a group of mice, which is ± 0.62 (14%), ± 0.23 (5%), and ± 0.24 (6%) for ^{18}F-FDG, ^{18}F-FLT, or ^{18}F-FMISO, respectively. Repeatability ranges (dashed line) are ± 1.9, ± 0.66, or ± 0.69 for ^{18}F-FDG, ^{18}F-FLT, or ^{18}F-FMISO, respectively. The CVs for %ID/g (mean ± SD) are 11.4% ± 10.6%, 4.0% ± 3.8%, and 6.0% ± 3.8% for ^{18}F-FDG, ^{18}F-FLT, and ^{18}F-FMISO, respectively.

Table IV-2. Reproducibility statistics for %ID/g

Radiotracer	Mean difference	95% CI for mean difference	wSD	Repeatability	CV (mean±SD)
^{18}F-FDG	-0.01	±0.62 (14%)	0.69	1.9	11.4%±10.6%
^{18}F-FLT[a]	-0.09	±0.23 (5%)	0.24	0.66	4.0%±3.8%
^{18}F-FMISO	-0.16	±0.24 (6%)	0.25	0.69	6.0%±3.8%

[a] Normality cannot be assumed

CI, confidence interval; wSD, within-subject standard deviation; CV, coefficient of Variation

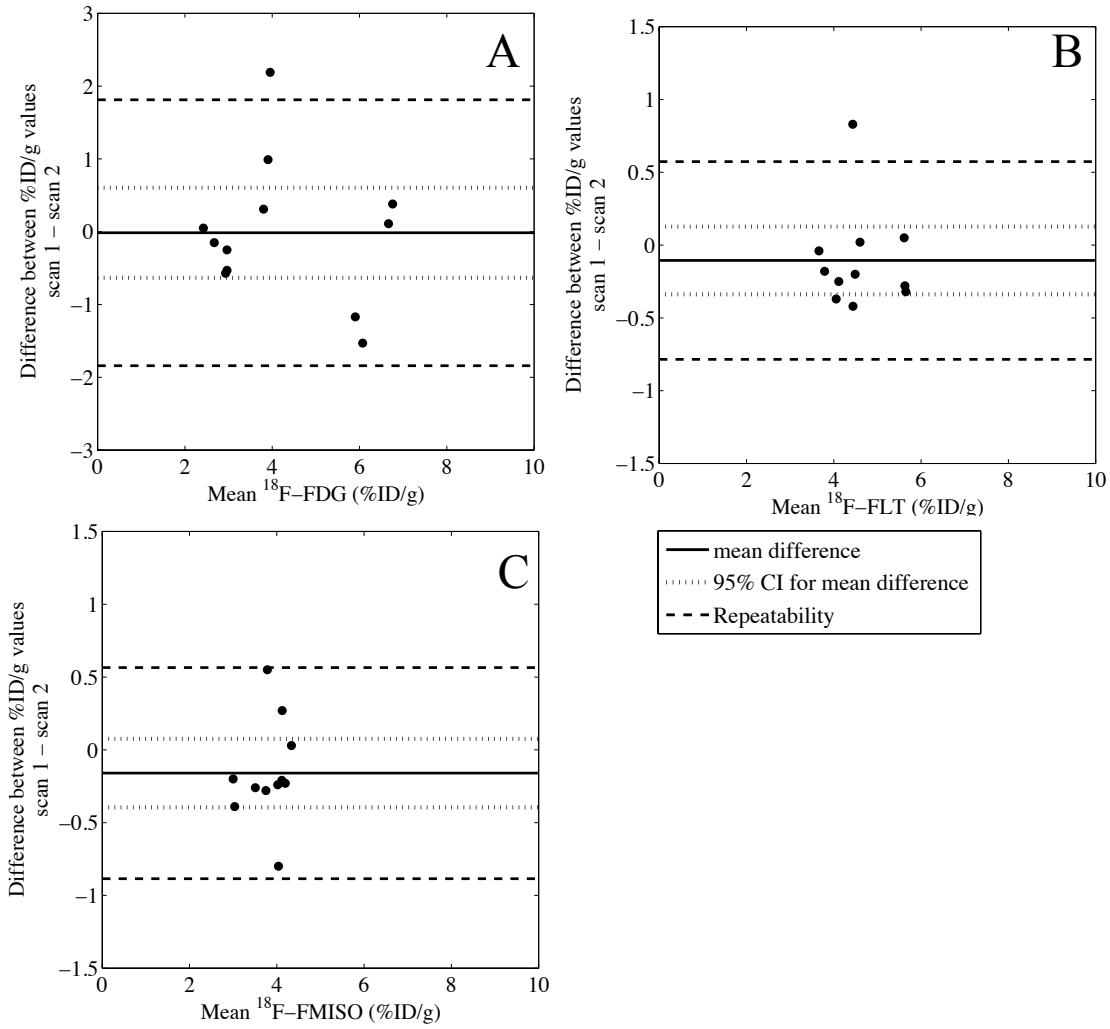

Figure IV-3. Bland-Altman plots displaying mean %ID/g plotted against mean parameter difference between repeat scans for ^{18}F-FDG (panel a), ^{18}F-FLT (panel b), and ^{18}F-FMISO (panel c). The mean difference (solid line) is shown with 95% confidence intervals (dotted lines) for the population. Repeatability is also shown (dashed lines), which represents the threshold of required change in an individual mouse.

The percentage values for the 95% CIs will change with the mean. We note that the absolute values are appropriate when determining measurement error (18), however the percentage values are easier to interpret in a longitudinal study when parameter changes are normalized to baseline as is commonly done. The reader is encouraged to

refer to Table IV-2 for the absolute values, however the 95% CIs will be quoted as a percentage when defining the threshold of change in a mouse cohort.

^{18}F-FLT Dynamic Reproducibility

Two additional data sets from the static reproducibility analysis were excluded due to abnormal TACs for the liver and kidney (n = 1) and the left ventricle not easily located on the images (n = 1), resulting in nine usable data sets. The AIC (mean ± SD) for the 4-parameter and 3-parameter models were 739 ± 44 and 758 ± 51, respectively. Reproducibility was assessed using the 4-parameter model, as it had the lowest AIC. Figure IV-4 shows an example of a repeated dynamic ^{18}F-FLT data set, where the TACs from the left ventricle and tumor are shown in panels A and B, respectively. The 4-parameter model fits are also shown, and the kinetic parameter values for each scan were: K_1, 0.031 and 0.038; V_d, 0.629 and 0.578; k_3, 0.027 and 0.029; k_4, 0.091 and 0.061; K_{FLT}, 0.011 and 0.012.

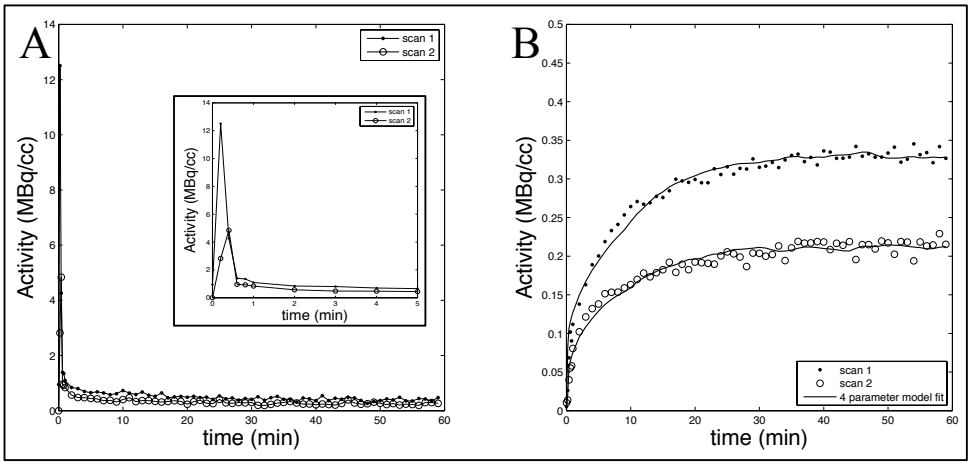

Figure IV-4. Representative example of ^{18}F-FLT dynamic reproducibility. Left ventricle time-activity curves for both scans (A) are shown over the entire 60 minute acquisition, with the inset figure displaying the first five minutes. Tumor time-activity curves from each scan (B) are shown with curve fits from the most parsimonious kinetic model (4-parameter fit, determined by AIC analysis).

^{18}F-FLT dynamic reproducibility statistics are listed in Table IV-3 (a). No parameter was significantly different from normal, and no systematic bias was detected among repeats for any kinetic parameter. Additionally, the variability associated with each parameter was independent of the mean, thus no logarithmic transformation was required. Bland-Altman plots for each kinetic parameter are displayed in Figure IV-5; similar to Figure IV-3, the mean difference is graphed with 95% CIs and repeatability ranges. V_d, k_3, and K_{FLT} were the most reproducible parameters, with 95% CIs of ± 18%, ± 10%, ± 18%, respectively. Results for K_1 and k_4 were more variable, with 95% CIs of ± 33% and ± 43%, respectively. The repeatability coefficients for K_1, V_d, k_3, k_4, and K_{FLT} were ± 0.035, ± 0.231, ± 0.007, ± 0.07, and ± 0.005, respectively. To compare dynamic reproducibility results with %ID/g, the CVs (mean ± SD) for K_1, V_d, k_3, k_4, and K_{FLT} were 25% ± 16%, 14% ± 9%, 6% ± 5%, 28% ± 27%, and 14% ± 9%, respectively.

Table IV-3. Dynamic reproducibility for (a) ^{18}F-FLT and (b) ^{18}F-FMISO

Parameter	Mean	Mean difference	95% CI for mean difference	wSD	Repeatability	CV (mean ± SD)
(a) ^{18}F-FLT with 4-parameter fit						
K_1	0.042	-0.012	±0.014 (33%)	0.012	0.035	25% ± 16%
V_d (K_1/k_2)	0.501	0.013	±0.091 (18%)	0.083	0.231	14% ± 9%
k_3	0.031	-0.001	±0.003 (10%)	0.003	0.007	6% ± 5%
k_4	0.065	-0.006	±0.028 (43%)	0.025	0.07	28% ± 27%
K_{FLT}	0.011	-0.001	±0.002 (18%)	0.002	0.005	14% ± 9%
(b) ^{18}F-FMISO with 3-parameter fit						
K_1	0.04	-0.007	±0.010 (25%)	0.008	0.022	21% ± 13%
V_d (K_1/k_2)	0.473	0.042	±0.075 (16%)	0.058	0.16	11% ± 7%
k_3	0.019	0.003	±0.008 (42%)	0.006	0.017	22% ± 13%
K_{FMISO}	0.007	0.001	±0.001 (14%)	0.001	0.003	11% ± 12%

CI, confidence interval; wSD, within-subject standard deviation; CV, coefficient of variation

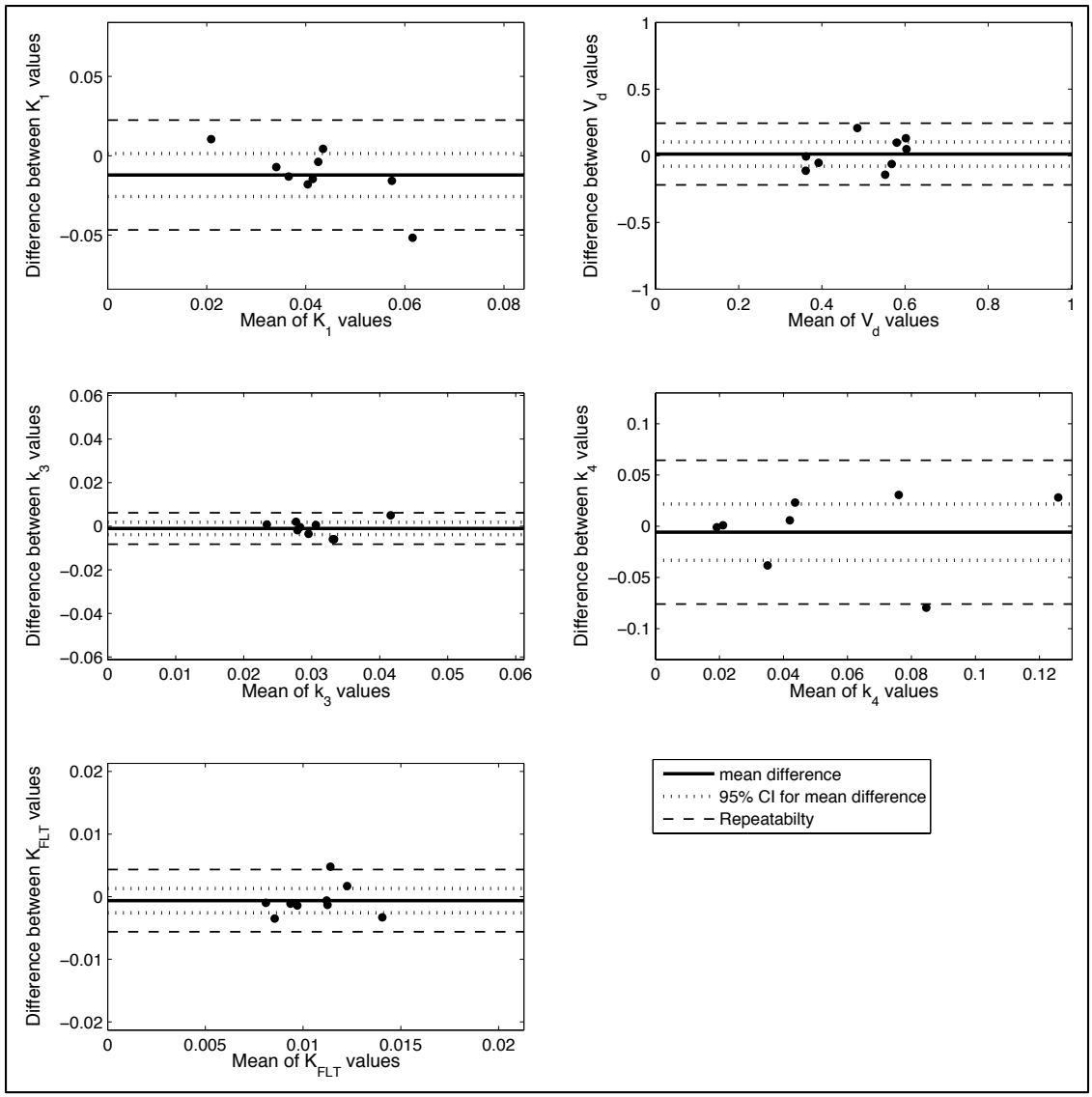

Figure IV-5. Bland-Altman plots displaying mean of each ^{18}F-FLT kinetic parameter plotted against the mean difference between scans. The mean difference (solid line) is shown with 95% confidence intervals (dotted lines) for the population. Repeatability is also shown (dashed lines) for each parameter, which represents the threshold of required change in an individual mouse.

^{18}F-FMISO Dynamic Reproducibility

Four additional data sets from the static reproducibility analysis were excluded due to abnormal liver and kidney TACs (n = 4), resulting in seven useable data sets. The AIC (mean ± SD) for the 4-parameter and 3-parameter models were 756 ± 42 and 747 ±

39, respectively. Reproducibility was assessed using the 3-parameter model, as it had the lowest AIC. Figure IV-6 shows an example of repeated dynamic ^{18}F-FMISO data, where the TACs from the left ventricle and tumor are shown in panels A and B, respectively. The 3-parameter model fits are also shown, and the kinetic parameter values for each scan were: K_1, 0.028 and 0.035; V_d, 0.432 and 0.35; k_3, 0.014 and 0.02; K_{FMISO}, 0.005 and 0.006.

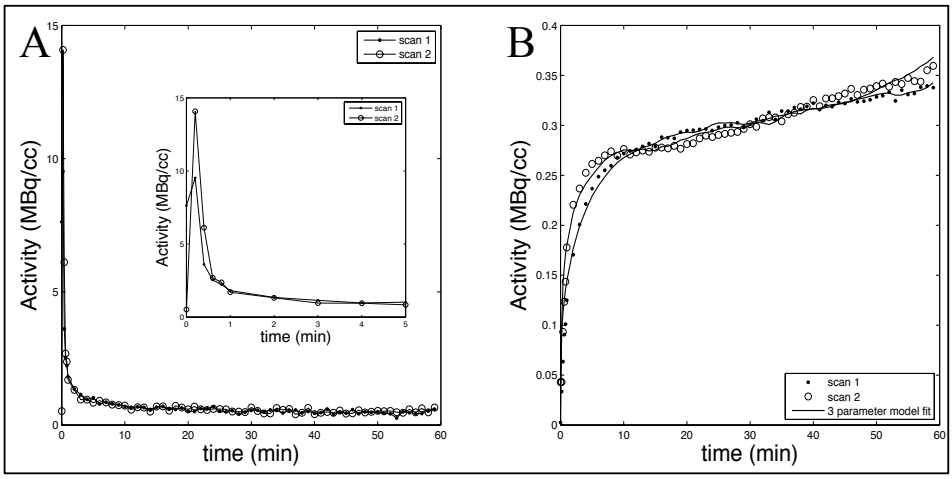

Figure IV-6. Representative example of ^{18}F-FMISO dynamic reproducibility. Left ventricle time-activity curves for both scans (A) are shown over the entire 60 minute acquisition, with the inset figure displaying the first five minutes. Tumor time-activity curves of each scan (B) are shown with curve fits from the most parsimonious kinetic model (3-parameter fit, determined by AIC analysis).

^{18}F-FMISO dynamic reproducibility statistics are listed in Table IV-3 (b). No kinetic parameter was significantly different from normal, and no systematic bias was detected among repeats for any parameter. Additionally, no parameter had a significant dependence of d on the mean, thus no logarithmic transformation was required. Bland-Altman plots for each ^{18}F-FMISO kinetic parameter are displayed in Figure IV-7; again, the mean difference is graphed with 95% CIs and repeatability ranges. V_d and K_{FMISO} were the most reproducible with the lowest 95% CIs of ± 16% and ± 14%, respectively.

Results for K_1 and k_3 were more variable, with 95% CIs of ± 25% and ± 42%, respectively. The repeatability coefficients for K_1, V_d, k_3, and K_{FLT} were ± 0.022, ± 0.16, ± 0.017, and ± 0.003, respectively. To compare dynamic reproducibility results with %ID/g, the CVs (mean±SD) for K_1, V_d, k_3, and K_{FMISO} were 22% ± 13%, 11% ± 7%, 24% ± 13%, and 12% ± 13%, respectively.

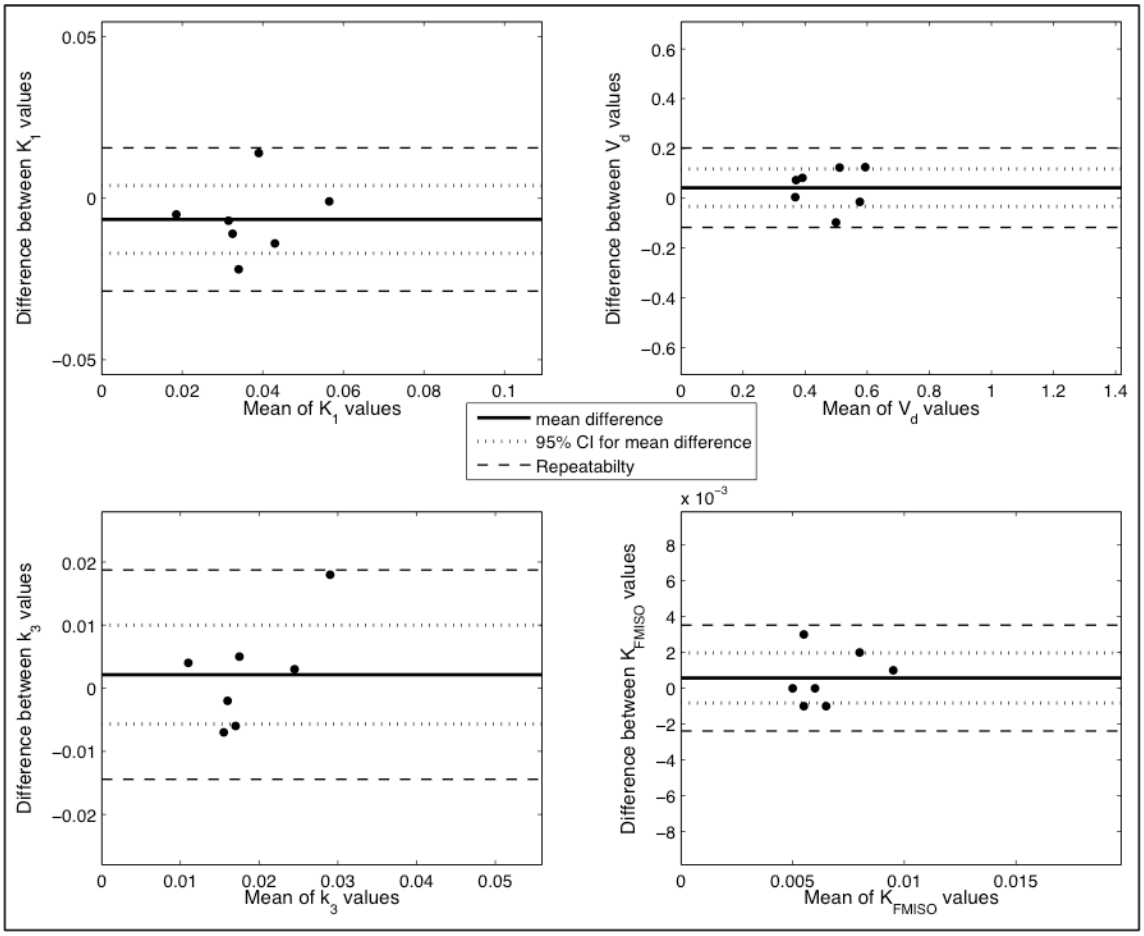

Figure IV-7. Bland-Altman plots displaying mean of each ^{18}F-FMISO kinetic parameter plotted against the mean difference between scans. The mean difference (solid line) is shown with 95% confidence intervals (dotted lines) for the population. Repeatability is also shown (dashed lines) for each parameter, which represents the threshold of required change in an individual mouse.

Discussion

Reproducibility for individuals or groups can be described by several statistical metrics. The 95% CIs of the mean difference in Tables IV-2 and IV-3 dictate thresholds by which greater changes would reflect tumor physiology rather than measurement variability in groups of similar size to our study. For individuals, the repeatability coefficient represents the required threshold of change. Both the 95% CI and repeatability coefficient are useful in, for example, a treatment response study where the objective is to quantify changes in parameters after a specific therapy. For example, ^{18}F-FDG %ID/g needs to either increase or decrease by 1.9 for individuals or 14% in a group analysis to reflect a treatment-induced change, whereas ^{18}F-FLT can be used to detect a change in %ID/g of ± 0.66 in individual tumors or ± 5% in a group. These measurement uncertainties are not unreasonable, and much higher changes due to therapy have been reported in preclinical studies of cancer (6,7).

Our results are comparable to previously published ^{18}F-FDG and ^{18}F-FLT static reproducibility *via* the CV. Average CV observed by Dandekar et al. (8) and Tseng et al. (9) for whole tumor ROIs were 15.4% and 14% for ^{18}F-FDG and ^{18}F-FLT, respectively. We observed CVs that were 4% and 10% less than the previous studies for ^{18}F-FDG and ^{18}F-FLT, respectively. This difference in measurement uncertainty could be attributed to differences in animal preparation and PET data reconstruction. We used jugular vein catheters that are implanted into the animal once, while the previous studies used tail vein catheters which can be quite difficult to place. A difficult catheter placement could cause activity accumulation in the tail due to a less than optimal tracer injection. Additionally, the two previous studies used an OSEM image-reconstruction algorithm. Disselhorst et al.

investigated the effect of different reconstruction algorithms on PET image quality, and observed that OSEM3D followed by MAP increased overall image quality by increasing the recovery coefficient, and lowering the spillover ratio and percent standard deviation of the noise. (20). The improved image quality obtained by using an OSEM3D-MAP algorithm would decrease measurement error; however, the slight differences in animal handling procedures and the uncontrollable variable that is animal stress between scans affects ^{18}F-FDG accumulation and would increase measurement error (21). This may explain why we observed a much lower CV for ^{18}F-FLT and a similar CV to the previous study for ^{18}F-FDG.

Measurements of tracer uptake normalized to the injected dose are straightforward to acquire, however changes in tracer clearance from the blood or tumor metabolism are not considered (22). Performing measurements that use the full dynamic curve of tracer retention/metabolism can overcome some of these issues. However, dynamic acquisitions and compartmental modeling can be complex and can introduce additional sources of noise in the measurement, which in turn, lowers reproducibility as has been observed previously (22) and also in our study.

One potential parameter of interest in a tumor response study with dynamic ^{18}F-FLT is K_{FLT}, which was the second most reproducible dynamic parameter after k_3. The 95% CI for K_{FLT} is ± 18%, suggesting that a change greater than ± 18% would reflect true treatment differences in a mouse cohort (n = 9). A larger difference in K_{FLT} due to treatment has been observed in a murine model of prostate cancer (23). The least reproducible parameter was k_4, which agrees with the large error previously reported (10), especially when using a 60-minute dynamic acquisition (22). The greater variability in K_1

(compared to K_{FLT}) may be because it is more sensitive to changes in the model input function and/or tracer injection; a similar phenomenon has been reported for ^{18}F-FMISO data (24) as well as dynamic contrast enhanced MRI (18). Using a power injector with a constant injection rate instead of a manual injection may lower variability in this parameter.

The only published ^{18}F-FLT dynamic reproducibility study in mice reported measurement error as the mean ± standard deviation of the percent difference (10). Choi et al. concluded that a parameter was reproducible if the standard deviation of the percent difference was ≤ 20%. The kinetic parameters that fit this criterion from their study were K_{FLT} (17.5%) for A431 tumors, and K_1 (19.7%), V_d (17.4%), and k_3 (8.6%) for LLC tumors (10). The parameters that fit this criterion from our study were V_d (13%), k_3 (6.4%), and K_{FLT} (13%).

The use of static ^{18}F-FMISO measurements to assess treatment response is increasing, however to the best of our knowledge a 3-compartment analysis of tracer accumulation within a treatment response protocol has not been performed. Thus, we can only hypothesize that the observed measurement errors for ^{18}F-FMISO are reasonable and the kinetic parameters can be used to reliably assess tumor response. The most reproducible parameter is K_{FMISO}, which might be of interest in a treatment response study as this parameter provides both a measure of tracer perfusion as well as tracer retention and/or trapping. For K_{FMISO}, a change greater than ± 14% would reflect changes due to treatment in a mouse cohort (n = 7) instead of measurement variability.

As mentioned previously, validation of an IDIF for ^{18}F-FMISO microPET studies in mice has not been published. However, an IDIF from ROIs within the carotid artery

has been used in a human study to assess ^{18}F-FMISO pharmacokinetics in cancer (25). Using a large blood pool such as the left ventricle or carotid artery for an IDIF is reasonable as these tissues are not normally hypoxic and therefore retention of ^{18}F-FMISO in those tissues should be minimal.

Study Limitations

We noted in the Results section that ^{18}F-FLT %ID/g test-retest measurements failed normality testing; however interpreting results from normality tests with small samples can be difficult. Indeed, a large *p*-value does not guarantee that the data follow a Gaussian distribution with small sample sizes (19). Therefore, we computed the reproducibility statistics knowing that the statistical methods depend strongly on the assumption of normally distributed data. The two previous static reproducibility studies (8,9) did not perform the statistical methods outlined in this work, instead concluded that the threshold of required change in an individual mouse would be twice that of the CV. Following their analysis with our data, threshold of change for ^{18}F-FLT %ID/g is ± 8% (twice the CV) in an individual mouse. Our reproducibility results are more conservative, and the repeatability coefficient as a percentage of the mean is ± 14%.

The anesthesia used in this study was 2% isoflurane in pure oxygen. A previous study has shown that the use of pure oxygen lowers accumulation of ^{18}F-FMISO, thereby potentially leading to systematic errors in the measurement of tumor hypoxia (26). However, the measurement error associated with the actual imaging protocol should not change depending on the anesthesia method.

Changes in physiological variables (e.g. blood glucose, cardiac output, and tracer

metabolic rates of tumors), scanner electronics efficiency, or radiotracer specific activities might increase longitudinal variability. The ability to generalize these same day test-retest reproducibility results to the variability of serial studies is important. To minimize these sources of error, it is imperative to develop and strictly follow a well-designed imaging protocol. Furthermore, implementing quantitative methods to normalize imaging data could prove beneficial if, for example, changes in blood glucose and scanner electronic drift become significant sources of variability during longitudinal studies.

Conclusion

Imaging biomarkers that can detect early changes in specific molecular characteristics of tumors would greatly benefit both preclinical and clinical cancer studies. Before an imaging biomarker can be employed to assess treatment response, reproducibility must be assessed. In this study, we assessed static reproducibility for ^{18}F-FDG, ^{18}F-FLT, and ^{18}F-FMISO, as well as dynamic ^{18}F-FLT and ^{18}F-FMISO microPET data. Our test-retest analyses of %ID/g measurements were very reproducible (95% CI < ± 14%). Although, the kinetic analysis of ^{18}F-FLT and ^{18}F-FMISO resulted in higher measurement error, the variability associated with the net influx constants (K_{FLT} and K_{FMISO}) is reasonable (95% CI < ± 19%). Our study indicates that static and dynamic measurements of these radiotracers can be used in serial studies to measure changes in tracer metabolism following anticancer therapies in mouse models of HER2+ human breast cancer.

References

1. Wahl RL, Jacene H, Kasamon Y, Lodge MA. From RECIST to PERCIST: Evolving Considerations for PET response criteria in solid tumors. J Nucl Med 2009;50 Suppl 1:122S-150S.
2. Guarneri V, Barbieri E, Dieci MV, Piacentini F, Conte P. Anti-HER2 neoadjuvant and adjuvant therapies in HER2 positive breast cancer. Cancer Treat Rev 2010;36 Suppl 3:S62-66.
3. Harry VN, Semple SI, Parkin DE, Gilbert FJ. Use of new imaging techniques to predict tumour response to therapy. Lancet Oncol 2010;11(1):92-102.
4. Dunphy MP, Lewis JS. Radiopharmaceuticals in preclinical and clinical development for monitoring of therapy with PET. J Nucl Med 2009;50 Suppl 1:106S-121S.
5. Hanahan D, Weinberg RA. Hallmarks of cancer: the next generation. Cell 2011;144(5):646-674.
6. Brepoels L, Stroobants S, Verhoef G, De Groot T, Mortelmans L, De Wolf-Peeters C. (18)F-FDG and (18)F-FLT uptake early after cyclophosphamide and mTOR inhibition in an experimental lymphoma model. J Nucl Med 2009;50(7):1102-1109.
7. Oehler C, O'Donoghue JA, Russell J, Zanzonico P, Lorenzen S, Ling CC, Carlin S. 18F-fluromisonidazole PET imaging as a biomarker for the response to 5,6-dimethylxanthenone-4-acetic acid in colorectal xenograft tumors. J Nucl Med 2011;52(3):437-444.
8. Dandekar M, Tseng JR, Gambhir SS. Reproducibility of 18F-FDG microPET studies in mouse tumor xenografts. J Nucl Med 2007;48(4):602-607.
9. Tseng JR, Dandekar M, Subbarayan M, Cheng Z, Park JM, Louie S, Gambhir SS. Reproducibility of 3'-deoxy-3'-(18)F-fluorothymidine microPET studies in tumor xenografts in mice. J Nucl Med 2005;46(11):1851-1857.
10. Choi SJ, Kim SY, Kim SJ, Lee JS, Lee SJ, Park SA, Yun SC, Im KC, Oh SJ, Kim SW, Kim JS, Ryu JS, Moon DH. Reproducibility of the kinetic analysis of 3'-deoxy-3'-[(18)F]fluorothymidine positron emission tomography in mouse tumor models. Nucl Med Biol 2009;36(7):711-719.
11. Whisenant JG, Peterson TE, Fluckiger JU, Tantawy MN, Ayers GD, Yankeelov TE. Reproducibility of static and dynamic (18)F-FDG, (18)F-FLT, and (18)F-FMISO MicroPET studies in a murine model of HER2+ breast cancer. Mol Imaging Biol 2013;15(1):87-96.
12. Ritter CA, Perez-Torres M, Rinehart C, Guix M, Dugger T, Engelman JA, Arteaga CL. Human breast cancer cells selected for resistance to trastuzumab in vivo overexpress epidermal growth factor receptor and ErbB ligands and remain dependent on the ErbB receptor network. Clin Cancer Res 2007;13(16):4909-4919.
13. Tang G, Wang M, Tang X, Gan M, Luo L. Fully automated one-pot synthesis of [18F]fluoromisonidazole. Nucl Med Biol 2005;32(5):553-558.
14. Choi SJ, Kim JS, Kim JH, Oh SJ, Lee JG, Kim CJ, Ra YS, Yeo JS, Ryu JS, Moon DH. [18F]3'-deoxy-3'-fluorothymidine PET for the diagnosis and grading of brain tumors. Eur J Nucl Med Mol Imaging 2005;32(6):653-659.

15. Muzi M, Mankoff DA, Grierson JR, Wells JM, Vesselle H, Krohn KA. Kinetic modeling of 3'-deoxy-3'-fluorothymidine in somatic tumors: mathematical studies. J Nucl Med 2005;46(2):371-380.
16. Burnham KP, Anderson DR. Multimodal Inference: Understanding AIC and BIC in Model Selection. Sociological Methods Research 2004;33(2):261-304.
17. Bland JM, Altman DG. Measuring agreement in method comparison studies. Stat Methods Med Res 1999;8(2):135-160.
18. Galbraith SM, Lodge MA, Taylor NJ, Rustin GJ, Bentzen S, Stirling JJ, Padhani AR. Reproducibility of dynamic contrast-enhanced MRI in human muscle and tumours: comparison of quantitative and semi-quantitative analysis. NMR Biomed 2002;15(2):132-142.
19. Motulsky H. Analyzing Data with GraphPad Prism. San Diego, CA: GraphPad Software Inc; 1999.
20. Disselhorst JA, Brom M, Laverman P, Slump CH, Boerman OC, Oyen WJ, Gotthardt M, Visser EP. Image-quality assessment for several positron emitters using the NEMA NU 4-2008 standards in the Siemens Inveon small-animal PET scanner. J Nucl Med 2010;51(4):610-617.
21. Fueger BJ, Czernin J, Hildebrandt I, Tran C, Halpern BS, Stout D, Phelps ME, Weber WA. Impact of animal handling on the results of 18F-FDG PET studies in mice. J Nucl Med 2006;47(6):999-1006.
22. Shields AF, Lawhorn-Crews JM, Briston DA, Zalzala S, Gadgeel S, Douglas KA, Mangner TJ, Heilbrun LK, Muzik O. Analysis and reproducibility of 3'-Deoxy-3'-[18F]fluorothymidine positron emission tomography imaging in patients with non-small cell lung cancer. Clin Cancer Res 2008;14(14):4463-4468.
23. Lee SJ, Kang HY, Kim SY, Chung JH, Oh SJ, Ryu JS, Kim SB, Kang JS, Park SK, Kim HM, Kim MH, Moon DH. Early assessment of tumor response to JAC106, an anti-tubulin agent, by 3'-deoxy-3'-[(1)F]fluorothymidine in preclinical tumor models. Eur J Nucl Med Mol Imaging 2011;38(8):1436-1448.
24. Wang W, Georgi JC, Nehmeh SA, Narayanan M, Paulus T, Bal M, O'Donoghue J, Zanzonico PB, Schmidtlein CR, Lee NY, Humm JL. Evaluation of a compartmental model for estimating tumor hypoxia via FMISO dynamic PET imaging. Phys Med Biol 2009;54(10):3083-3099.
25. Wang W, Lee NY, Georgi JC, Narayanan M, Guillem J, Schoder H, Humm JL. Pharmacokinetic analysis of hypoxia (18)F-fluoromisonidazole dynamic PET in head and neck cancer. J Nucl Med 2010;51(1):37-45.
26. Kersemans V, Hueting R, Cornelissen B, Hussien K, Allen PD, Falzone N, Dilworth J, Gouverneur V, Muschel R, Smart S. Confounding factors arising from the use of anesthesia in preclinical imaging studies of 18F-FMISO as a diagnostic marker of hypoxia. J Nucl Med: Abstract Book Supplement 2011;52(1):72P-73P.

CHAPTER V

REPRODUCIBILITY OF DIFFUSION-WEIGHTED MAGNETIC RESONANCE IMAGING STUDIES IN A MURINE MODEL OF HER2+ BREAST CANCER

Introduction

Current radiographic analysis of treatment response is based on the Response Evaluation Criteria in Solid Tumors (RECIST), which uses one-dimensional changes in tumor size to determine response (1). However, it is well recognized that RECIST may not provide the most sensitive response assessment to novel and emerging therapies that target the molecular or cellular aspects of the tumor itself or, for example, its microenvironment (2,3). Development of imaging methods that can provide an earlier assessment of disease response is an active area of research, as it would allow for the initiation of alternative, potentially more effective, treatments while avoiding unnecessary toxicities associated with ineffective therapy. Diffusion-weighted magnetic resonance imaging (DW-MRI) has the potential to offer earlier assessments of disease response, as parameters derived from quantitative analyses of such data can be used to characterize treatment-induced alterations in tumor cell density (4-7).

The microscopic, thermally-induced behavior of molecules moving in a random pattern is referred to as self-diffusion or Brownian motion. The rate of diffusion in cellular tissues is described by an apparent diffusion coefficient (ADC), which is influenced by the number and separation of barriers that a diffusing water molecule encounters. DW-MRI maps the ADC, and in well-controlled situations, the variations in

ADC have been shown to correlate inversely with tissue cellularity (8). It has been shown, in preclinical (9-12) and clinical (13-15) settings, that exposure of tumors to both chemotherapy and radiotherapy consistently leads to measurable increases in water diffusion in cases of favorable treatment response.

In their 2009 DW-MRI review, Padhani et al. recommended that each imaging center determine the reproducibility of DW-MRI data at their institution to allow for proper study design and to assess the significance of treatment-induced changes (16). Reproducibility of clinical DW-MRI data have been previously assessed in normal and diseased tissues with a variety of image acquisition methods and data analyses including differences in the number and strength of diffusion-weighted images, as well as the reproducibility statistics themselves (17-20). However, there is a paucity of such data in the preclinical setting. With the increasing use of DW-MRI as a surrogate biomarker of response in preclinical studies (9,10,12), investigating reproducibility is imperative to interpret whether parameter changes during therapeutic interventions reflect tumor cellularity instead of measurement error in mouse models of disease. Thus, the objective of this study was to quantify DW-MRI reproducibility in a murine model of HER2+ breast cancer in order to assist in the interpretation of results collected from future longitudinal treatment response studies.

Materials and Methods

Animal and Tumor Xenograft Model

Trastuzumab-resistant breast cancer cells, HR6, were obtained from a generous gift from Dr. Carlos Arteaga, M.D. at Vanderbilt University. These cells were developed

by harvesting them from BT474 xenografts that initially responded but recurred in the presence of maintained trastuzumab; details are provided in (21). (This cell line was selected as it is part of an ongoing investigation of trastuzumab-resistance in breast tumors). Female athymic nude mice (n = 11, 4-6 weeks old, Harlan, Indianapolis, IN) were implanted with 0.72 mg, 60-day release, 17β-estradiol pellets (Innovative Research of America, Sarasota, FL). Twenty-four hours later, approximately 10^7 HR6 cells were injected subcutaneously into the right flank. Mice were anesthetized with 2% isoflurane in pure oxygen for both procedures. The mean tumor volume at start of imaging was 298 mm^3 (range: 136 mm^3 – 526 mm^3). All animal procedures were approved by our Institution's Animal Care and Use Committee.

Image Acquisition

Test-retest DW-MRI sessions were performed on 11 mice using a 7T MRI scanner (Agilent Technologies (formally Varian), Palo Alto, CA) equipped with a 38-mm quadrature RF coil (Doty Scientific, Columbia, SC). A second test-retest session was performed on one mouse one week after the first study, resulting in 12 useable data sets. Anesthesia was induced and maintained for each imaging session *via* 2% isoflurane in pure oxygen. Animal respiration rate was monitored, and animal body temperature was maintained at an external temperature of 32 ^{o}C by means of a flow of warm air directly into the bore of the magnet. Each animal was placed in a custom built restraint, and the tumor region was first localized *via* 3D gradient echo scout images. Multiple 1 mm thick slices with a 1 mm gap were acquired over the entire tumor region. A standard pulsed gradient spin echo sequence was used to acquire diffusion-weighted images with three *b* values (150, 500, and 800 s/mm^2) and gradients applied simultaneously along the three

orthogonal directions (x, y, and z). Scan acquisition parameters were: TR/TE = 2000/30 ms, gradient duration δ = 3 ms, gradient interval Δ = 20 ms, two signal excitations, and an acquisition matrix of 128 × 128 over a 28 × 28 mm^2 field of view. Image acquisition was triggered with respiration and navigator corrected (22) to reduce image artifacts due to bulk motion. Animals were allowed to recover from anesthesia and given free access to food and water between repeat imaging sessions. Repeat DW-MRI scan acquisitions were separated by a median of 5.88 hours (range: 1.5 – 7.8).

Image Analysis

To construct an ADC parametric map, signal intensities from images acquired at three b values were fit for each image voxel using a nonlinear least squares optimization method to Eq. (V-1):

$$S(b) = S_0 \cdot \exp(-\mathrm{ADC} \cdot b), \qquad \text{(V-1)}$$

where S_0 and $S(b)$ are the signal intensities before and after application of diffusion gradients, respectively. As we did not acquire images without application of diffusion gradients (i.e., b = 0), S_0 was a free parameter in our optimization routine. Both image volumes were viewed simultaneously to ensure that a similar tissue section was analyzed, and the b = 150 s/mm^2 image was utilized to define tumor boundaries. Care was taken during setup so that animal position and orientation in the magnet were similar between repeat acquisitions; however, image co-registration was not performed and thus separate regions of interest (ROIs) were drawn around the tumor for each scan. ROIs were also drawn within the skeletal muscle on the same slice as the tumor ROIs. Mean ADC values from each ROI were calculated and compared between repeated measurements. To

ensure data integrity, a water phantom was imaged simultaneously with the animal in each imaging session. If the mean ADC of the water phantom was outside the range of 2.65×10^{-3} $mm^2/s \pm 15\%$ (ADC value of free water at 32 ^{o}C; linearly interpolated from reference (23)), then the DW-MRI data from that animal was not used. All data analysis methods were performed in MATLAB® (The MathWorks, Natick, MA).

Reproducibility Statistics

Statistical methods for evaluating reproducibility follow Bland and Altman (24), and similar to what was previously implemented with imaging data by Galbraith et al. (25). For each data set, the difference between repeat measurements, *d*, was calculated. The distribution of the differences *d* was tested for normality using a two-sided Shapiro-Wilk test. A Kendall's tau test was used to estimate the correlation between the magnitude of the difference values and overall mean parameter value for the repeated measurements. Wilcoxon signed-rank test was performed with the original data to test the null hypothesis of no bias (i.e., average difference is zero) between repeated measurements. The statistical measurements of reproducibility were then calculated as follows:

1. The root-mean-square deviation (rMSD) is computed using the differences between repeat measurements *d*:

$$\text{rMSD} = \sqrt{\frac{\sum d^2}{\text{n}}} \qquad \text{(V-2)}$$

2. The 95% confidence interval (CI) for change which might occur in a group of *n* subjects:

$$\mathrm{CI} = \pm \frac{1.96 \cdot \mathrm{std}(d)}{\sqrt{\mathrm{n}}}, \tag{V-3}$$

where std(*d*) is the standard deviation of the difference between repeated measurements. Any change in a group of *n* greater than this value would be significant at the 5% level.

3. The within-subject standard deviation (wSD) is:

$$\mathrm{wSD} = \frac{\mathrm{rMSD}}{\sqrt{2}}. \tag{V-4}$$

4. The repeatability coefficient (r) is:

$$\mathrm{r} = 2.77 \cdot \mathrm{wSD}, \tag{V-5}$$

or, equivalently:

$$\mathrm{r} = 1.96 \cdot \mathrm{rMSD}. \tag{V-6}$$

The repeatability coefficient defines the magnitude of the maximum difference expected in 95% of paired observations; i.e., an observed difference greater than this value between scans in an individual would indicate a significant difference at the 5% level.

Due to our moderate sample sizes, we replaced 1.96 in Eq. (V-3) with the appropriate t-statistic for our sample size, which for 12 data sets is 2.2. Statistical analyses were performed using the statistical toolbox in MATLAB. A significance value of $p < 0.05$ was used for all statistical tests.

In addition to the above reproducibility statistics, we also quantified the intraclass correlation coefficient (ICC). An ICC greater than 0.61 was considered substantial agreement between repeated measurements (26).

Results

ADC from the water phantom for all repeated data sets was within the accepted range of free water diffusion at 32 °C (i.e., 2.65×10^{-3} mm^2/s ± 15%). The average ADC for scan 1 was 2.59×10^{-3} mm^2/s (range: 2.25×10^{-3} mm^2/s to 2.94×10^{-3} mm^2/s), and the average ADC for scan 2 was 2.53×10^{-3} mm^2/s (range: 2.28×10^{-3} mm^2/s to 2.82×10^{-3} mm^2/s). Examples of ADC parametric maps from repeated scans are depicted in Figure V-1, annotated with labels for tumor ('T'), muscle ('M'), and water phantom ('W'). It can be noted from the figure that the animal orientation is slightly different between repeated scans, thus demonstrating the need for separate ROIs for each imaging session.

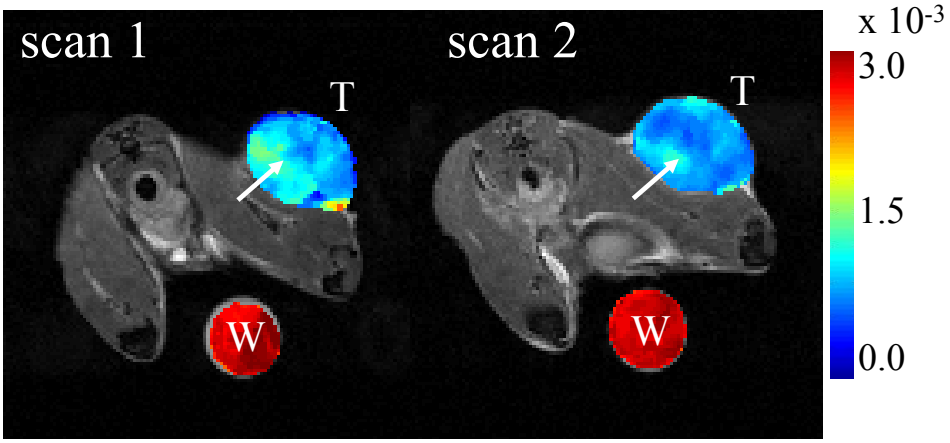

Figure V-1. Test-retest examples of ADC parametric maps. Three regions of interest are indicated: tumor (denoted with a 'T'), skeletal muscle (denoted with 'M'), and a water phantom (denoted with a 'W'). Take note of how the animal orientation is slightly different between repeat scans, which might affect ADC reproducibility as the same tissue sections from each scan might not be analyzed. This variation in positioning is somewhat noticeable in the tumor, as the location and size of higher ADC regions (white arrows) are different. Units of ADC are in mm^2/s.

The reproducibility statistics for the tumor and muscle ROIs are listed in Table V-1. Neither ROI had an average difference significantly different from normal as determined from the Wilcoxon signed-rank test. Additionally, the difference between repeat measurements *d* was independent of the mean for both tumor and muscle ROIs (thus, a logarithmic (or other) transformation was not required).

Table V-1. ADC (mm^2/s) reproducibility analysis for both tumor and muscle ROIs

ROI	Mean ($x10^{-3}$)	Mean difference ($x10^{-3}$)	95% CI for mean difference ($x10^{-3}$)	wSD ($x10^{-3}$)	Repeatability ($x10^{-3}$)	ICC
tumor	0.811	0.030	± 0.099 (11%)	0.099	0.273	0.79
muscle	1.14	-0.008	± 0.097 (8.5%)	0.104	0.288	0.64

ADC, apparent diffusion coefficient; ROI, region of interest; CI, confidence interval; wSD, within-subject standard deviation; ICC, intraclass correlation coefficient

Figure V-2 displays Bland-Altman plots for both ROIs, with each panel plotting the differences in ADC values between the repeated scans against the mean ADC. The mean difference and 95% CIs are displayed as solid and dotted lines, respectively. The 95% CIs define the required change to surpass the expected measurement variability for a group of mice, which are ± 0.090 × 10^{-3} mm^2/s (± 11.1%) and ± 0.097 × 10^{-3} mm^2/s (± 8.5%) for mean tumor and muscle ADC, respectively. Repeatability ranges (dashed lines) provide thresholds of significance for individuals, and are ± 0.273 × 10^{-3} mm^2/s and ± 0.288 × 10^{-3} mm^2/s for mean tumor and muscle ADC, respectively.

We calculated the ICC for each ROI (see Table V-1). The ICC for each of the ROIs was greater than 0.61, and thus there was substantial agreement between repeated measurements (26).

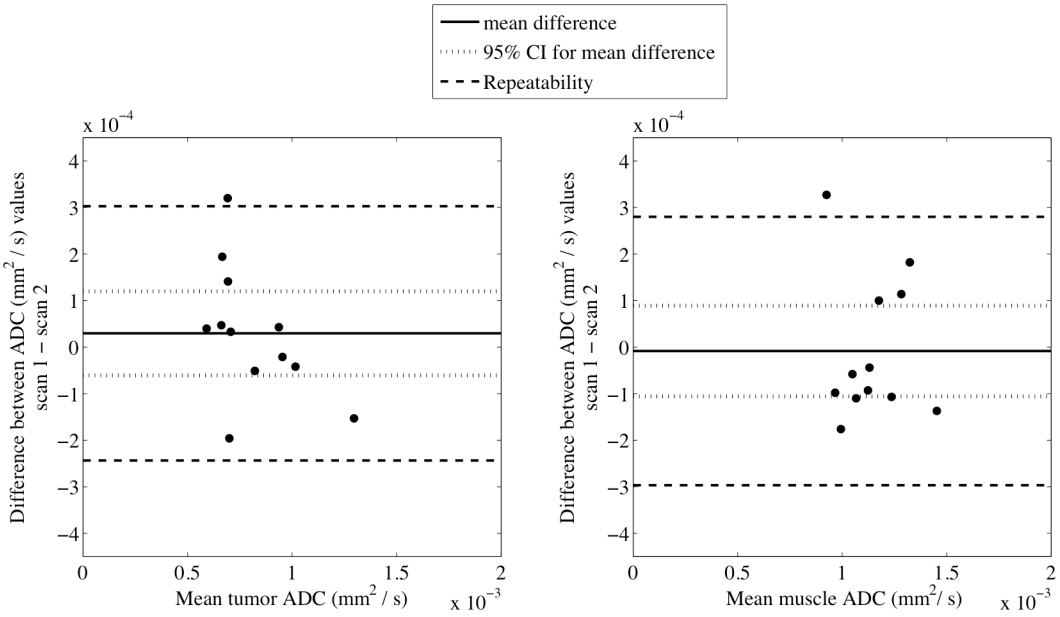

Figure V-2. Bland-Altman plots displaying the difference in ADC between scans plotted against mean ADC for both tumor (left panel) and muscle (right panel) ROIs. The mean difference (solid line) is shown with 95% confidence intervals (dotted lines), which defines the significance threshold for the population. Repeatability is also shown (dashed lines), and represents the threshold required to guarantee a statistically significant change in an individual mouse.

Discussion

We chose to quantify reproducibility for individuals and groups in a manner similar to Galbraith et al. (24), which is based on the limits of agreement methods described by Bland and Altman (24). This analysis provides objective statistical thresholds that define the range of repeatability by quantifying the maximum difference expected to be observed between two repeat observations for an individual. Additionally, the 95% CI for the mean difference provides a measure of spontaneous change that is expected in groups of similar size to our cohort. Both the 95% CI and repeatability coefficient are useful in, for example, a longitudinal treatment response study where the objective is to quantify changes in parameters after a specific therapeutic intervention.

For example, mean tumor ADC would need to increase or decrease by 0.090×10^{-3} mm^2/s to reflect a treatment-induced change in a group analysis, or change by $\pm 0.273 \times 10^{-3}$ mm^2/s for an individual animal. The 95% CI when expressed as a percentage of the mean is ± 11.1%; this is a tolerable variability as treatment-induced changes greater than ± 20% have been reported when evaluating DW-MRI as a biomarker of response in several preclinical mouse models of cancer (12,27), including a mouse model of HER2+ human breast cancer (9). The reproducibility for muscle ADC was also expressed as a 95% CI and repeatability coefficient, which were $\pm 0.097 \times 10^{-3}$ mm^2/s and $\pm 0.288 \times 10^{-3}$ mm^2/s, respectively. The 95% CI expressed as a percentage of the mean is ± 8.5%, and thus changes greater than this value would reflect treatment-induced change rather than measurement error in muscle for cohort of mice.

Reproducibility in terms of agreement between repeat measurements (defined by the ICC) was worse for muscle (ICC = 0.64) compared to tumor (ICC = 0.79). This result is not surprising, considering that muscle ADC values in this study are calculated from a diffusion-weighted pulse sequence that encodes along a single diffusion direction, instead of the trace, for each *b* value. Since diffusion in muscle tissue is anisotropic (28-30), ADC values measured along only one direction, acquired by applying diffusion gradients simultaneously on all three axes, would be dependent on animal orientation in the scanner. Although the orientation was kept as consistent as possible, one might expect that slight differences between repeated scans would have a greater impact on reproducibility in muscle compared to tumor, as water diffusion in most tumor models is nearly isotropic (16).

The ICC for tumor and muscle from our study were slightly lower than a previous reproducibility study by O'Flynn et al. who observed an ICC of 0.91 for mean ADC of normal human breast tissue at 3T (20). It is worth noting that, while we observed lower ICCs than O'Flynn et al., our main objective was to quantify a threshold by which changes greater than that value would represent therapeutic interventions. The 95% CI and repeatability coefficient define these thresholds in a population or an individual, respectively, and thus are more appropriate than the ICC when interpreting results from a longitudinal treatment response study (19,31).

Although we attempted to be as consistent as possible between repeated acquisitions, this study is not without limitations. The most prominent issue is that we are not comparing the exact sections of tissue from each scan. We chose to remove the animal from the scanner between repeat acquisitions to more closely mimic a study in which an animal is scanned multiple times over multiple days, thereby allowing us to quantify the variability that we might expect during a treatment study. Additionally, allowing the animal to recover between repeat scans eliminated any physiological stress that may occur during long periods (~ 2.5 hours) of anesthesia. Removing the animal and allowing for recovery would mean that there might be slight differences in ROIs (both tumor and muscle), and thus possible repositioning errors between acquisitions. We expect that errors associated with differences in animal position would negatively impact reproducibility, thus resulting in larger 95% CIs and repeatability coefficients.

Conclusion

The development of imaging biomarkers with the sensitivity to detect treatment-induced changes in tumor physiology before tumor volume change is an active area of interest. Before an imaging biomarker can be reliably employed in a treatment response study, the reproducibility must be assessed. In this study, we assessed reproducibility of DW-MRI data in conjunction with an ADC measurement. The test-retest analysis of mean tumor ADC measurements was very reproducible (95% CI = ± 11.1%), and thus DW-MRI can be used in serial studies to measure treatment-induced changes of tumor physiology in our mouse model of HER2+ human breast cancer.

References

1. Wahl RL, Jacene H, Kasamon Y, Lodge MA. From RECIST to PERCIST: Evolving Considerations for PET response criteria in solid tumors. J Nucl Med 2009;50 Suppl 1:122S-150S.
2. Guarneri V, Barbieri E, Dieci MV, Piacentini F, Conte P. Anti-HER2 neoadjuvant and adjuvant therapies in HER2 positive breast cancer. Cancer Treat Rev 2010;36 Suppl 3:S62-66.
3. Jackson JR, Patrick DR, Dar MM, Huang PS. Targeted anti-mitotic therapies: can we improve on tubulin agents? Nat Rev Cancer 2007;7(2):107-117.
4. Galons JP, Altbach MI, Paine-Murrieta GD, Taylor CW, Gillies RJ. Early increases in breast tumor xenograft water mobility in response to paclitaxel therapy detected by non-invasive diffusion magnetic resonance imaging. Neoplasia 1999;1(2):113-117.
5. Jensen LR, Garzon B, Heldahl MG, Bathen TF, Lundgren S, Gribbestad IS. Diffusion-weighted and dynamic contrast-enhanced MRI in evaluation of early treatment effects during neoadjuvant chemotherapy in breast cancer patients. J Magn Reson Imaging 2011;34(5):1099-1109.
6. Jordan BF, Runquist M, Raghunand N, Baker A, Williams R, Kirkpatrick L, Powis G, Gillies RJ. Dynamic contrast-enhanced and diffusion MRI show rapid and dramatic changes in tumor microenvironment in response to inhibition of HIF-1alpha using PX-478. Neoplasia 2005;7(5):475-485.
7. Karroum O, Mignion L, Kengen J, Karmani L, Leveque P, Danhier P, Magat J, Bol A, Labar D, Gregoire V, Bouzin C, Feron O, Gallez B, Jordan BF. Multimodal imaging of tumor response to sorafenib combined with radiation therapy: comparison between diffusion-weighted MRI, choline spectroscopy and (18) F-FLT PET imaging. Contrast Media Mol Imaging 2013;8(3):274-280.
8. Anderson AW, Xie J, Pizzonia J, Bronen RA, Spencer DD, Gore JC. Effects of cell volume fraction changes on apparent diffusion in human cells. Magn Reson Imaging 2000;18(6):689-695.
9. Aliu SO, Wilmes LJ, Moasser MM, Hann BC, Li KL, Wang D, Hylton NM. MRI methods for evaluating the effects of tyrosine kinase inhibitor administration used to enhance chemotherapy efficiency in a breast tumor xenograft model. J Magn Reson Imaging 2009;29(5):1071-1079.
10. Larocque MP, Syme A, Allalunis-Turner J, Fallone BG. ADC response to radiation therapy correlates with induced changes in radiosensitivity. Med Phys 2010;37(7):3855-3861.
11. Lee SC, Poptani H, Pickup S, Jenkins WT, Kim S, Koch CJ, Delikatny EJ, Glickson JD. Early detection of radiation therapy response in non-Hodgkin's lymphoma xenografts by in vivo 1H magnetic resonance spectroscopy and imaging. NMR Biomed 2010;23(6):624-632.
12. Loveless ME, Lawson D, Collins M, Nadella MV, Reimer C, Huszar D, Halliday J, Waterton JC, Gore JC, Yankeelov TE. Comparisons of the efficacy of a Jak1/2 inhibitor (AZD1480) with a VEGF signaling inhibitor (cediranib) and sham treatments in mouse tumors using DCE-MRI, DW-MRI, and histology. Neoplasia 2012;14(1):54-64.

13. Thoeny HC, Ross BD. Predicting and monitoring cancer treatment response with diffusion-weighted MRI. J Magn Reson Imaging 2010;32(1):2-16.
14. Galban CJ, Chenevert TL, Meyer CR, Tsien C, Lawrence TS, Hamstra DA, Junck L, Sundgren PC, Johnson TD, Galban S, Sebolt-Leopold JS, Rehemtulla A, Ross BD. Prospective analysis of parametric response map-derived MRI biomarkers: identification of early and distinct glioma response patterns not predicted by standard radiographic assessment. Clin Cancer Res 2011;17(14):4751-4760.
15. Sun YS, Zhang XP, Tang L, Ji JF, Gu J, Cai Y, Zhang XY. Locally advanced rectal carcinoma treated with preoperative chemotherapy and radiation therapy: preliminary analysis of diffusion-weighted MR imaging for early detection of tumor histopathologic downstaging. Radiology 2010;254(1):170-178.
16. Padhani AR, Liu G, Koh DM, Chenevert TL, Thoeny HC, Takahara T, Dzik-Jurasz A, Ross BD, Van Cauteren M, Collins D, Hammoud DA, Rustin GJ, Taouli B, Choyke PL. Diffusion-weighted magnetic resonance imaging as a cancer biomarker: consensus and recommendations. Neoplasia 2009;11(2):102-125.
17. Gibbs P, Pickles MD, Turnbull LW. Repeatability of echo-planar-based diffusion measurements of the human prostate at 3 T. Magn Reson Imaging 2007;25(10):1423-1429.
18. Kim SY, Lee SS, Park B, Kim N, Kim JK, Park SH, Byun JH, Song KJ, Koo JH, Choi EK, Lee MG. Reproducibility of measurement of apparent diffusion coefficients of malignant hepatic tumors: effect of DWI techniques and calculation methods. J Magn Reson Imaging 2012;36(5):1131-1138.
19. Koh DM, Blackledge M, Collins DJ, Padhani AR, Wallace T, Wilton B, Taylor NJ, Stirling JJ, Sinha R, Walicke P, Leach MO, Judson I, Nathan P. Reproducibility and changes in the apparent diffusion coefficients of solid tumours treated with combretastatin A4 phosphate and bevacizumab in a two-centre phase I clinical trial. Eur Radiol 2009;19(11):2728-2738.
20. O'Flynn EA, Morgan VA, Giles SL, deSouza NM. Diffusion weighted imaging of the normal breast: reproducibility of apparent diffusion coefficient measurements and variation with menstrual cycle and menopausal status. Eur Radiol 2012;22(7):1512-1518.
21. Ritter CA, Perez-Torres M, Rinehart C, Guix M, Dugger T, Engelman JA, Arteaga CL. Human breast cancer cells selected for resistance to trastuzumab in vivo overexpress epidermal growth factor receptor and ErbB ligands and remain dependent on the ErbB receptor network. Clin Cancer Res 2007;13(16):4909-4919.
22. Anderson AW, Gore JC. Analysis and correction of motion artifacts in diffusion weighted imaging. Magn Reson Med 1994;32(3):379-387.
23. Mills R. Self-Diffusion in Normal and Heavy Water in the Range of 1-45 degrees. The Journal of Physical Chemistry 1973;77(5).
24. Bland JM, Altman DG. Measuring agreement in method comparison studies. Stat Methods Med Res 1999;8(2):135-160.
25. Galbraith SM, Lodge MA, Taylor NJ, Rustin GJ, Bentzen S, Stirling JJ, Padhani AR. Reproducibility of dynamic contrast-enhanced MRI in human muscle and

tumours: comparison of quantitative and semi-quantitative analysis. NMR Biomed 2002;15(2):132-142.
26. Landis JR, Koch GG. The measurement of observer agreement for categorical data. Biometrics 1977;33(1):159-174.
27. Suh JY, Cho G, Song Y, Lee CK, Kang JS, Kang MR, Park SB, Kim YR, Kim JK. Is apparent diffusion coefficient reliable and accurate for monitoring effects of antiangiogenic treatment in a longitudinal study? J Magn Reson Imaging 2012;35(6):1430-1436.
28. Westin CF, Maier SE, Mamata H, Nabavi A, Jolesz FA, Kikinis R. Processing and visualization for diffusion tensor MRI. Med Image Anal 2002;6(2):93-108.
29. Galban CJ, Maderwald S, Uffmann K, de Greiff A, Ladd ME. Diffusive sensitivity to muscle architecture: a magnetic resonance diffusion tensor imaging study of the human calf. Eur J Appl Physiol 2004;93(3):253-262.
30. Williams SE, Heemskerk AM, Welch EB, Li K, Damon BM, Park JH. Quantitative effects of inclusion of fat on muscle diffusion tensor MRI measurements. J Magn Reson Imaging 2013.
31. Galbraith SM, Rustin GJ, Lodge MA, Taylor NJ, Stirling JJ, Jameson M, Thompson P, Hough D, Gumbrell L, Padhani AR. Effects of 5,6-dimethylxanthenone-4-acetic acid on human tumor microcirculation assessed by dynamic contrast-enhanced magnetic resonance imaging. J Clin Oncol 2002;20(18):3826-3840.

CHAPTER VI

OPTIMIZATION OF IMAGING TIME POINTS FOR LONGITUDINAL TREATMENT RESPONSE STUDIES

Introduction

The current radiographic assessment of tumor response is based on the Response Evaluation Criteria in Solid Tumors (RECIST), which relies on characterizing one-dimensional changes in tumor size during the course of therapy (1). Results from these criteria can be misleading as tumor response is based on linear changes along one-dimension, whereas tumors are most certainly changing in all three spatial dimensions. Additionally, this measurement is based on morphological changes that are almost certainly temporally delayed behind molecular, cellular, and physiological changes (2). Thus, imaging techniques with the sensitivity to quantify early changes in molecular characteristics of cancer would potentially offer earlier and more specific assessments of treatment response.

The primary objective of Specific Aim 2 is to define a set of imaging techniques that are most sensitive to assessing early treatment response of HER2+ breast cancer xenografts exposed to trastuzumab. More specifically, we aim to determine the imaging methods that differentiate responders from nonresponders before tumor size changes are evident. In this chapter, we describe the experiments used to select the optimal imaging time points during therapy, with the objective of determining when a significant difference in tumor volume is first observed.

Materials and Methods

Tumor Xenograft Model

BT474 cells (gifted from Dr. Carlos Arteaga, M.D. at Vanderbilt University) were cultured in improved minimal essential medium (IMEM, Invitrogen, Carlsbad, CA) supplemented with 10% fetal bovine serum at 37°C in a humidified, 5% CO_2 incubator. Cells were harvested with trypsin at approximately 85% confluence. Female athymic mice (n = 8, 4-6 weeks of age, Harlan, Indianapolis, IN) were implanted with 0.72 mg, 60-day release, 17β-estradiol pellets (Innovative Research of America, Sarasota, FL). One day later, approximately 10^7 BT474 cells suspended in a 1:10 ratio of growth factor-reduced Matrigel and IMEM were injected subcutaneously into the right flank. Mice were anesthetized with 2% isoflurane in pure oxygen for both procedures. Tumor volumes were measured weekly *via* calipers, and longitudinal imaging and treatment regiment commenced when tumor volumes reached approximately 200 mm^3 (typically 4-8 weeks after cell injection). Vanderbilt University's Animal Care and Use Committee approved all animal procedures.

Image Acquisition and Analysis

All tumor-bearing mice were separated into treated and control cohorts, and imaged across multiple days after baseline (see Figure VI-1): day 1, day 2, day 4, day 5, day 7, and day 8. Mice were treated immediately following imaging at baseline and days 3 and 6 with either trastuzumab (10 mg/kg) or saline vehicle *via* an i.p. injection (total volume, 100 mL). Trastuzumab was purchased from the Vanderbilt University Hospital Pharmacy (Nashville, TN).

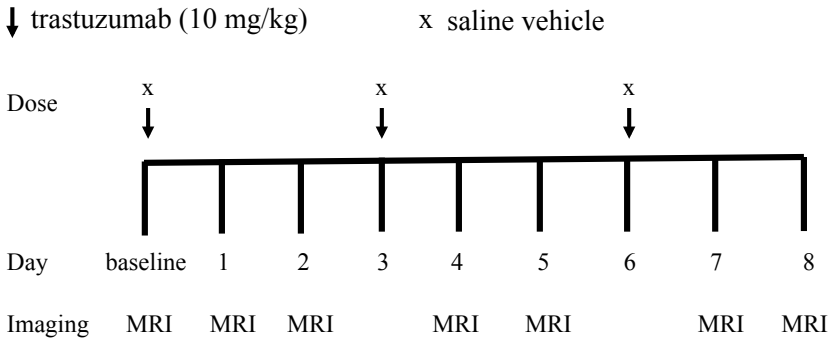

Figure VI-1. Longitudinal imaging and trastuzumab treatment study schema. Tumor volume measurements were quantified from T_2-weighted images acquired at baseline and days 1, 2, 4, 5, 7, and 8. Mice were randomized equally into two groups: trastuzumab (n = 4) and vehicle (n = 4) treated cohorts. Mice were treated with either trastuzumab (10 mg/kg) or saline vehicle by i.p. (total volume, 100 mL).

Tumor volumes were measured from high-resolution, T_2-weighted, magnetic resonance images (MRI) collected at each time point using a 7T MRI scanner (Agilent Technologies (formally Varian), Palo Alto, CA) equipped with a 38 mm quadrature RF coil (Doty Scientific, Columbia, SC). Anesthesia was induced and maintained for each imaging session *via* 2% isoflurane in pure oxygen. Animal respiration rate was monitored, and animal body temperature was maintained at an external temperature of 32^{o} C by means of a flow of warm air directly into the bore of the magnet. Each animal was placed in a custom built restraint, and the tumor region was first localized *via* 3D gradient echo scout images. T_2-weighted images covering the entire tumor volume were acquired using a fast spin-echo pulse sequence with the following parameters: TR = 5500 ms, effective TE = 35.6 ms, 1 mm slice thickness, and an acquisition matrix of 128 × 128 over a 28 × 28 mm^2 field of view yielding a voxel size of 0.22 × 0.22 mm^2.

MRI data were imported into MATLAB® version R2010B (The MathWorks, Natick, MA), and tumor volumes at each time point were measured by manually drawing

regions of interest (ROIs) along tumor boundaries from all slices consisting of tumor tissue. I delineated all tumor ROIs to ensure consistency. Tumor volumes at each time point were compared between and within each mouse cohort using a two-tailed Student's t-test. A significance value of $p < 0.05$ was used for all comparisons.

Results

Figure VI-2 displays a representative example of a T_2-weighted image with tumor boundaries highlighted in red. Note that the image contrast between tumor and muscle tissue is sufficient such that the peripheries of the tumor can be easily identified for accurate tumor segmentation and ROI definition.

Figure VI-2. Representative example of a T_2-weighted magnetic resonance image displayed with tumor boundaries highlighted in red. Note the sufficient contrast between tumor and muscle for accurate delineation of tumor boundaries.

Average tumor volume (± standard error, SE) is displayed in Figure VI-3 for the trastuzumab and vehicle treated cohorts. Statistically significant differences in tumor volume between cohorts are denoted with asterisks (*).

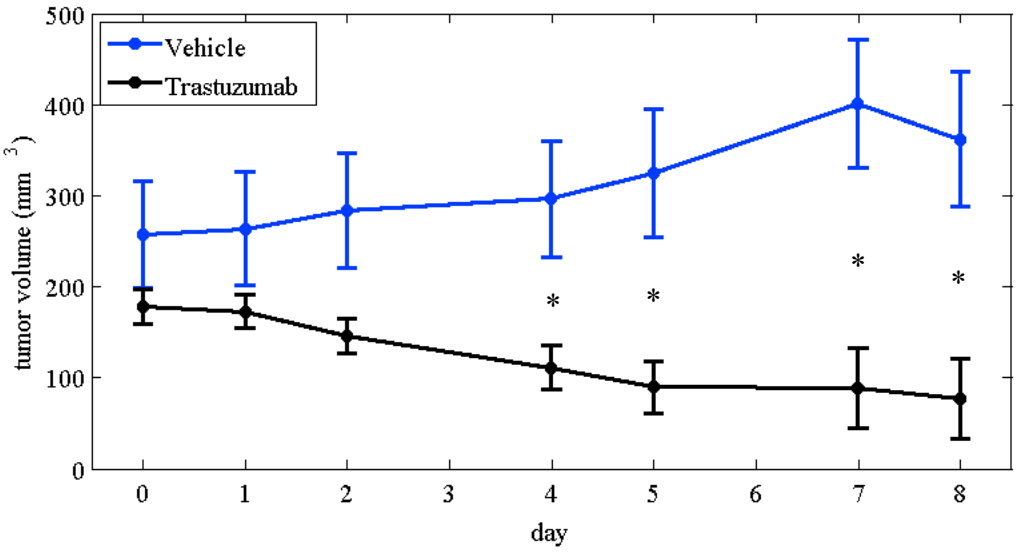

Figure VI-3. Average tumor volume displayed at each imaging time point for each mouse cohort. Longitudinal tumor volumes were measured from T_2-weighted MR images. * $p < 0.05$, significant difference in tumor volume between cohorts.

The *p* values from each statistical comparison (i.e., within each group and between groups) at each time point are listed in Table VI-1. Values representing significance are highlighted in red font. Significant differences in tumor volume were observed at day 2 within each cohort compared to baseline. However, tumor volumes between mouse cohorts were not statistically different until day 4.

Table VI-1. Comparison results for within and between each group and time point

Mouse Cohort	Baseline	Day 1	Day 2	Day 4	Day 5	Day 7	Day 8
Vehicle	n/a	0.41	**0.01**	**0.008**	**0.01**	**0.009**	**0.007**
Trastuzumab	n/a	0.47	**0.04**	**0.02**	**0.02**	0.09	0.08
Between cohorts	0.25	0.21	0.08	**0.03**	**0.02**	**0.02**	**0.03**

Discussion

The objective of this experiment was to determine the earliest time point after therapy where differences in tumor volume measurements were not observed. A

statistically significant difference in tumor volume between the BT474 treated and control group was first observed at 24 hours after the second round of treatment (day 4). Both of the within group comparisons resulted in a significant difference in tumor volume at day 2 when compared to baseline. Difference in tumor volume when compared within or between cohorts was not observed at day 1. Thus, the optimal imaging time points for the longitudinal treatment response studies were determined to be baseline before any treatment, and 24 hours post a first (day 1) and second (day 4) treatment.

Conclusion

Specific Aims 2 and 3 (Chapters VII-IX) investigate the utility of several PET and MRI techniques for assessing response early during the course of treatment with HER2+ human breast cancer xenografts exposed to trastuzumab. Since these treatment response studies were our first experiences with these tumor models, it was imperative to investigate the pattern of tumor growth with and without treatment. This study allowed for the determination of an early time point after treatment where differences in tumor volume were not yet significant. We hypothesize that functional and molecular imaging techniques will report treatment-induced vascular, cellular, and molecular changes at or before this early time point, and thus be predictors of therapeutic response. This hypothesis is systematically tested in the following chapters.

References

1. Wahl RL, Jacene H, Kasamon Y, Lodge MA. From RECIST to PERCIST: Evolving Considerations for PET response criteria in solid tumors. J Nucl Med 2009;50 Suppl 1:122S-150S.
2. Harry VN, Semple SI, Parkin DE, Gilbert FJ. Use of new imaging techniques to predict tumour response to therapy. Lancet Oncol 2010;11(1):92-102.

CHAPTER VII

UTILITY OF ^{18}F-FLT PET TO ASSESS TREATMENT RESPONSE IN A MURINE MODEL OF HER2+ BREAST CANCER

Introduction

The human epidermal growth factor receptor 2 (HER2) is overexpressed in 20% to 25% of diagnosed breast cancers (1,2), and positively correlates with a more aggressive disease phenotype and poor prognosis (2). Consequently, specific anti-HER2 therapeutics have been developed that bind to HER2 and disrupt downstream signaling pathways (3). Trastuzumab (Herceptin®, Genentech, San Francisco, CA) was the first HER2-targeted therapy (4,5), and has been shown to inhibit cell cycle progression, cell proliferation, and survival (6,7). It is estimated, however, that only 25% to 30% of patients with HER2-overexpressing tumors will respond to single-agent trastuzumab and others will develop resistance (8), emphasizing the need for accurate and reliable assessments of treatment response early during the course of therapy.

The standard-of-care radiographic assessment of response uses the response evaluation criteria in solid tumors (RECIST, (9)), which quantifies treatment response based on one-dimensional changes in tumor morphology. As current and emerging anticancer therapies are designed to induce molecular changes that potentially occur substantially sooner than changes in tumor size (10), RECIST may not be the most sensitive or accurate approach (11). Thus, noninvasive imaging techniques that can report on cellular and physiological processes are of interest. Positron emission tomography

(PET) with 3'-deoxy-3'-^{18}F-fluorothymidine (^{18}F-FLT) is an emerging molecular imaging technique that, in certain situations, provides a noninvasive estimate of cellular proliferation as tracer uptake is regulated by the expression and activity of thymidine kinase 1 (TK1), which is an important enzyme in the cell-cycle dependent thymidine salvage pathway of DNA synthesis (12). ^{18}F-FLT PET might provide more insight than RECIST into the assessment of disease response, as one of the hallmarks of malignant tumors is increased proliferative activity (13). Indeed, ^{18}F-FLT PET has been shown to be useful for evaluating treatment efficacy with molecular targeted therapies in preclinical mouse models (14-16), as well as assessing response early during the course of therapy in patients (17,18). However, a recent study provided evidence suggesting that ^{18}F-FLT PET might not always reflect the proliferative index of certain tumors (19); thus, emphasizing the need for the systematic evaluation of ^{18}F-FLT PET to assess response in a variety of cancer types and treatment regimens.

Based on the observations that trastuzumab reduces HER2-mediated cell proliferation, we explored the utility of ^{18}F-FLT PET to assess response early during the course of therapy (i.e., before significant changes in tumor size occurred) in HER2+ mouse models that are sensitive and resistant to trastuzumab. We also explored the sensitivity of ^{18}F-FLT PET to differentiate trastuzumab resistance between sensitive and resistant HER2+ xenografts after exposure to trastuzumab. Thus, the objective of this study was to determine if ^{18}F-FLT PET could separate mouse cohorts early during the course of treatment. In an attempt to validate the imaging findings, we also investigated the relationship between the imaging data and the underlying biology.

Materials and Methods

Cell Culture

Trastuzumab responsive (BT474) and resistant (HR6) cells were gifts from Dr. Carlos Arteaga, M.D. at Vanderbilt University. HR6 cells were harvested from BT474 xenografts as described previously (6). Briefly, female athymic mice with BT474 xenografts were treated twice per week with 20 mg/kg trastuzumab diluted in sterile saline. Tumors that initially responded completely and then recurred in the presence of maintained trastuzumab treatment were harvested, minced, and digested to generate the HR6 cell line (6). Both cell lines were cultured in improved minimal essential medium (IMEM, Invitrogen, Carlsbad, CA) supplemented with 10% fetal bovine serum at 37°C in a humidified, 5% CO_2 incubator. To maintain trastuzumab resistance, HR6 cells were also cultured with 10 mg/ml trastuzumab as previously described (6). Trastuzumab was purchased from the Vanderbilt University Hospital Pharmacy (Nashville, TN). For cell innoculation, cells were harvested with trypsin at approximately 85% confluence.

Tumor Xenograft Model

Our Institution's Animal Care and Use Committee approved all animal procedures. Female athymic nude mice (n = 25, 4-6 weeks old, Harlan, Indianapolis, IN) were implanted with 0.72 mg, 60-day release, 17β-estradiol pellets (Innovative Research of America, Sarasota, FL). Twenty-four hours later, approximately 10^7 BT474 or HR6 cells, suspended in a 1:10 ratio of growth factor-reduced Matrigel and IMEM, were injected subcutaneously into the right flank. Tumor volumes were measured once per week *via* calipers, and experiments commenced once tumor volumes reached > 200 mm^3

(typically 4 to 8 weeks post cell innoculation). A 26-gauge jugular catheter was surgically implanted for radiotracer delivery. Mice were anesthetized with 2% isoflurane in pure oxygen mixture for all surgical procedures.

Trastuzumab Treatment Study

Mice bearing tumors were grouped into four cohorts: trastuzumab and vehicle treated BT474 cohorts, and trastuzumab and vehicle treated HR6 cohorts. The number of mice for each cohort and imaging time point is displayed in Table VII-1.

Table VII-1. Tabulated list of animal number for each cohort and time point

Time point	BT474 treated	BT474 control	HR6 treated	HR6 control
Baseline	8	5	8	6
Day 1	8	5	8	6
Day 4	6	4	7	6

For treatment, mice were administered twice in four days with trastuzumab (10 mg/kg) or saline vehicle by i.p. (total volume, 100 mL). ^{18}F-FLT PET was conducted at baseline and days 1 and 4, which were 24 hours post first and second treatments, respectively. Figure VII-1 illustrates the imaging and dosing schedule for the treatment response study.

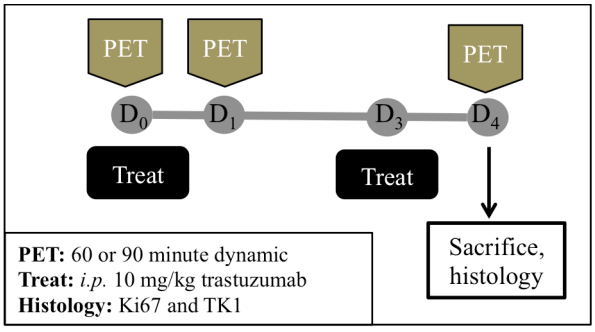

Figure VII-1. Longitudinal imaging and trastuzumab treatment study schema. Mice were treated twice in four days with either trastuzumab (10 mg/kg) or saline vehicle. Dynamic ^{18}F-FLT PET data were acquired at baseline and 24 hours post the first and second treatment.

Radiotracer Synthesis

^{18}F-FLT was prepared as a service by the radiochemistry core using a two-step, one pot reaction as described previously (20). ^{18}F-FLT was obtained with average radiochemical purity of 98.3% and specific activity ≥ 345.5 TBq/mmol.

Volumetric Imaging and Analysis

Longitudinal tumor volume was measured from T_2-weighted magnetic resonance images (as previously described in Chapter VI). Anesthesia was induced and maintained *via* 2% isoflurane in pure oxygen. Animal respiration rate was monitored, and animal body temperature was maintained at an external temperature of 32^{o} C by means of a flow of warm air directly into the bore of the magnet. Each animal was placed in a custom built restraint, and the tumor region was first localized *via* 3D gradient echo scout images. T_2-weighted images covering the entire tumor volume were acquired using a fast spin-echo pulse sequence with the following parameters: TR = 5500 ms, effective TE = 35.6 ms, 1 mm slice thickness, and an acquisition matrix of 128 × 128 over a 28 × 28 mm^2 field of view yielding a voxel size of 0.22 × 0.22 mm^2. Data were imported into MATLAB® version R2010b (The MathWorks, Natick, MA), and tumor volumes were measured at each time point by manually drawing regions of interest (ROIs) along tumor boundaries from all slices consisting of tumor tissue. I delineated all tumor ROIs to ensure consistency.

^{18}F-FLT PET Imaging

After volumetric imaging, mice were transferred under anesthesia to a dedicated small-animal microPET Focus 200 system (Concorde Microsystems Inc, Knoxville, TN (21)) where animal body temperature was then maintained by a heated water pad and heat lamp. Anesthesia was continued, and list-mode data were collected for 60 (n = 2) or 90 (n = 23) minutes before, during, and after injection of 7.3 ± 2.0 MBq (mean ± standard error, SE) of ^{18}F-FLT diluted in 100 μL of sterile saline. Images collected for 90 minutes were reconstructed into a 46-frame dynamic sequence (12 × 5 s, 6 × 10 s, 4 × 40 s, 4 × 60 s, 5 × 120 s, 4 × 180s, and 12 × 300 s) using a three-dimensional ordered-subsets expectation maximization (OSEM3D) algorithm followed by a maximum *a posteriori* (MAP) algorithm (22). OSEM3D-MAP reconstruction was performed using two OSEM3D iterations with nine subsets, followed by 18 MAP iterations with a beta value 0.038 (22). Images collected for 60 minutes were reconstructed similarly but with a 64-frame dynamic sequence (5 × 12 s, 59 × 60 s). The resulting 3D reconstruction has a voxel size of 0.475 mm × 0.475 mm × 0.796 mm. Attenuation and scatter correction were not performed as the amount of attenuation in microPET studies of mice is small compared to human studies and differences between animals are not expected to be significant (21).

Quantification of Tracer Uptake

MATLAB was used to manually draw 3D ROIs around the tumor volumes from the PET images. ROIs were also drawn across three slices within the contralateral muscle. The average activity from the last 30 minutes of each dynamic acquisition was

normalized for animal weight and injected dose to generate parametric maps of the standardized uptake value (SUV). For longitudinal comparison, the maximum SUV normalized to lean muscle (SUL_{max}) was quantified for each tumor ROI.

Immunohistochemistry

Immediately following imaging, animals were sacrificed and excised tumors were fixed in 10% formalin for at least 24 hours. Samples were then transferred to 70% ethanol and stored in 4 °C. Samples were blocked in paraffin, and 4-micron sections were prepared for immunostaining with Ki67 (M7240; Dako, Carpinteria, CA) and TK1 (ab57757; Abcam, Cambridge, MA). Stained sections were imaged at 20× magnification using a Leica SCN400 Slice Scanner (Leica, Buffalo Grove, IL). Unbiased and automated image analysis was performed using algorithms that were trained based on shape and intensity of the stain. The index for each marker was expressed as the ratio of the number of percent positive cells to total cell number counted from four random fields per tumor section. Tumor sections from 4 (BT474 and HR6 vehicle treated groups) or 6 (BT474 and HR6 trastuzumab treated groups) mice from each cohort were analyzed for comparison with *in vivo* data.

Statistics

Three statistical comparisons were performed in this study: 1) trastuzumab versus vehicle treated BT474 cohorts, 2) trastuzumab versus vehicle treated HR6 cohorts, and 3) responders (BT474 treated) versus nonresponders (HR6 treated). Longitudinal ^{18}F-FLT PET parameters were compared within and between cohorts at each imaging time point.

Ki67 and TK1 percent positive were compared between cohorts. All data are presented as mean ± SE. Additionally, all statistical comparisons were evaluated using the nonparametric Wilcoxon rank sum test in MATLAB version 2010b, and data were considered significant if $p < 0.05$.

Results

Impact of Trastuzumab on Tumor Xenograft Growth

Longitudinal tumor volumes from the trastuzumab and vehicle treated BT474 cohorts are displayed in Figure VII-2A. In the vehicle treated group, tumor size increased slightly over four days but the increase was not statistically significant (day 1: $p = 0.42$; day 4: $p = 0.11$). Trastuzumab treatment inhibited tumor growth in the trastuzumab treated group; the decrease was not statistically significant at day 1 ($p = 0.44$), yet trended towards significance at day 4 ($p = 0.05$). No difference in tumor volume between the trastuzumab and vehicle treated BT474 mice was observed at day 1 ($p = 0.28$), but a statistically significant difference was observed at day 4 ($p = 0.02$), indicating that the BT474 xenograft model is responsive to trastuzumab.

Longitudinal tumor volumes for the trastuzumab and vehicle treated HR6 cohorts are displayed in Figure VII-2B. Tumor size steadily increased over four days in the vehicle treated group yet differences after treatment were not statistically different (day 1: $p = 0.39$; day 4: $p = 0.24$). Tumor size also increased in the trastuzumab treated group, although, similar to the vehicle cohort, differences were not significant at any time point after baseline (day 1: $p = 0.80$; day 4: $p = 0.96$). Tumor volume between groups was not

statistically different at any imaging time point (baseline: $p = 0.18$; day 1: $p = 0.14$; day 4: $p = 0.18$), indicating that the HR6 xenograft model is resistant to trastuzumab.

To evaluate the impact of trastuzumab on tumor xenografts with different trastuzumab sensitivities, longitudinal tumor volume from the responders (BT474 treated) and nonresponders (HR6 treated) are graphed for comparison in Figure VII-2C. No difference in tumor volume between responders and nonresponders was observed at day 1 ($p = 0.23$), but a statistically significant difference was observed at day 4 ($p = 0.04$).

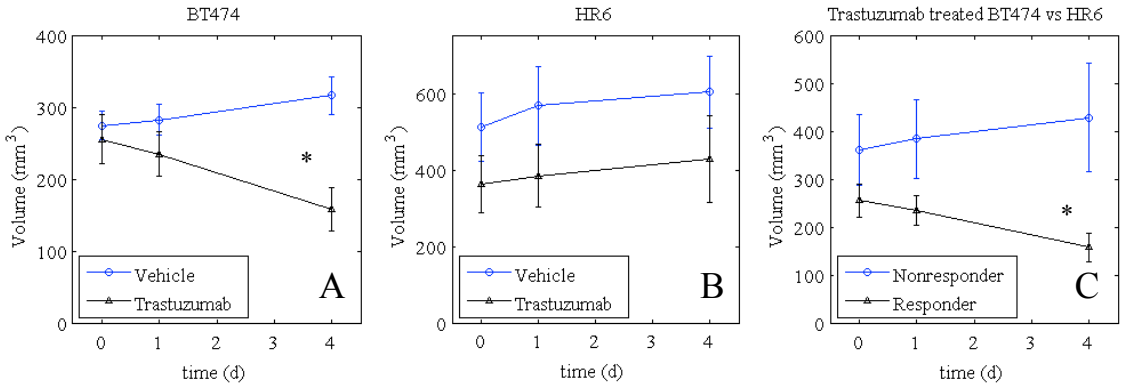

Figure VII-2. Impact of trastuzumab on tumor growth in the: (A) trastuzumab sensitive BT474, (B) trastuzumab resistant HR6, and (C) trastuzumab treated BT474 and HR6 xenografts. Tumor volume was measured from MR images. *$p < 0.05$

^{18}F-FLT PET Assesses Early Treatment Response in BT474 Xenografts

Changes in ^{18}F-FLT accumulation in response to trastuzumab are shown in Figure VII-3. At baseline, no statistical difference in SUL_{max} was observed between trastuzumab and vehicle treated groups ($p = 0.72$). In the vehicle treated group, a non-significant increase in SUL_{max} was observed at day 1 ($p = 0.55$, compared to baseline); the increase in SUL_{max} at day 4 trended towards significance ($p = 0.06$, compared to baseline). In contrast, SUL_{max} in the trastuzumab treated group decreased, although not significantly, at day 1 ($p = 0.10$, compared to baseline) and day 4 ($p = 0.75$, compared to baseline).

However, the difference in SUL_{max} between the trastuzumab and vehicle treated groups was statistically significant at day 1 ($p = 0.03$), and continued to be significantly different at day 4 ($p = 0.04$). The Ki67 immunohistochemistry results (Figure VII-3C) supported the imaging findings at day 4 as a significant difference ($p = 0.02$) in Ki67 score is observed between the trastuzumab and vehicle treated BT474 cohorts. The expected trend in TK1 immunohistochemistry results was observed (i.e., more TK1 staining observed in the vehicle treated group), however the difference between cohorts was not statistically significant ($p = 0.61$).

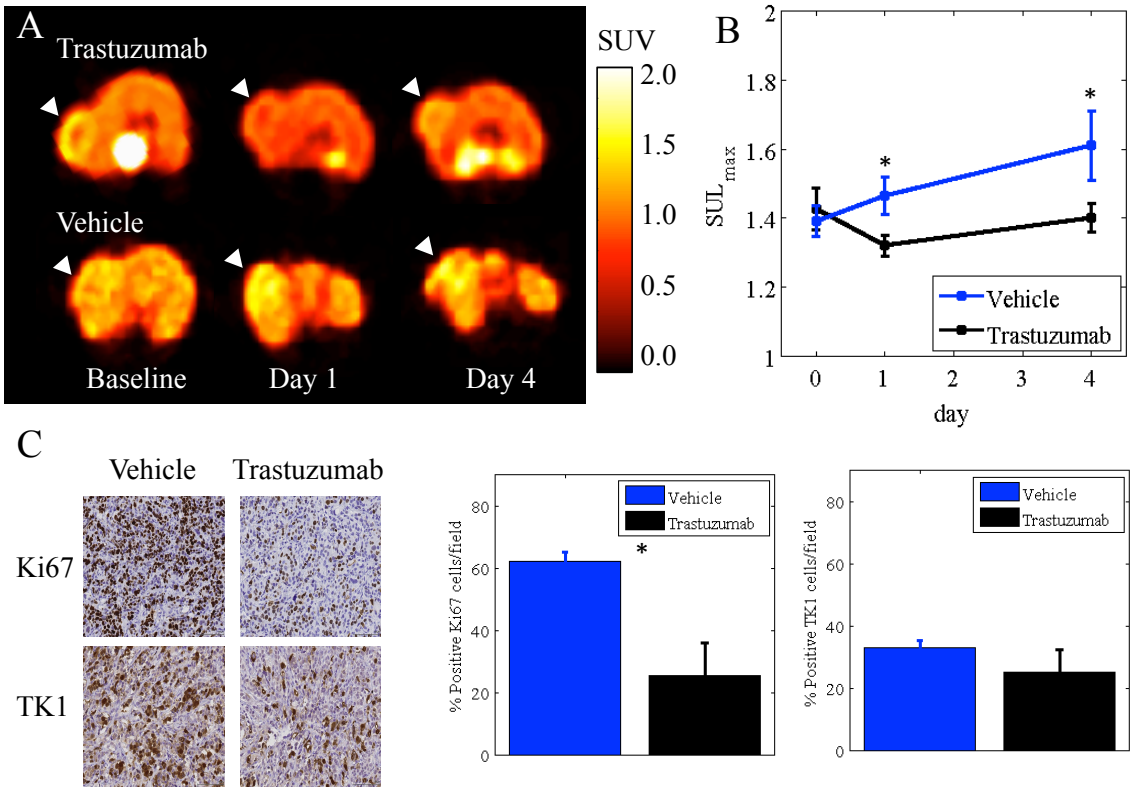

Figure VII-3. Early biological changes after trastuzumab treatment is observed with ^{18}F-FLT PET: parametric maps of the standardized uptake value (SUV) from a representative animal in the trastuzumab (*top row*) and vehicle (*bottom row*) treated cohorts (A), longitudinal changes in SUL_{max} (mean ± SE) of tumors in mice receiving either trastuzumab or vehicle (B), and significant difference Ki67 percent positive corresponds with *in vivo* imaging results (C). Expected trend in TK1 percent positive is observed, but differences between cohorts was not statistically significant (C). * $p < 0.05$

For reference, the maximum SUV from the tumor ROI, the mean SUV from the muscle ROI used to calculate SUL_{max}, and the SUL_{max} for each time point and animal in the trastuzumab and vehicle treated BT474 cohorts is tabulated in Supplemental Table VII-1 (located at the end of this chapter).

No Difference in ^{18}F-FLT PET Observed Between HR6 Xenografts

Longitudinal ^{18}F-FLT PET data are displayed in Figure VII-4 for the trastuzumab and vehicle treated HR6 cohorts. Statistical differences in SUL_{max} between the trastuzumab and vehicle treated HR6 groups were not observed any point during the study (baseline: $p = 0.28$; day 1: $p = 0.41$; day 4: $p = 0.84$). In the vehicle treated group, a non-significant decrease in SUL_{max} was observed at day 1 ($p = 0.18$, compared to baseline). A non-significant increase was observed at day 4 but to a SUL_{max} below that at baseline ($p = 0.59$, compared to baseline). In the trastuzumab treated group, a non-significant decrease in SUL_{max} was observed at day 1 ($p = 0.38$, compared to baseline) followed by a non-significant increase at day 4 ($p = 0.23$, compared to baseline).

Immunohistochemistry results (Figure VII-4C) supported the imaging findings at day 4 as the difference in Ki67 and TK1 scores were not statistically significant ($p = 0.11$, $p = 0.35$, respectively) between the trastuzumab and vehicle treated HR6 cohorts. Although the differences were insignificant, the percentages of Ki67 and TK1 positive cells were almost 50% higher in the trastuzumab-treated cohort, which was unexpected considering the *in vivo* PET data (Figure VII-4B). We hypothesize that the 50% increase in histological markers relating to cellular proliferation (e.g., Ki67 and TK1) is the effect of overcoming trastuzumab response. We return to this point in the Discussion.

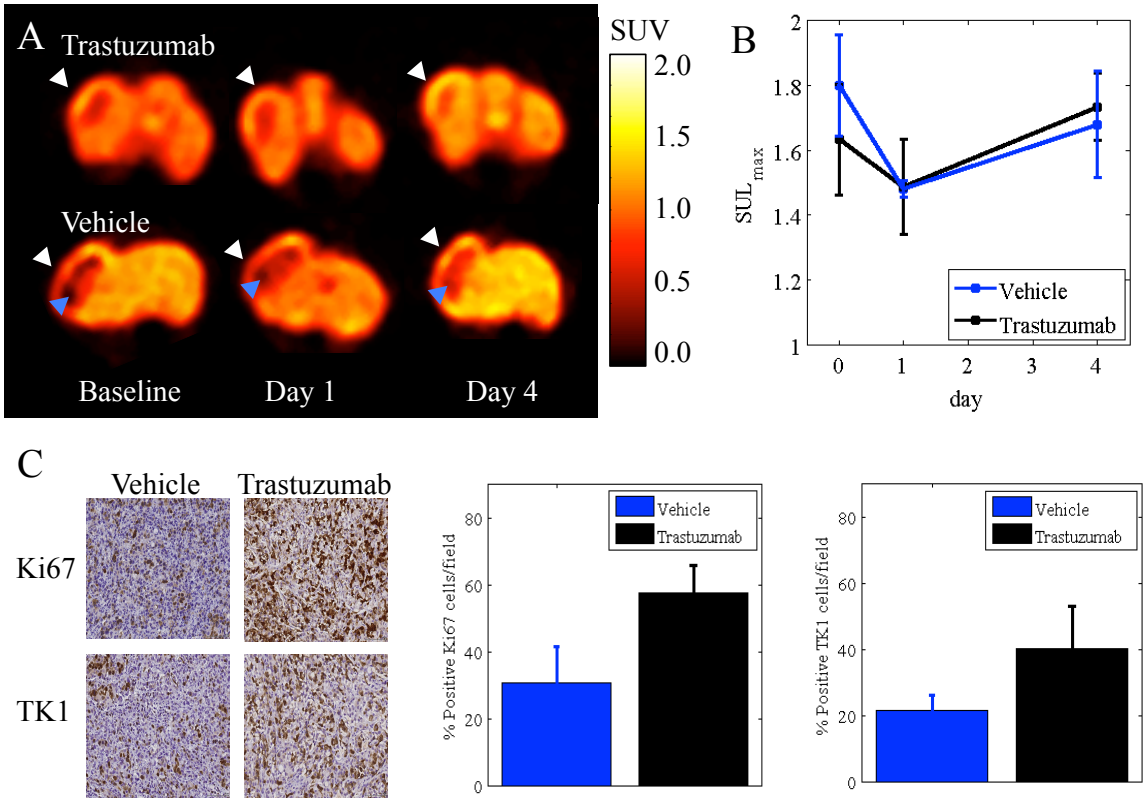

Figure VII-4. Statistically significant differences in ^{18}F-FLT retention were not observed between trastuzumab and vehicle treated trastuzumab resistant HR6 cohorts at any time point during the study: parametric maps of the standardized uptake value (SUV) from a representative animal in the trastuzumab (*top row*) and vehicle (*bottom row*) treated cohorts (A), longitudinal changes in SUL_{max} (mean ± SE) of tumors in mice receiving either trastuzumab or vehicle (B), and no significant differences with Ki67 or TK1 immunohistochemistry (C), which corresponds with the *in vivo* imaging data at day 4. White arrows point to the tumor, and a blue arrow points to an example of necrosis.

For reference, the maximum SUV from the tumor ROI, the mean SUV from the muscle ROI used to calculate SUL_{max}, and the SUL_{max} for each time point and animal in the trastuzumab and vehicle treated HR6 cohorts is tabulated in Supplemental Table VII-1 (located at the end of this chapter).

^{18}F-FLT PET Differentiates Responders from Nonresponders

Longitudinal ^{18}F-FLT PET data is graphed in Figure VII-5 for the trastuzumab treated BT474 and HR6 cohorts, i.e., the responders and nonresponders, respectively. Differences in SUL_{max} were not statistically different at baseline (p = 0.65) or day 1 (p = 0.57) between the responders and nonresponders. However, differences at day 4 were significant (p = 0.02), suggesting that ^{18}F-FLT PET can differentiate between tumors that are sensitive and resistant to trastuzumab. Ki67 immunohistochemistry results trended similarly to the imaging data, however the difference between the responder and nonresponder cohorts only trended towards significance (p = 0.06; Figure VII-5B). The TK1 immunohistochemistry results also trended similarly to the imaging data, however the difference was not statistically different between cohorts (p = 0.59; Figure VII-5C).

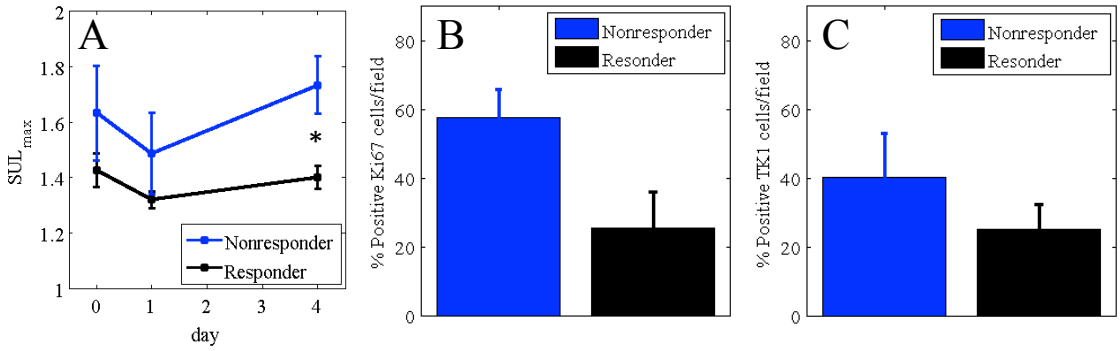

Figure VII-5. Statistically significant differences in SUL_{max} were observed between mice bearing tumors with varying trastuzumab sensitivities, suggesting that ^{18}F-FLT PET can detect responders from nonresponders (A). Ki67 score trended with the imaging data at Day 4, however the difference between cohorts only trended toward significance (B, p = 0.06). TK1 score also trended with the imaging data, however the difference was not statistically significant (C, p = 0.59) 7). * $p < 0.05$

Discussion

In contrast to the anatomical imaging methods (e.g., computed tomography and MRI) used to assess one-dimensional changes in tumor size, noninvasive molecular

imaging aims to provide *in vivo* assessments of specific molecular, cellular, and physiological characteristics of the tumor and the microenvironment. As emerging anticancer therapeutics are designed to induce molecular changes that potentially occur substantially sooner than changes in morphology, molecular imaging techniques offer earlier and potentially more sensitive therapeutic response assessments. Recently newer criteria, such as the PET Response Criteria in Solid Tumors (PERCIST), recognize the potential utility of PET to predict response earlier during the course of therapy (PERCIST (9)). ^{18}F-FLT PET is an emerging molecular imaging technique that has shown clinical utility in preclinical mouse models of cancer (14,15,23) and patients (17,24). However, limitations of ^{18}F-FLT as a biomarker of the proliferative index of tumors have been recently reported (19), emphasizing the need for a systematic evaluation of ^{18}F-FLT PET to assess response in a variety of cancer types and specific treatment regimens. Thus, the objective of this study was to evaluate the potential utility of ^{18}F-FLT PET to offer earlier response assessments in HER2+ mouse models of breast cancer treated with trastuzumab.

We demonstrated the utility of ^{18}F-FLT PET to assess early response to trastuzumab in the BT474 HER2+ human breast cancer model. We are not the first to report these observations in the BT474 exposed to trastuzumab. Shah et al. performed ^{18}F-FLT PET before and after 1 week of trastuzumab therapy, and observed a significant difference between trastuzumab and vehicle treated cohorts (25). Our study builds on the previous effort and suggests that ^{18}F-FLT PET can detect a significant change as early as 24 hours after one trastuzumab treatment. Shah et al. also evaluated the ability of the most clinically used PET tracer, 2-deoxy-2-^{18}F-fluoro-D-glucose (^{18}F-FDG), to quantify tumor metabolism changes in the BT474 model exposed to trastuzumab; however,

significant differences in ^{18}F-FDG uptake were not observed between trastuzumab and vehicle treated cohorts (25). The insensitivity of ^{18}F-FDG to differentiate response coupled with our findings suggest that biomarkers of proliferation (e.g., ^{18}F-FLT PET) might be better suited to predict response to therapies that alter cellular proliferation (e.g., trastuzumab).

We are, however, the first to present longitudinal ^{18}F-FLT PET data in a xenograft model that was engineered to exhibit trastuzumab resistance. We demonstrated that differences in ^{18}F-FLT retention were not observed between trastuzumab and vehicle treated mice with trastuzumab resistant xenografts although one cohort was receiving therapy that was intended to alter cellular proliferation. This result then allowed for the comparison between the so-called responders and nonresponders, or the trastuzumab treated BT474 and HR6 cohorts, respectively. We observed a significant difference in ^{18}F-FLT retention between cohorts suggesting that ^{18}F-FLT PET can differentiate nonresponders from responders. However, the detected change was significant at the same time as a significant difference in tumor volume (i.e., at day 4); thus, ^{18}F-FLT PET did not provide an early biomarker of treatment response in these cohorts.

The objective of the immunohistochemistry analyses was to provide potential validation of the *in vivo* data by investigating the relationship between the imaging parameter and the underlying biology. Both the Ki67 and TK1 scores for the BT474 cohorts corresponded with the imaging data (Figure VII-3C), although only the difference in Ki67 between the cohorts was statistically significant. Significant differences in Ki67 or TK1 scores were not observed between the trastuzumab and vehicle treated HR6 cohorts, which also corresponded with the imaging data (Figure VII-4C). The difference

in Ki67 score between the responders and nonresponders trended towards significance (Figure VII-5C $p = 0.06$). To investigate whether Ki67 score correlated with SUL_{max}, we calculated the Pearson correlation coefficient. Similarly to the comparison between Ki67 scores from the two cohorts, the correlation between the histological parameter and *in vivo* imaging parameter also only trended towards significance. These data suggest that the imaging-histology parameter comparison does not have the required power to observe a statistical significant difference. To test this hypothesis, we processed tumor sections from additional BT474 (n = 2) and HR6 (n = 2) xenografts with Ki67 immunohistochemistry. These mice were treated in the same manner (i.e., at baseline and day 3) as the mice included in the imaging study, the only difference being that ^{18}F-FLT PET data were not collected. The resulting difference in Ki67 score after including more animals is now significant ($p = 0.04$). The trend in TK1 score corresponded with the imaging data, yet difference between cohorts was neither significant nor trended towards significance (Figure VII-5C).

Study Limitations

We note that the average tumor volume of the treated trastuzumab resistant HR6 xenografts at baseline was larger (~30%) than the treated trastuzumab sensitive BT474 xenografts. Since the difference in tumor volume between these two groups was not significant, we were able to compare the effects of trastuzumab treatment with the *in vivo* PET and histology data. As the volume of xenografts increase, regions of necrosis develop due to a reduced delivery of nutrients to those tumor regions. (Examples of necrosis are highlighted with blue arrows in Figure VII-4A). Necrosis will increase the

heterogeneity of radiotracer uptake throughout the whole tumor volume. To eliminate the potential bias of tumor heterogeneity from the quantified ^{18}F-FLT PET data, we compared the maximum activity from the tumor ROI. We also noted longitudinal differences (> ±15%) in ^{18}F-FLT accumulation within the muscle tissue in a few mice suggesting possible differences in radiotracer specific activities and radioactivity yield. In order to compare data across multiple time points and mice, we normalized the maximum SUV from the tumor to the average SUV from the contralateral muscle.

Future Work

We noted in the Results section that although not significant, a 50% increase in both Ki67 and TK1 scores were observed in the trastuzumab treated HR6 cohort compared to the vehicle treated cohort. Our hypothesis for these observations is that the trastuzumab treated HR6 cohort is resistant to trastuzumab by increasing cellular processes, specifically those leading to cellular proliferation and survival. Ritter et al. postulate that the HR6 cell line escapes trastuzumab action through PI3K activation, which is a cell signaling pathway that leads to cellular proliferation and survival (6). In a subsequent report from the same group, Miller et al. demonstrate that inhibition of mTOR (a major downstream effector of the PI3K pathway) suppressed cell growth in the HR6 cells (26). Quantifying TK1 and other proteins relating to cellular proliferation (e.g., PS6, which is a marker for mTOR) from Western blot studies of HR6 cells with and without exposure to trastuzumab is a potential study that, if TK1 expression increased with increasing concentration of trastuzumab, would support our hypothesis. Future studies to

elucidate the potential relationship between TK1 expression and trastuzumab resistance are needed to support this hypothesis.

Robust and reproducible methods for analyzing kinetic ^{18}F-FLT PET data in order to provide quantitative evaluations of tumor proliferation have been previously investigated (27-29). The net tracer flux (previously described in Chapter III) is a quantity of interest in treatment response studies as it combines kinetic modeling parameters relating to delivery and retention of the radiotracer (30). Future work will be to evaluate the utility of ^{18}F-FLT PET dynamic parameters to assess early response to trastuzumab in both HER2+ models that are sensitive (i.e., BT474) and resistant (i.e., HR6) to trastuzumab.

Conclusion

^{18}F-FLT PET is an emerging molecular imaging technique that offers noninvasive measurements of cellular proliferation. However, mixed reviews of the utility of ^{18}F-FLT PET to assess early treatment response have been reported, thus emphasizing the need to systematically evaluate this technique in different cancer types and treatment regimens. Our data suggest that ^{18}F-FLT PET is sensitive to early molecular changes in the trastuzumab sensitive BT474 HER2+ breast cancer model, and can also differentiate mouse models of HER2+ breast cancer with varying trastuzumab sensitivities (i.e., BT474 versus HR6). The latter result potentially has significant clinical impact as the development of imaging methods that can separate responders from nonresponders earlier during the course of therapy is of great interest in order to reduce cost and negative systemic effects caused by ineffective therapies.

References

1. Spector NL, Blackwell KL. Understanding the mechanisms behind trastuzumab therapy for human epidermal growth factor receptor 2-positive breast cancer. J Clin Oncol 2009;27(34):5838-5847.
2. Dean-Colomb W, Esteva FJ. Her2-positive breast cancer: herceptin and beyond. Eur J Cancer 2008;44(18):2806-2812.
3. Ross JS, Fletcher JA. The HER-2/neu oncogene in breast cancer: prognostic factor, predictive factor, and target for therapy. Stem Cells 1998;16(6):413-428.
4. Nahta R, Esteva FJ. HER2 therapy: molecular mechanisms of trastuzumab resistance. Breast Cancer Res 2006;8(6):215.
5. Carter P, Presta L, Gorman CM, Ridgway JB, Henner D, Wong WL, Rowland AM, Kotts C, Carver ME, Shepard HM. Humanization of an anti-p185HER2 antibody for human cancer therapy. Proc Natl Acad Sci U S A 1992;89(10):4285-4289.
6. Ritter CA, Perez-Torres M, Rinehart C, Guix M, Dugger T, Engelman JA, Arteaga CL. Human breast cancer cells selected for resistance to trastuzumab in vivo overexpress epidermal growth factor receptor and ErbB ligands and remain dependent on the ErbB receptor network. Clin Cancer Res 2007;13(16):4909-4919.
7. Moulder SL, Yakes FM, Muthuswamy SK, Bianco R, Simpson JF, Arteaga CL. Epidermal growth factor receptor (HER1) tyrosine kinase inhibitor ZD1839 (Iressa) inhibits HER2/neu (erbB2)-overexpressing breast cancer cells in vitro and in vivo. Cancer Res 2001;61(24):8887-8895.
8. Schmitz KR, Ferguson KM. Interaction of antibodies with ErbB receptor extracellular regions. Exp Cell Res 2009;315(4):659-670.
9. Wahl RL, Jacene H, Kasamon Y, Lodge MA. From RECIST to PERCIST: Evolving Considerations for PET response criteria in solid tumors. J Nucl Med 2009;50 Suppl 1:122S-150S.
10. Guarneri V, Barbieri E, Dieci MV, Piacentini F, Conte P. Anti-HER2 neoadjuvant and adjuvant therapies in HER2 positive breast cancer. Cancer Treat Rev 2010;36 Suppl 3:S62-66.
11. Harry VN, Semple SI, Parkin DE, Gilbert FJ. Use of new imaging techniques to predict tumour response to therapy. Lancet Oncol 2010;11(1):92-102.
12. Dunphy MP, Lewis JS. Radiopharmaceuticals in preclinical and clinical development for monitoring of therapy with PET. J Nucl Med 2009;50 Suppl 1:106S-121S.
13. Hanahan D, Weinberg RA. Hallmarks of cancer: the next generation. Cell 2011;144(5):646-674.
14. McKinley ET, Smith RA, Zhao P, Fu A, Saleh SA, Uddin MI, Washington MK, Coffey RJ, Manning HC. 3'-Deoxy-3'-18F-fluorothymidine PET predicts response to (V600E)BRAF-targeted therapy in preclinical models of colorectal cancer. J Nucl Med 2013;54(3):424-430.
15. Mason NS, Lopresti BJ, Ruszkiewicz J, Dong X, Joyce S, Leef G, Sen M, Wahed AS, Mathis CA, Grandis JR, Thomas SM. Utility of 3'-[(18)F]fluoro-3'-deoxythymidine as a PET tracer to monitor response to gene therapy in a

xenograft model of head and neck carcinoma. Am J Nucl Med Mol Imaging 2013;3(1):16-31.
16. Aide N, Kinross K, Cullinane C, Roselt P, Waldeck K, Neels O, Dorow D, McArthur G, Hicks RJ. 18F-FLT PET as a surrogate marker of drug efficacy during mTOR inhibition by everolimus in a preclinical cisplatin-resistant ovarian tumor model. J Nucl Med 2010;51(10):1559-1564.
17. Hoeben BA, Troost EG, Span PN, van Herpen CM, Bussink J, Oyen WJ, Kaanders JH. 18F-FLT PET during radiotherapy or chemoradiotherapy in head and neck squamous cell carcinoma is an early predictor of outcome. J Nucl Med 2013;54(4):532-540.
18. Kahraman D, Holstein A, Scheffler M, Zander T, Nogova L, Lammertsma AA, Boellaard R, Neumaier B, Dietlein M, Wolf J, Kobe C. Tumor lesion glycolysis and tumor lesion proliferation for response prediction and prognostic differentiation in patients with advanced non-small cell lung cancer treated with erlotinib. Clin Nucl Med 2012;37(11):1058-1064.
19. McKinley ET, Ayers GD, Smith RA, Saleh SA, Zhao P, Washington MK, Coffey RJ, Manning HC. Limits of [(18)F]-FLT PET as a Biomarker of Proliferation in Oncology. PLoS One 2013;8(3):e58938.
20. Choi SJ, Kim JS, Kim JH, Oh SJ, Lee JG, Kim CJ, Ra YS, Yeo JS, Ryu JS, Moon DH. [18F]3'-deoxy-3'-fluorothymidine PET for the diagnosis and grading of brain tumors. Eur J Nucl Med Mol Imaging 2005;32(6):653-659.
21. Tai YC, Ruangma A, Rowland D, Siegel S, Newport DF, Chow PL, Laforest R. Performance evaluation of the microPET focus: a third-generation microPET scanner dedicated to animal imaging. J Nucl Med 2005;46(3):455-463.
22. Qi J, Leahy RM, Cherry SR, Chatziioannou A, Farquhar TH. High-resolution 3D Bayesian image reconstruction using the microPET small-animal scanner. Phys Med Biol 1998;43(4):1001-1013.
23. Cawthorne C, Burrows N, Gieling RG, Morrow CJ, Forster D, Gregory J, Radigois M, Smigova A, Babur M, Simpson K, Hodgkinson C, Brown G, McMahon A, Dive C, Hiscock D, Wilson I, Williams KJ. [18F]-FLT Positron Emission Tomography Can Be Used to Image the Response of Sensitive Tumors to PI3-Kinase Inhibition with the Novel Agent GDC-0941. Mol Cancer Ther 2013;12(5):819-828.
24. Idema AJ, Hoffmann AL, Boogaarts HD, Troost EG, Wesseling P, Heerschap A, van der Graaf WT, Grotenhuis JA, Oyen WJ. 3'-Deoxy-3'-18F-fluorothymidine PET-derived proliferative volume predicts overall survival in high-grade glioma patients. J Nucl Med 2012;53(12):1904-1910.
25. Shah C, Miller TW, Wyatt SK, McKinley ET, Olivares MG, Sanchez V, Nolting DD, Buck JR, Zhao P, Ansari MS, Baldwin RM, Gore JC, Schiff R, Arteaga CL, Manning HC. Imaging biomarkers predict response to anti-HER2 (ErbB2) therapy in preclinical models of breast cancer. Clin Cancer Res 2009;15(14):4712-4721.
26. Miller TW, Forbes JT, Shah C, Wyatt SK, Manning HC, Olivares MG, Sanchez V, Dugger TC, de Matos Granja N, Narasanna A, Cook RS, Kennedy JP, Lindsley CW, Arteaga CL. Inhibition of mammalian target of rapamycin is required for optimal antitumor effect of HER2 inhibitors against HER2-overexpressing cancer cells. Clin Cancer Res 2009;15(23):7266-7276.

27. Muzi M, Vesselle H, Grierson JR, Mankoff DA, Schmidt RA, Peterson L, Wells JM, Krohn KA. Kinetic analysis of 3'-deoxy-3'-fluorothymidine PET studies: validation studies in patients with lung cancer. J Nucl Med 2005;46(2):274-282.
28. Whisenant JG, Peterson TE, Fluckiger JU, Tantawy MN, Ayers GD, Yankeelov TE. Reproducibility of static and dynamic (18)F-FDG, (18)F-FLT, and (18)F-FMISO MicroPET studies in a murine model of HER2+ breast cancer. Mol Imaging Biol 2013;15(1):87-96.
29. Bradbury MS, Hambardzumyan D, Zanzonico PB, Schwartz J, Cai S, Burnazi EM, Longo V, Larson SM, Holland EC. Dynamic small-animal PET imaging of tumor proliferation with 3'-deoxy-3'-18F-fluorothymidine in a genetically engineered mouse model of high-grade gliomas. J Nucl Med 2008;49(3):422-429.
30. Lee SJ, Kang HY, Kim SY, Chung JH, Oh SJ, Ryu JS, Kim SB, Kang JS, Park SK, Kim HM, Kim MH, Moon DH. Early assessment of tumor response to JAC106, an anti-tubulin agent, by 3'-deoxy-3'-[(1)(8)F]fluorothymidine in preclinical tumor models. Eur J Nucl Med Mol Imaging 2011;38(8):1436-1448.

Supplementary Table VII-1

Tabulated SUV values for tumor and muscle ROIs, as well as, the tumor SUL_{max} for each trastuzumab and vehicle treated BT474 and HR6 cohort and imaging time point

Trastuzumab treated BT474 mice

	SUV tumor			SUV muscle			SUL_{max}		
Mouse	**Baseline**	**Day 1**	**Day 4**	**Baseline**	**Day 1**	**Day 4**	**Baseline**	**Day 1**	**Day 4**
1	1.14	1.19	1.29	0.91	0.97	0.97	1.25	1.22	1.33
2	1.35	1.30	1.21	0.98	0.91	0.88	1.37	1.43	1.38
3	1.92	1.83	1.91	1.34	1.31	1.24	1.43	1.39	1.53
4	1.53	1.46	1.21	1.05	1.11	0.80	1.45	1.31	1.53
5	1.99	1.64	1.34	1.13	1.28	1.02	1.76	1.28	1.32
6	1.73	1.18	1.36	1.07	0.99	1.03	1.62	1.20	1.32
7	1.82	1.65	NaN	1.24	1.25	NaN	1.46	1.32	NaN
8	1.44	1.61	NaN	1.18	1.15	NaN	1.22	1.41	NaN
average	**1.61**	**1.48**	**1.39**	**1.11**	**1.12**	**0.99**	**1.45**	**1.32**	**1.40**
SE	**0.11**	**0.08**	**0.11**	**0.05**	**0.05**	**0.06**	**0.06**	**0.03**	**0.04**

Vehicle treated BT474 mice

	SUV tumor			SUV muscle			SUL_{max}		
Mouse	**Baseline**	**Day 1**	**Day 4**	**Baseline**	**Day 1**	**Day 4**	**Baseline**	**Day 1**	**Day 4**
1	1.67	1.79	1.76	1.26	1.25	1.25	1.32	1.43	1.41
2	2.12	1.75	1.85	1.45	1.24	1.20	1.46	1.42	1.54
3	0.91	1.41	1.98	0.69	0.94	1.23	1.31	1.51	1.61
4	2.23	2.09	2.35	1.45	1.27	1.24	1.53	1.64	1.89
5	1.54	1.68	NaN	1.16	1.27	NaN	1.33	1.32	NaN
average	**1.69**	**1.75**	**1.98**	**1.20**	**1.19**	**1.23**	**1.39**	**1.47**	**1.61**
SE	**0.24**	**0.11**	**0.13**	**0.14**	**0.06**	**0.01**	**0.04**	**0.05**	**0.10**

Trastuzumab treated HR6 mice

	SUV tumor			SUV muscle			SUL_{max}		
Mouse	**Baseline**	**Day 1**	**Day 4**	**Baseline**	**Day 1**	**Day 4**	**Baseline**	**Day 1**	**Day 4**
1	1.86	1.89	2.15	1.32	1.33	1.17	1.41	1.42	1.84
2	1.22	1.51	1.01	0.86	1.14	0.57	1.42	1.32	1.78
3	1.43	1.28	1.92	1.09	1.21	1.40	1.31	1.05	1.37
4	1.85	1.68	0.86	1.22	1.13	0.47	1.52	1.49	1.85
5	1.31	1.34	1.60	0.99	1.10	1.14	1.33	1.21	1.41
6	2.82	2.37	1.78	1.01	1.00	1.04	2.78	2.38	1.72
7	1.99	1.84	1.84	1.17	1.04	0.84	1.70	1.77	2.18
8	1.65	1.56	NaN	1.03	1.25	NaN	1.59	1.25	NaN
average	**1.77**	**1.68**	**1.60**	**1.09**	**1.15**	**0.95**	**1.63**	**1.49**	**1.73**
SE	**0.18**	**0.12**	**0.18**	**0.05**	**0.04**	**0.13**	**0.17**	**0.15**	**0.10**

Vehicle treated HR6 mice

	SUV tumor			SUV muscle			SUL_{max}		
Mouse	**Baseline**	**Day 1**	**Day 4**	**Baseline**	**Day 1**	**Day 4**	**Baseline**	**Day 1**	**Day 4**
1	1.69	1.53	1.90	1.23	1.04	1.26	1.37	1.47	1.50
2	2.43	1.36	2.01	1.05	0.91	0.85	2.33	1.49	2.35
3	1.84	1.86	2.59	1.11	1.23	1.30	1.66	1.51	1.99
4	2.62	1.69	1.92	1.20	1.18	1.30	2.19	1.43	1.47
5	1.68	1.53	1.40	0.95	1.09	0.98	1.77	1.40	1.43
6	1.62	1.89	1.42	1.09	1.20	1.07	1.48	1.58	1.33
average	**1.98**	**1.64**	**1.87**	**1.10**	**1.11**	**1.13**	**1.80**	**1.48**	**1.68**
SE	**0.18**	**0.08**	**0.18**	**0.04**	**0.05**	**0.08**	**0.16**	**0.03**	**0.16**

CHAPTER VIII

ASSESSING TREATMENT RESPONSE IN HER2+ MURINE MODELS OF BREAST CANCER WITH DYNAMIC CONTRAST ENHANCED MRI

Introduction

The human epidermal growth factor receptor 2 (HER2) is overexpressed in approximately 25% of all breast cancers (1,2); HER2 overexpression is usually represented by a more aggressive disease phenotype and poor prognosis (2). Consequently, specific anti-HER2 therapeutics have been developed that bind to HER2 and disrupt downstream signaling pathways (3). Trastuzumab (Herceptin®, Genentech, San Francisco, CA) is one such therapy that was specifically developed to target HER2. The exact mechanisms of action of trastuzumab are unknown (4), however studies have shown that trastuzumab inhibits cell signaling pathways leading to an inhibition of cellular proliferation and survival. Trastuzumab has also been observed to alter tumor microvasculature by downregulating specific growth factors of angiogenesis leading to reduced vascular volume and blood flow (5,6). (A more detailed description of these mechanisms is provided in Chapter II).

A number of imaging techniques that report on specific characteristics of tumor vasculature have been developed; including, but not limited to, contrast enhanced ultrasound (7,8), contrast-enhanced computed tomography (9), and dynamic contrast enhanced magnetic resonance imaging (10). The latter technique is one of current interest, and efforts to improve the quality of information derived from dynamic contrast

enhanced magnetic resonance imaging (DCE-MRI) in the context of assessing treatment response are ongoing. Fundamentally, DCE-MRI is an imaging technique that characterizes the pharmacokinetics of an injected contrast agent (CA) as it washes in and out of a specific tissue. By acquiring serial T_1-weighted images over time, the kinetics of the CA can be quantified using (for example) a two-compartment model to estimate physiological characteristics relating to tumor microvasculature such as blood flow, vessel permeability, and tissue volume fractions. These quantitative measurements have been used to assess treatment response in a variety of cancer models and treatment regimens (11-13). More recently, the clinical utility of DCE-MRI to predict nonresponders from responders earlier in the course of therapy has been reported (14,15).

Although the use of DCE-MRI has been investigated in preclinical and clinical settings, the clinical translation of quantitative DCE-MRI into routine clinical care of cancer has been limited. This can be attributed to the inadequate understanding of whether DCE-MRI protocols can predict therapeutic efficacy and the lack of validation to assist in the interpretation of the imaging data (16,17). Thus, the objectives of this study were to determine if DCE-MRI can assess early treatment response (i.e., before changes in tumor size occur) in HER2+ mouse models that are sensitive to trastuzumab. We also explored the sensitivity of DCE-MRI to differentiate trastuzumab resistance between sensitive and resistant HER2+ xenografts exposed to trastuzumab. Additionally, in an attempt to validate the imaging findings, we investigated the relationship between the imaging data and the underlying biology.

Materials and Methods

Cell Culture

Trastuzumab responsive (BT474) and resistant (HR6) cells were gifts from Dr. Carlos Arteaga, M.D. at Vanderbilt University. HR6 cells were harvested from BT474 xenografts as described previously (18). Briefly, female athymic mice with BT474 xenografts were treated twice per week with 20 mg/kg trastuzumab diluted in sterile saline. Tumors that initially responded completely and then recurred in the presence of maintained trastuzumab treatment were harvested, minced, and digested to generate the HR6 cell line (18). Both cell lines were cultured in improved minimal essential medium (IMEM, Invitrogen, Carlsbad, CA) supplemented with 10% fetal bovine serum at 37 °C in a humidified, 5% CO_2 incubator. To maintain trastuzumab resistance, HR6 cells were also cultured with 10 mg/ml trastuzumab as previously described (18). Trastuzumab was purchased from the Vanderbilt University Hospital Pharmacy (Nashville, TN). Cells were harvested with trypsin at approximately 85% confluence for implantation.

Tumor Xenograft Model

Our Institution's Animal Care and Use Committee approved all animal procedures. Female athymic nude mice (n = 25, 4-6 weeks old, Harlan, Indianapolis, IN) were implanted with 0.72 mg, 60-day release, 17β-estradiol pellets (Innovative Research of America, Sarasota, FL). Twenty-four hours later, approximately 10^7 BT474 or HR6 cells, suspended in a 1:10 ratio of growth factor-reduced Matrigel and IMEM, were injected subcutaneously into the right flank. Tumor volumes were measured once per week *via* calipers, and experiments commenced once tumor volumes reached > 200 mm^3

(typically 4 to 8 weeks post cell injection). A 26-gauge jugular catheter was surgically implanted for radiotracer delivery. Mice were anesthetized with 2% isoflurane in pure oxygen mixture for all surgical procedures.

Trastuzumab Treatment Study

Mice bearing tumors were grouped into four cohorts: trastuzumab and vehicle treated BT474 cohorts, and trastuzumab and vehicle treated HR6 cohorts. The number of mice for each cohort and time point is displayed in Table VIII-1. For treatment, mice

Table VIII-1. Tabulated list of animal number for each cohort and time point

Time point	BT474 treated	BT474 control	HR6 treated	HR6 control
Baseline	7	5	5	8
Day 1	7	5	5	8
Day 4	4	4	5	6

were administered twice in four days with trastuzumab (10 mg/kg) or saline vehicle by i.p. (total volume, 100 mL). DCE-MRI was conducted at baseline and days 1 and 4, which were 24 hours post first and second treatments, respectively. Figure VIII-1 illustrates the imaging and dosing schedule for the trastuzumab treatment study.

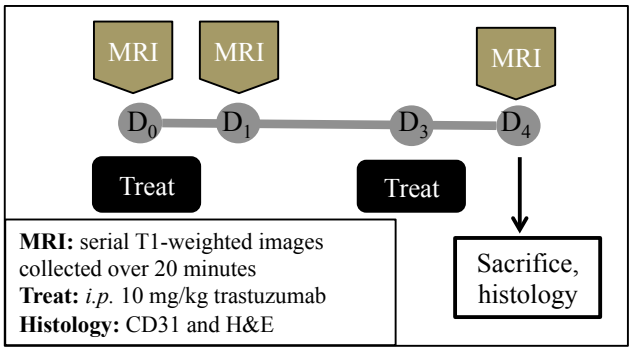

Figure VIII-1. Longitudinal imaging and trastuzumab treatment study schema. Mice were treated twice in four days with either trastuzumab (10 mg/kg) or saline vehicle. DCE-MRI data were acquired at baseline and 24 hours post the first and second treatments.

Volumetric Imaging and Analysis

All MRI data were collected using a 7T MRI scanner (Agilent Technologies (formally Varian), Palo Alto, CA) equipped with a 38 mm quadrature RF coil (Doty Scientific, Columbia, SC). Anesthesia was induced and maintained *via* 2% isoflurane in pure oxygen. Animal respiration rate was monitored, and animal body temperature was maintained at an external temperature of 32 ^{o}C by means of a flow of warm air directly into the bore of the magnet. Each animal was placed in a custom built restraint, and the tumor region was first localized *via* 3D gradient echo scout images. Longitudinal tumor volume was measured from T_2-weighted images; T_2-weighted images covering the entire tumor volume were acquired using a fast spin-echo pulse sequence with the following parameters: TR = 5500 ms, effective TE = 35.6 ms, 1 mm slice thickness, and an acquisition matrix of 128 × 128 over a 28 × 28 mm^2 field of view yielding a voxel size of 0.22 × 0.22 mm^2. Data were imported into MATLAB® version R2010b (The MathWorks, Natick, MA), and tumor volumes were measured at each time point by manually drawing regions of interest (ROIs) along tumor boundaries from all slices consisting of tumor tissue. I delineated all tumor ROIs to ensure consistency.

DCE-MRI Data Acquisition

The DCE-MRI protocol included acquisition of a pre-contrast T_1 map, as well as, serial T_1-weighted images. Data for the pre-contrast T_1 map were obtained by employing an inversion recovery fast low angle shot gradient echo sequence with an adiabatic inversion pulse with seven inversion times (TI): 15, 27, 49.8, 90, 162, 300, 600 seconds. The imaging parameters were as follows: TR/TE/a = 12,000 ms/2.1 ms/15°, NEX = 2,

acquisition matrix of 64 × 64, and a 28 × 28 mm^2 FOV yielding a voxel size of 0.44 × 0.44 mm^2. Fifteen 1 mm thick slices were acquired to cover the entire tumor volume. Dynamic T_1-weighted images were acquired using a spoiled gradient echo sequence at a temporal resolution of 12.8 seconds for ~20 minutes with the following parameters: TR/TE/α = 100 ms/2.1 ms/25°, NEX = 2, and the same acquisition matrix and FOV as the pre-contrast T_1 map. A bolus of Gd-DTPA at a concentration of 0.05 mmol/kg was delivered *via* a jugular catheter using an automated syringe pump (Harvard Apparatus, Holliston, MA) at a rate of 2.4 mL/min. Eleven baseline images (~ 2 minutes) were acquired before Gd-DTPA was administered.

DCE-MRI Data Analysis

Data collected for the pre-contrast T_1 map were imported into MATLAB, and then fit for every image voxel using a nonlinear least squares method to the following equation (also described in Chapter III):

$$S = S_0 \cdot \left| (1 - 2 \cdot e^{-TI/T_1} + e^{-TR/T_1}) \right|, \qquad \text{(VIII-1)}$$

where TR is the repetition time, and S_0 and S are the signal intensities at thermal equilibrium and inversion time, respectively.

Once T_1 maps were calculated, signal intensity time courses from all tumor voxels were analyzed to extract quantitative parameters relating to tumor blood flow, vessel permeability, and tissue volume fractions. Each signal intensity time course was then fit to a two-compartment model to extract pharmacokinetic parameters (19,20). If a homogeneous distribution of the contrast agent is assumed in both compartments, then

the time rate of change of the contrast agent concentration in the tissue, can be described as a linear, first-order ordinary differential equation:

$$\frac{dC_t(t)}{dt} = K^{trans} \cdot C_p(t) + \frac{K^{trans}}{v_e} C_t(t), \qquad \text{(VIII-2)}$$

where C_t and C_p are the concentrations of the contrast agent in the tissue and plasma compartment, respectively, K^{trans} is the volume transfer constant between C_p and C_t, and v_e is the extravascular extracellular volume fraction. The solution to this equation is:

$$C_t(t) = K^{trans} \int_0^t C_p(u) \cdot e^{-(K^{trans}/v_e)(t-u)} du. \qquad \text{(VIII-3)}$$

The measured signal intensity time courses from each voxel were fit to Eq. (VIII-3) using a nonlinear least squares algorithm to extract estimates of K^{trans} and v_e. The efflux constant that describes the transfer of contrast between C_p and C_t, $k_{ep} (\equiv K^{trans} / v_e)$, was calculated from the estimated values of K^{trans} and v_e. The ROIs used for the tumor volume measurements were downsampled to match the image resolution of the DCE-MRI data, and the median K^{trans}, k_{ep}, and v_e were quantified from multiple slices across the tumor volume.

The fitting routine incorporated 1) the pre-contrast T_1 value, 2) the fast exchange limit model with relaxivity for gadopentetate at 7T, r_1 = 4.72/mM/s (21), and 3) a population-derived vascular input function collected from a cohort of 10 athymic female mice using the identical protocol described by Loveless et al. (21). The population-derived vascular input function was calibrated for each animal in the current study using the method previously described by Li et al. (22). Briefly, a region of interest was drawn across three slices in the muscle to generate an averaged signal intensity time course, which was then fit to the two-compartment model in an iterative fashion until the v_e of

the muscle equaled a physiologically relevant value, i.e., 0.11 (23). With each iteration the peak of the population-derived concentration time course was altered. This process was repeated until the muscle v_e equaled 0.11 (22).

Histological Analysis

Animals were sacrificed immediately following imaging at day 4, and excised tumors were fixed in 10% formalin for at least 24 hours. Samples were then transferred to 70% ethanol and stored in 4 °C. Samples were blocked in paraffin and sectioned with 4-micron thick slices. Immunohistochemistry for CD31 (CM303; Biocare Medical, Concord, CA) and hematoxylin and eosin (H&E) was performed on consecutively sectioned slides. Stained sections were imaged at 20× magnification using a Leica SCN400 Slice Scanner (Leica, Buffalo Grove, IL). Unbiased and automated image analysis was performed with associated software packages that use trained algorithms based on shape and intensity of the stain. Microvessel density was quantified from CD31 stained sections by counting the number of positively stained vessels and dividing it by the area of the tissue section. The percentage of extracellular space (EC%) was quantified as previously described (11). Briefly, a region was manually drawn around the entire tissue section, and every pixel was analyzed to determine whether it contained enough staining to be counted. Pixels that did not reach this threshold were considered unstained (i.e., extracellular regions). The EC% was calculated using Eq. (VIII-4):

$$EC\% = \left(\frac{A_{ROI} - A_{stain}}{A_{roi}} \right) \times 100, \qquad \text{(VIII-4)}$$

where A_{ROI} is the thresholding that includes the total area of the tissue section and A_{stain} is the total stained area. Tumor sections from 4-5 mice from each cohort were analyzed for

comparison with *in vivo* data. Microvessel density measurements were compared with DCE-MRI measurements relating to perfusion/blood flow (e.g., K^{trans}, k_{ep}). The EC% was compared with the extracellular extravascular volume fraction (i.e., v_e).

Statistics

Three statistical comparisons were performed in this study: 1) trastuzumab versus vehicle treated BT474 cohorts, 2) trastuzumab versus vehicle treated HR6 cohorts, and 3) responders (BT474 treated) versus nonresponders (HR6 treated). Longitudinal DCE-MRI parameters were compared within and between cohorts at each time point. Microvessel density and EC% were compared between cohorts. All data are presented as mean ± SE. All statistical comparisons were evaluated using the nonparametric Wilcoxon rank sum test in MATLAB version 2010b, and data were considered significant if $p < 0.05$.

Results

Impact of Trastuzumab on Tumor Xenograft Growth

Longitudinal tumor volumes for the trastuzumab and vehicle treated BT474 cohorts are displayed in Figure VIII-2A. There was no statistically significant difference in tumor volume between these cohorts at the measured timed points (baseline: $p = 0.76$; day 1: $p = 0.64$; day 4: $p = 0.20$). In the vehicle treated group, tumor size steadily increased over time yet differences after treatment were not statistically significant at day 1: $p = 0.55$, compared to baseline) or day 4 ($p = 0.29$, compared to baseline). Trastuzumab inhibited tumor growth in the trastuzumab treated group, although

differences were not statistically significant at day 1 ($p = 0.53$, compared to baseline) or day 4 ($p = 0.41$, compared to baseline).

Longitudinal tumor volumes for the trastuzumab and vehicle treated HR6 cohorts are displayed in Figure VIII-2B. Again, there was no statistically significant difference in tumor volume between these cohorts at the measured timed points (baseline: $p = 0.35$; day 1: $p = 0.44$; day 4: $p = 0.54$). In the vehicle treated group, non-significant increases in tumor size were observed at day 1 ($p = 0.65$, compared to baseline), and day 4 ($p = 0.75$, compared to baseline). In the trastuzumab treated group, tumor size steadily increased over time yet differences after treatment were also not statistically different day 1 ($p = 0.84$, compared to baseline) or day 4 ($p = 0.84$, compared to baseline).

To evaluate the impact of trastuzumab on tumor xenografts with different trastuzumab sensitivities, longitudinal tumor volume from the trastuzumab treated BT474 (responder) and HR6 (nonresponder) cohorts are graphed for comparison in Figure VIII-2C. Similar to the other cohort comparisons, differences in tumor volume between responders and nonresponders were not statistically significant at any of the measured time points (baseline: $p = 0.76$; day 1: $p = 0.53$; day 4: $p = 0.29$).

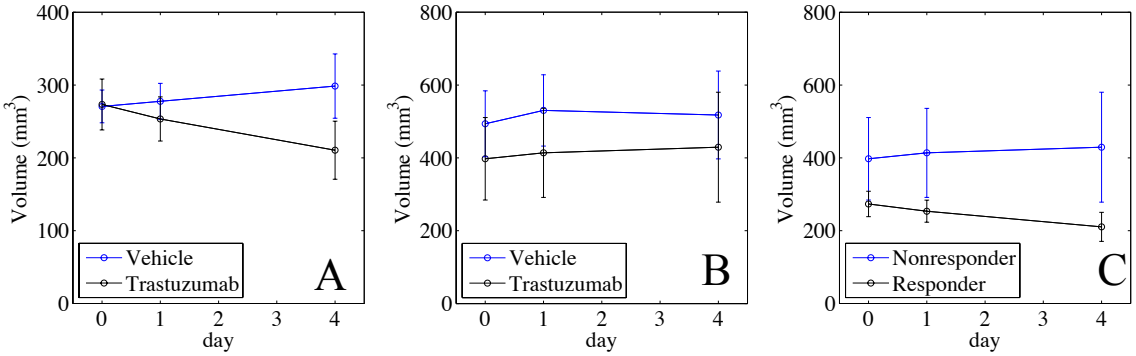

Figure VIII-2. Impact of trastuzumab on tumor growth in the: (A) trastuzumab sensitive BT474, (B) trastuzumab resistant HR6, and (C) trastuzumab treated BT474 and HR6 xenografts. Tumor volume was measured from T_2-weighted MR images. Significant differences were not observed between cohorts at any of the measured time points.

DCE-MRI Assesses Early Treatment Response Between BT474 Cohorts

Figure VIII-3 displays the representative parametric maps of K^{trans} and v_e for a mouse in the trastuzumab and vehicle treated BT474 groups. The tumor parametric maps are superimposed onto one of the baseline serial T_1-weighted images for anatomical reference. The K^{trans} parametric maps illustrate a marked increase in K^{trans} with the trastuzumab treated group compared to the vehicle control. This result was unexpected considering the previously observed antiangiogenic effects of trastuzumab (5,6). We return to this point in the Discussion. Additionally, a slight increase in longitudinal v_e is observed in the trastuzumab treated group compared to the controls.

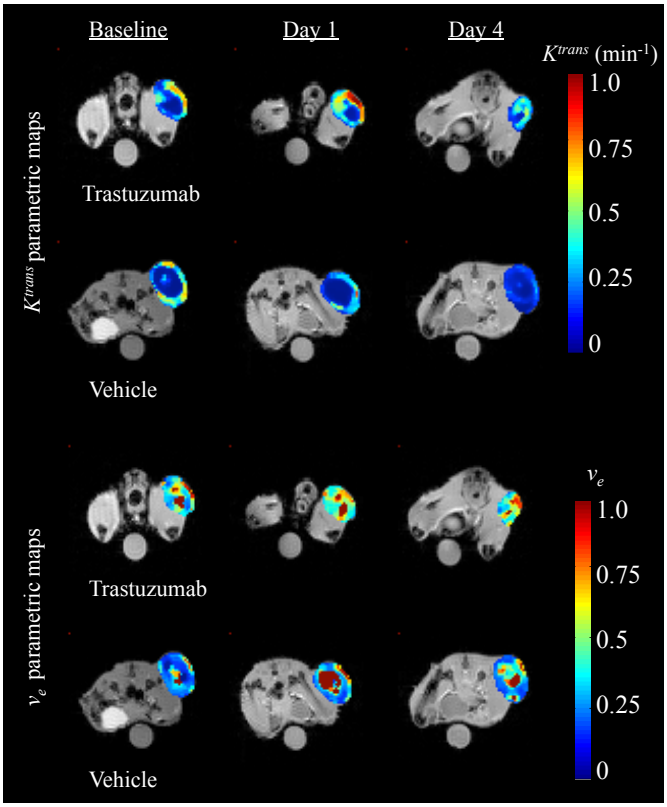

Figure VIII-3. Parametric maps of K^{trans} and v_e are displayed for a representative animal from each trastuzumab and vehicle treated BT474 cohort. Note the marked increase in K^{trans} at day 1 with the treated animal compared with the control animal. This result was unexpected due to the antiangiogenic effects of trastuzumab. Also note the slight increase in longitudinal v_e in the trastuzumab treated animal compared to the relatively no change in v_e for the control animal. For viewing purposes only, voxels with $v_e > 1$ were set to 1.

Figure VIII-4 displays longitudinal changes in K^{trans} (left panel), k_{ep} (center panel), and v_e (right panel) in the BT474 cohorts. A significant difference in K^{trans} is observed at day 4 between the trastuzumab and vehicle treated cohorts (Figure VIII-4A, $p = 0.03$). At day 4, the K^{trans} of the trastuzumab treated group was significantly higher than the vehicle treated group, which was unexpected considering the previous observed antiangiogenic effects of trastuzumab (5,6). We return to this point in the Discussion. In the trastuzumab treated group, a non-significant increase was observed at day 1 ($p = 1.00$, compared to baseline) while a significant increase in K^{trans} was observed at day 4 ($p = 0.04$, compared to baseline). In the vehicle treated group, non-significant decreases in K^{trans} were observed at day 1 ($p = 1.00$, compared to baseline) and day 4 ($p = 0.9$, compared to baseline).

Significant differences in k_{ep} were not observed at any time point during the study between the BT474 trastuzumab and vehicle treated cohorts (Figure VIII-4B; baseline: $p = 0.53$; day 1: $p = 0.88$; day 4: $p = 0.11$). In the trastuzumab treated group, a non-significant decrease in k_{ep} was observed at day 1 ($p = 0.62$, compared to baseline) followed by a non-significant increase at day 4 ($p = 0.23$, compared to baseline). In the vehicle treated group, non-significant decreases in k_{ep} were observed at day 1 ($p = 0.84$, compared to baseline) and day 4 ($p = 1.00$, compared to baseline).

A significant difference in v_e was observed at day 4 between the trastuzumab and vehicle treated cohorts (Figure VIII-4C, $p = 0.03$). In the trastuzumab treated group, a trend towards a significant increase in v_e was observed at day 1 ($p = 0.07$, compared to baseline) followed by a significant increase at day 4 ($p = 0.006$, compared to baseline). In

the vehicle treated group, non-significant increases in v_e were observed at day 1 (p = 0.31, compared to baseline) and day 4 (p = 0.56, compared to baseline).

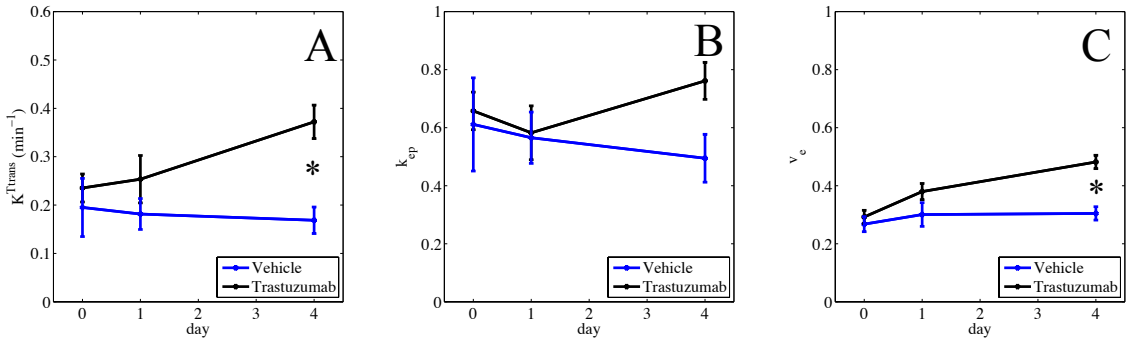

Figure VIII-4. Longitudinal changes in the pharmacokinetic parameters derived from DCE-MRI data. Early changes (i.e., before tumor size) in K^{trans} (A) and v_e (C) were observed between the trastuzumab and vehicle treated BT474 cohorts. Differences in k_{ep} between cohorts were not statistically significant at any of the time points (B). * $p < 0.05$

Representative examples of CD31 and H&E tissue sections for a mouse from each BT474 cohort are illustrated at 20× magnification in Figure VIII-5. The amount of CD31 staining appears to be larger in the trastuzumab treated animal compared to the vehicle treated animal (Figure VIII5-A, *top row*). This qualitative observation was supported by the significant increase in microvessel density from the trastuzumab treated BT474 mice compared to the controls (Figure VIII-5B; p = 0.03). The significant difference in CD31 between these two cohorts corresponds with the *in vivo* data for K^{trans} (Figure VIII-4A). Qualitatively, it appears that the H&E tissue section from the trastuzumab treated animal has more extracellular space than the tumor from the vehicle treated tumor (Figure VIII5-A, *bottom row*). This qualitative observation was supported by the observed significant difference in EC% (Figure VIII-5C). Additionally, this significant difference in EC% corresponds with the observed significant difference in v_e (Figure VIII-5C).

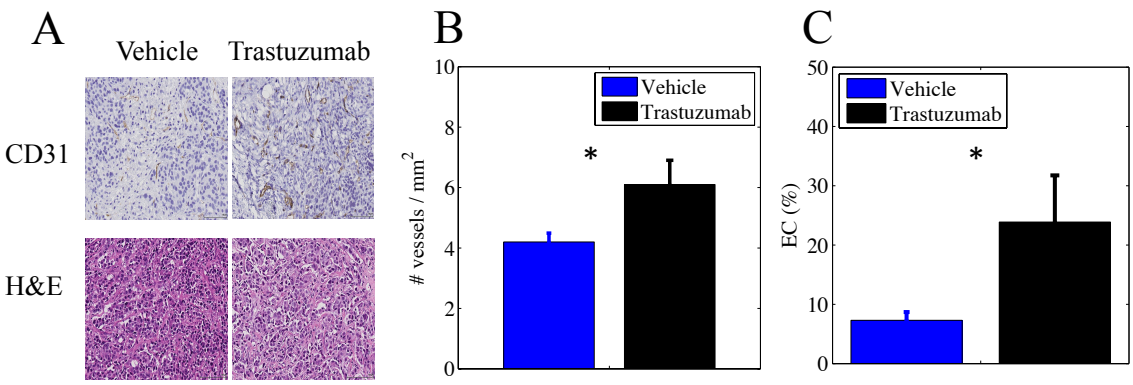

Figure VIII-5. CD31 and H&E histology comparisons between the trastuzumab and vehicle treated BT474 cohorts. It can be observed from the sample CD31 stains that the trastuzumab treated cohort has increased CD31 staining (A, *top row*). This observation is supported by the significant increase in microvessel density from the trastuzumab treated cohort compared to the controls (B). It can be observed from the sample H&E stains that the trastuzumab treated group has an increased amount of extracellular space compared to the vehicle treated group (A, *bottom row*). This observation is also supported by the significant increase in EC% from the trastuzumab treated cohort (C). * $p < 0.05$

No Difference in DCE-MRI Pharmacokinetic Parameters Between HR6 Cohorts

Figure VIII-6 displays representative parametric maps of K^{trans} and v_e for a mouse in the trastuzumab and vehicle treated HR6 groups. The tumor parametric maps are superimposed onto one of the baseline serial T_1-weighted images for anatomical reference. It can be observed qualitatively from these images that minimal changes in K^{trans} and v_e occur longitudinally in these cohorts. Additionally, both the K^{trans} and v_e values appear to be similar between the trastuzumab and vehicle treated HR6 groups.

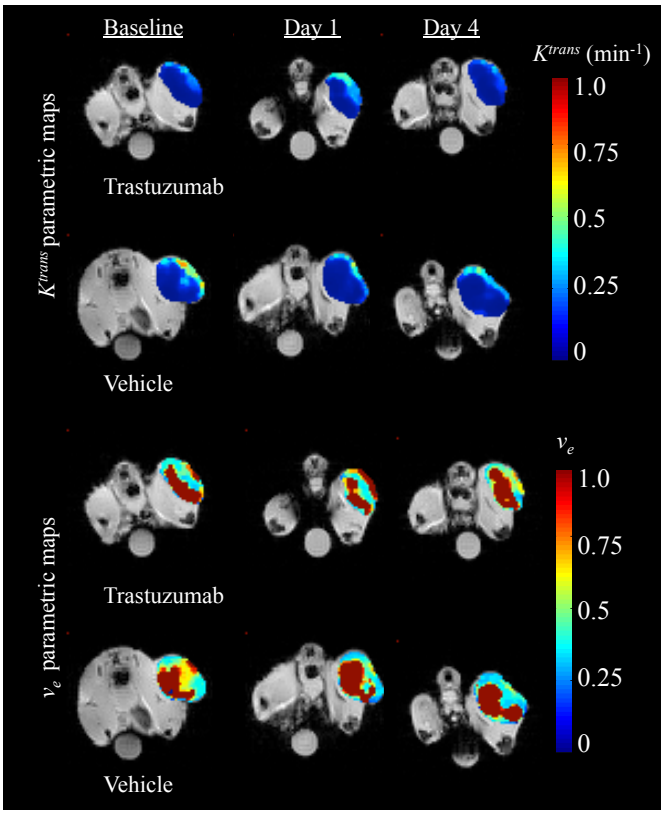

Figure VIII-6. Parametric maps of K^{trans} and v_e are displayed for a representative animal from each trastuzumab and vehicle treated HR6 cohort. Note how neither of these parameters change longitudinally in both of these cohorts. For viewing purposes only, voxels with $v_e > 1$ were set to 1.

The group average for the actual parameter values and percent change is graphed at each measured time point in Figure VIII-7 for the trastuzumab and vehicle treated HR6 cohorts, where K^{trans}, k_{ep}, and v_e are shown in the left, center, and right panels, respectively. The difference in K^{trans} between the HR6 cohorts was not statistically significant at any time point (Figure VIII-7A; baseline: $p = 0.28$; day 1: $p = 0.53$; day 4: $p = 1.00$). In the trastuzumab treated HR6 group, the decrease in K^{trans} trended towards significance at day 1 ($p = 0.06$, compared to baseline), and then was followed by a non-significant increase at day 4 ($p = 0.84$, compared to baseline). In the vehicle treated

group, non-significant increases in K^{trans} were observed at day 1 (p = 0.80, compared to baseline) and at day 4 (p = 0.49, compared to baseline).

Significant differences in k_{ep} were not observed at any time point during the study between the HR6 trastuzumab and vehicle treated cohorts (Figure VIII-7B; baseline: p = 0.94; day 1: p = 0.28; day 4: p = 0.54). In the trastuzumab treated group, non-significant decreases in k_{ep} were observed at day 1 (p = 0.22, compared to baseline) and day 4 (p = 0.69, compared to baseline). In the vehicle treated group, a non-significant decrease in k_{ep} was observed at day 1 (p = 0.13, compared to baseline), which was followed by a non-significant increase at day 4 (p = 0.61, compared to baseline).

Significant differences in v_e were not observed at any time point during the study between the HR6 trastuzumab and vehicle treated cohorts (Figure VIII-7C; baseline: p = 0.28; day 1: p = 1.00; day 4: p = 0.13). In the trastuzumab treated group, a non-significant decrease in v_e was observed at day 1 (p = 1.00, compared to baseline), which was followed by an increase in v_e that trended towards significance (p = 0.07, compared to baseline). In the vehicle treated group, non-significant increases in v_e were observed at day 1 (p = 0.51, compared to baseline) and day 4 (p = 0.18, compared to baseline).

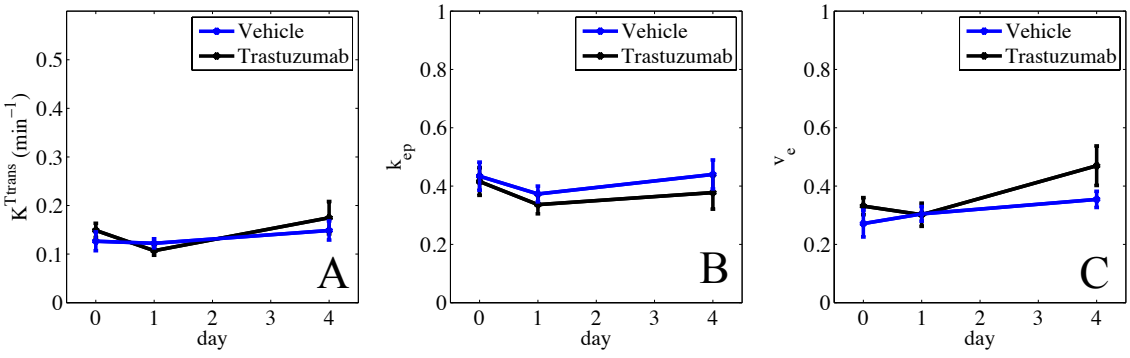

Figure VIII-7. Longitudinal changes in the pharmacokinetic parameters derived from DCE-MRI data. Significant differences between cohorts were not observed with any of the pharmacokinetic parameters at the measured time points.

Representative examples of CD31 and H&E tissue sections for a mouse from each HR6 cohort are illustrated at 20× magnification in Figure VIII-8. The amount of CD31 staining between the trastuzumab and vehicle treated cohorts appears to be similar (Figure VIII8-A, top row). This qualitative observation was supported by the similar microvessel density measurements between the cohorts (Figure VIII-8B; $p = 1.00$). The non-significant difference in CD31 between these two cohorts corresponds with the *in vivo* data for K^{trans} (Figure VIII-8A). Qualitatively, it appears that the H&E tissue section from the trastuzumab treated animal (lower right) has slightly more extracellular space than the vehicle treated animal (lower left). This observation is supported by the trend in EC% (Figure VIII-7C), where the EC% calculated from the trastuzumab treated HR6 cohort was larger than the vehicle controls; however, the difference between cohorts was not statistically significant ($p = 0.19$). Additionally, the trend in EC% corresponds with the trend in v_e values observed in the trastuzumab treated cohort of HR6 tumor-bearing mice (Figure VIII-7C).

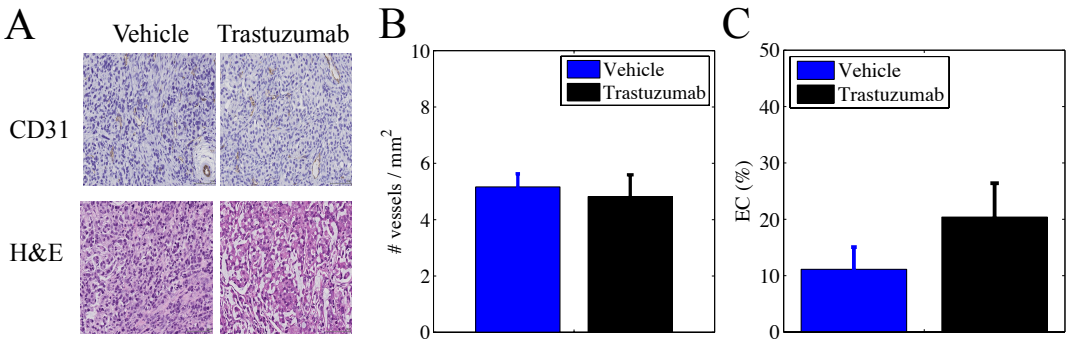

Figure VIII-8. CD31 and H&E histology comparisons between the trastuzumab and vehicle treated HR6 cohorts. It can be observed from the samples that the CD31 staining is similar between cohorts (A, *top row*). This observation is supported by the non-significant difference in microvessel density (B, $p = 1.00$). It can be observed from the sample H&E stains that the trastuzumab treated group might have a slightly larger EC% compared to the vehicle group (A, *bottom row*). This observation was also observed by the increase in EC% from the trastuzumab treated cohort, however the difference between cohorts was not statistically significant (C, $p = 0.19$).

DCE-MRI Evaluation of Treatment Response Between Responders and Nonresponders

The group average for the actual parameter values and percent change is graphed at each measured time point in Figure VIII-9 for the responders (BT474 treated) and nonresponders (HR6 treated), where K^{trans}, k_{ep}, and v_e are shown in the left, center, and right panels, respectively. The difference in K^{trans} between these cohorts was statistically significant at all time points during the study (Figure VIII-9A; baseline: $p = 0.03$; day 1: $p = 0.005$; day 4: $p = 0.02$). The difference in k_{ep} between these cohorts was statistically significant at baseline (Figure VIII-9A, $p = 0.02$), trended towards significance at day 1 ($p = 0.05$), and then was significantly different again at day 4 ($p = 0.02$). The difference in v_e between these cohorts was not statistically significant at the measured time points (Figure VIII-9C; baseline: $p = 0.34$; day 1: $p = 0.15$; day 4: $p = 1.00$).

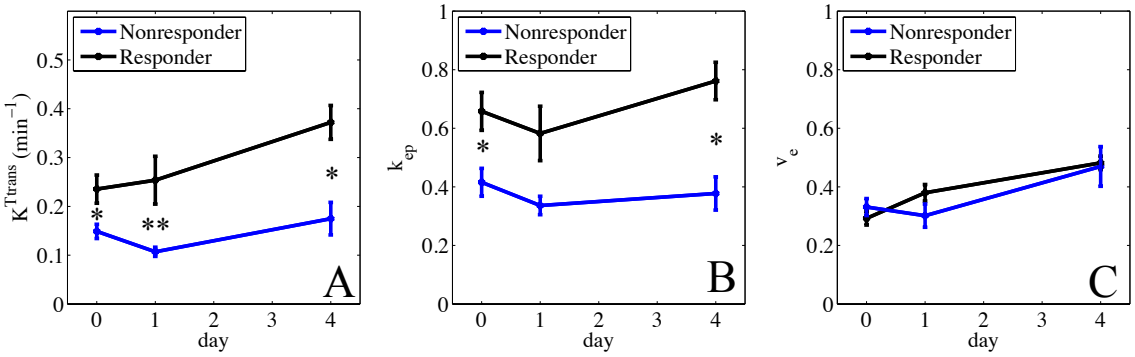

Figure VIII-9. Longitudinal changes in the pharmacokinetic parameters derived from DCE-MRI data for the responders and nonresponders. Significant differences in K^{trans} were observed at all of the measured time points (A). Similar to K^{trans}, significant differences in k_{ep} were observed between cohorts at baseline and day 4 (B); the difference between cohorts at day 1 trended towards significance ($p = 0.05$). No statistically significant differences in v_e were observed at the measured time points (C). *$p < 0.05$, **$p < 0.01$.

Representative examples of CD31 and H&E tissue sections for a mouse from each BT474 treated and HR6 treated cohorts are illustrated at 20× magnification in Figure

VIII-10. Microvessel density is increased in the responder group (which corresponds to the *in vivo* K^{trans} data; Figure VIII-9A), however the difference between the groups is not statistically significant (p = 0.42). Additionally, the EC% is slightly increased in the responder group, however the difference is not statistically significant (p = 0.90). Furthermore, the non-significant difference in EC% corresponds with the non-significant difference in v_e observed between these cohorts (Figure VIII-9C).

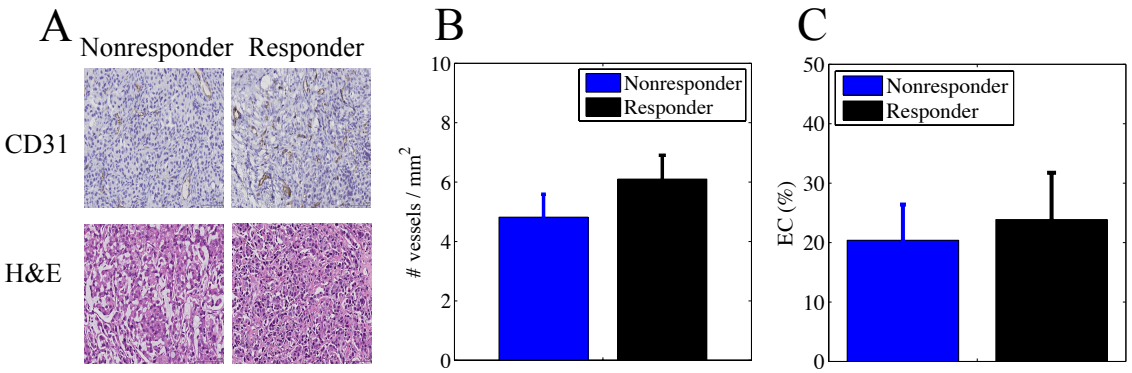

Figure VIII-10. CD31 and H&E histology comparisons between the responder and nonresponder cohorts. Microvessel density in the responder group is slightly increased compared to the nonresponders, however the difference is not statistically significant (B, p = 0.42). Similarly, the EC% in the responder group is slightly increased, but again the difference is not statistically significant (C, p = 0.90). Although not significant, the trends in both the microvessel density and EC% correspond with the *in vivo* DCE-MRI data.

Discussion

The main mechanism of action of trastuzumab appears to be the disruption of downstream cell signaling pathways leading to inhibition of cellular proliferation and survival (2,4). A secondary mechanism of action has been observed where trastuzumab acts as an antiangiogenic agent to reduce vascular volume and flow (5). The former observation will occur, by definition, earlier than changes in tumor size. Additionally, treatment-induced changes in tumor vasculature might also occur sooner than changes in tumor morphology. Thus, one of the unique advantages of imaging tumor physiology is

that quantitative functional and molecular imaging techniques have the ability to capture treatment-induced changes before any palpable/volumetric changes in tumor growth are observed; thus, providing early response assessments. The goals of this study were to examine the sensitivity of DCE-MRI to: 1) assess early treatment response in HER2+ breast cancer xenografts that are trastuzumab responsive, and 2) differentiate between trastuzumab responsive and resistant HER2+ breast cancer xenografts exposed to trastuzumab.

An early treatment-induced change in K^{trans} was observed between the trastuzumab and vehicle treated BT474 cohorts. Interestingly, K^{trans} of the trastuzumab treated group was significantly higher than the vehicle group. This result was unexpected considering the previously observed antiangiogenic effects of trastuzumab (5,6). Additionally, we hypothesized that K^{trans} would decrease with effective treatment, as has been previously observed with other antiangiogenic agents (11,13). When we quantified the microvessel density measurements, however, we observed a significant increase in the trastuzumab treated cohorts. Thus, the histological result corresponds with the *in vivo* K^{trans} measurement. The increase in microvessel density and the subsequent increase in K^{trans} in the trastuzumab treated cohort could be explained by an increase in vascular volume contributing to an increase in vessel flow that in turn increases K^{trans} (in a flow-limited regime (20)). However, it is well known that K^{trans} is a mixed parameter, reflecting on vessel flow, vessel permeability, or most often in tumors, a combination of the two (20). In this experiment, it is almost impossible to tease out the different contributions of vessel flow and permeability from the K^{trans} measurement. To investigate to what extent trastuzumab affects vessel flow or permeability, a future DCE-MRI

experiment with a larger-sized contrast agent (e.g., albumin-Gd-DTPA (24)) could be used so that K^{trans} reflects vessel permeability. For example, if trastuzumab affects permeability, then K^{trans} would decrease with a larger contrast agent. However, an increase in K^{trans} would reflect a trastuzumab-induced change in vessel flow.

In addition to microvessel density measurements assessed *via* CD31 staining, employing another histological marker that reflects vessel perfusion instead of just vessel morphology would add to the physiological understanding of K^{trans}. For example, Moasser et al. used fluorescein isothiocyanate (FITC)-labeled lectin perfusion studies in addition to CD31 staining in order to glean information about the tumor morphology and functionality during a DCE-MRI evaluation of treatment response with an epidermal growth factor receptor inhibitor (24).

Another plausible explanation for the significant increase in K^{trans} observed from the trastuzumab treated BT474 cohort is the idea of "tumor remodeling". Suppose that before any treatment, the whole tumor volume has areas of viable and necrotic regions. After treatment the necrotic regions might shrink with tumor volume, resulting in an apparent increase in K^{trans} as there is now less necrotic voxels that consequently have lower K^{trans} values contributing to the whole tumor measurement. Future analyses to investigate changes in the distribution of K^{trans} (i.e., histogram analysis or regional clustering) might provide more information than just reporting one summary statistics from the whole tumor volume.

An early treatment-induced change in v_e was also observed between the trastuzumab and vehicle treated BT474 cohorts. The v_e value of the trastuzumab treated group was significantly higher than the vehicle group. This was an expected result

considering that trastuzumab inhibits cellular proliferation causing an increase in extracellular space, which in turn results in an increase in the extravascular extracellular volume fraction, v_e. When we quantified the percentage of extracellular space (i.e., EC%) from H&E tissue sections, we observed a significant increase in EC% in the trastuzumab treated cohorts. Thus, the histological result corresponds with the *in vivo* v_e measurement.

We also demonstrated that parameters derived from quantitative DCE-MRI analyses are not different between trastuzumab and vehicle treated mice with trastuzumab-resistant (i.e., HR6) xenografts although one cohort was receiving therapy that was intended to alter cellular proliferation and vascular physiology. Both of the histological parameters supported the *in vivo* data, as significant differences in microvessel density and EC% were not observed between the groups. These results then allowed for the comparison between the so-called responders and nonresponders, or the trastuzumab-treated BT474 and HR6 cohorts, respectively.

DCE-MRI parameters relating to vascular flow and permeability (i.e. K^{trans}, k_{ep}) were significantly different between responders and nonresponders at baseline. K^{trans} continued to be significantly different at both time points after the initiation of treatment, and k_{ep} was significantly different at day 4. These results not only suggest that DCE-MRI can differentiate between trastuzumab sensitivities, but that K^{trans} and k_{ep} might be prognostic factors for trastuzumab effectiveness. Although we did not observe a statistical difference in microvessel density, the expected trend (i.e., microvessel density is higher in the responder group) was observed. A statistical difference in v_e was not observed between the responders and nonresponders, which was corroborated by the non-significant difference in EC%.

Study Limitations

The optimal imaging time points for this study were determined from a separate group of trastuzumab and vehicle treated mice with BT474 xenografts (see Chapter VI). Although a significant difference in tumor volume was observed at day 4 in the previous study, treatment-induced differences in tumor volume were not statistically different at day 4 in the current study. Thus, due to the variability of mouse physiology and treatment efficiency, a true study endpoint based on tumor size changes was not achieved in the current study. This is not ideal, especially in studies that are evaluating if an imaging parameter is a biomarker of early treatment response; however, the trends in tumor volume changes were as expected.

Quantitative analysis of DCE-MRI requires the concentration of the contrast agent in the plasma. As noted in Chapter III, the gold standard for this measurement is blood sampling. However, the difficulty of collecting blood samples at a sufficient temporal resolution, particularly in small animals, limits the efficiency of this method. Thus, we employed a population-derived vascular input function collected from a group of gender and age matched population of mice. We note that the use of a population-derived vascular input function can lead to parameter errors due to the overestimation or underestimation of the contrast agent concentration in the plasma (i.e., C_p) in individual subjects. Error in the measurement of C_p would manifest itself in errors of the derived parameters, i.e., K^{trans} and v_e. Recognizing this is as a potential limitation of the study, we used the method previously described by Li et al. to calibrate the population-derived input function for each mouse based on the characteristics of a known tissue, which in this study was the v_e of muscle (22). After setting the v_e of muscle to a certain value (i.e.,

0.11), we then adjusted the peak concentration of the population-derived input function in order to better reflect the actual pharmacokinetics for each animal. However, errors could still occur resulting in unphysical values, for example, $v_e > 1$. Thus, we eliminated those voxels from the whole tumor analysis as including them would have skewed the K^{trans}, k_{ep}, and v_e measurements.

Conclusion

DCE-MRI is an emerging quantitative imaging technique that offers noninvasive measurements of vascular physiology and tissue volume fractions. Efforts to evaluate the ability of DCE-MRI data to provide early response assessments as well as prognostic indicators of eventual response are ongoing. The results from this study suggest that DCE-MRI parameters K^{trans} and v_e are early biomarkers of response in trastuzumab sensitive HER2+ xenografts. Furthermore, this work shows that DCE-MRI has the potential sensitivity to differentiate between HER2+ xenografts with varying trastuzumab sensitivities (i.e., BT474 versus HR6). The latter result potentially has significant clinical impact as the development of imaging methods that can separate responders from nonresponders earlier during the course of therapy is of great interest in order to reduce medical cost and negative systemic effects caused by ineffective therapies.

References

1. Dean-Colomb W, Esteva FJ. Her2-positive breast cancer: herceptin and beyond. Eur J Cancer 2008;44(18):2806-2812.
2. Spector NL, Blackwell KL. Understanding the mechanisms behind trastuzumab therapy for human epidermal growth factor receptor 2-positive breast cancer. J Clin Oncol 2009;27(34):5838-5847.
3. Ross JS, Fletcher JA. The HER-2/neu oncogene in breast cancer: prognostic factor, predictive factor, and target for therapy. Stem Cells 1998;16(6):413-428.
4. Nahta R, Esteva FJ. HER2 therapy: molecular mechanisms of trastuzumab resistance. Breast Cancer Res 2006;8(6):215.
5. Izumi Y, Xu L, di Tomaso E, Fukumura D, Jain RK. Tumour biology: herceptin acts as an anti-angiogenic cocktail. Nature 2002;416(6878):279-280.
6. Klos KS, Zhou X, Lee S, Zhang L, Yang W, Nagata Y, Yu D. Combined trastuzumab and paclitaxel treatment better inhibits ErbB-2-mediated angiogenesis in breast carcinoma through a more effective inhibition of Akt than either treatment alone. Cancer 2003;98(7):1377-1385.
7. Loveless ME, Whisenant JG, Wilson K, Lyshchik A, Sinha TK, Gore JC, Yankeelov TE. Coregistration of ultrasonography and magnetic resonance imaging with a preliminary investigation of the spatial colocalization of vascular endothelial growth factor receptor 2 expression and tumor perfusion in a murine tumor model. Mol Imaging 2009;8(4):187-198.
8. Cosgrove D, Lassau N. Imaging of perfusion using ultrasound. Eur J Nucl Med Mol Imaging 2010;37 Suppl 1:S65-85.
9. Naish JH, McGrath DM, Bains LJ, Passera K, Roberts C, Watson Y, Cheung S, Taylor MB, Logue JP, Buckley DL, Tessier J, Young H, Waterton JC, Parker GJ. Comparison of dynamic contrast-enhanced MRI and dynamic contrast-enhanced CT biomarkers in bladder cancer. Magn Reson Med 2011;66(1):219-226.
10. Yankeelov TE, Gore JC. Dynamic Contrast Enhanced Magnetic Resonance Imaging in Oncology: Theory, Data Acquisition, Analysis, and Examples. Curr Med Imaging Rev 2009;3(2):91-107.
11. Loveless ME, Lawson D, Collins M, Nadella MV, Reimer C, Huszar D, Halliday J, Waterton JC, Gore JC, Yankeelov TE. Comparisons of the efficacy of a Jak1/2 inhibitor (AZD1480) with a VEGF signaling inhibitor (cediranib) and sham treatments in mouse tumors using DCE-MRI, DW-MRI, and histology. Neoplasia 2012;14(1):54-64.
12. Marzola P, Degrassi A, Calderan L, Farace P, Nicolato E, Crescimanno C, Sandri M, Giusti A, Pesenti E, Terron A, Sbarbati A, Osculati F. Early antiangiogenic activity of SU11248 evaluated in vivo by dynamic contrast-enhanced magnetic resonance imaging in an experimental model of colon carcinoma. Clin Cancer Res 2005;11(16):5827-5832.
13. Haney CR, Fan X, Markiewicz E, Mustafi D, Karczmar GS, Stadler WM. Monitoring anti-angiogenic therapy in colorectal cancer murine model using dynamic contrast-enhanced MRI: comparing pixel-by-pixel with region of interest analysis. Technol Cancer Res Treat 2013;12(1):71-78.

14. Li X, Arlinghaus LR, Ayers GD, Chakravarthy AB, Abramson RG, Abramson VG, Atuegwu N, Farley J, Mayer IA, Kelley MC, Meszoely IM, Means-Powell J, Grau AM, Sanders M, Bhave SR, Yankeelov TE. DCE-MRI analysis methods for predicting the response of breast cancer to neoadjuvant chemotherapy: Pilot study findings. Magn Reson Med 2013.
15. Chawla S, Kim S, Dougherty L, Wang S, Loevner LA, Quon H, Poptani H. Pretreatment diffusion-weighted and dynamic contrast-enhanced MRI for prediction of local treatment response in squamous cell carcinomas of the head and neck. AJR Am J Roentgenol 2013;200(1):35-43.
16. Harry VN, Semple SI, Parkin DE, Gilbert FJ. Use of new imaging techniques to predict tumour response to therapy. Lancet Oncol 2010;11(1):92-102.
17. Padhani AR, Liu G, Koh DM, Chenevert TL, Thoeny HC, Takahara T, Dzik-Jurasz A, Ross BD, Van Cauteren M, Collins D, Hammoud DA, Rustin GJ, Taouli B, Choyke PL. Diffusion-weighted magnetic resonance imaging as a cancer biomarker: consensus and recommendations. Neoplasia 2009;11(2):102-125.
18. Ritter CA, Perez-Torres M, Rinehart C, Guix M, Dugger T, Engelman JA, Arteaga CL. Human breast cancer cells selected for resistance to trastuzumab in vivo overexpress epidermal growth factor receptor and ErbB ligands and remain dependent on the ErbB receptor network. Clin Cancer Res 2007;13(16):4909-4919.
19. Kety SS. The theory and applications of the exchange of inert gas at the lungs and tissues. Pharmacol Rev 1951;3(1):1-41.
20. Tofts PS, Brix G, Buckley DL, Evelhoch JL, Henderson E, Knopp MV, Larsson HB, Lee TY, Mayr NA, Parker GJ, Port RE, Taylor J, Weisskoff RM. Estimating kinetic parameters from dynamic contrast-enhanced T(1)-weighted MRI of a diffusable tracer: standardized quantities and symbols. J Magn Reson Imaging 1999;10(3):223-232.
21. Loveless ME, Halliday J, Liess C, Xu L, Dortch RD, Whisenant J, Waterton JC, Gore JC, Yankeelov TE. A quantitative comparison of the influence of individual versus population-derived vascular input functions on dynamic contrast enhanced-MRI in small animals. Magn Reson Med 2012;67(1):226-236.
22. Li X, Rooney WD, Varallyay CG, Gahramanov S, Muldoon LL, Goodman JA, Tagge IJ, Selzer AH, Pike MM, Neuwelt EA, Springer CS, Jr. Dynamic-contrast-enhanced-MRI with extravasating contrast reagent: rat cerebral glioma blood volume determination. J Magn Reson 2010;206(2):190-199.
23. Donahue KM, Weisskoff RM, Parmelee DJ, Callahan RJ, Wilkinson RA, Mandeville JB, Rosen BR. Dynamic Gd-DTPA enhanced MRI measurement of tissue cell volume fraction. Magn Reson Med 1995;34(3):423-432.
24. Moasser MM, Wilmes LJ, Wong CH, Aliu S, Li KL, Wang D, Hom YK, Hann B, Hylton NM. Improved tumor vascular function following high-dose epidermal growth factor receptor tyrosine kinase inhibitor therapy. J Magn Reson Imaging 2007;26(6):1618-1625.

CHAPTER IX

ASSESSING TREATMENT RESPONSE IN HER2+ MURINE MODELS OF BREAST CANCER WITH DIFFUSION-WEIGHTED MRI

Introduction

Imaging biomarkers that can detect and characterize cancer as well as monitor the response to therapy are of great interest. Diffusion-weighted magnetic resonance imaging (DW-MRI) is a promising technique as it provides a noninvasive, quantitative characterization of tumor cytoarchitecture, data acquisition does not require an exogenous contrast agent, and can be obtained relatively rapidly (1). DW-MRI depends on the microscopic, thermally-induced behavior of water molecules moving in a random pattern, classically referred to as Brownian motion. In a system defined by small compartments (e.g., cellular tissues) that are separated by semi-permeable membranes, the rate of Brownian motion or self-diffusion will be less than that of free diffusion. In cellular tissues, this rate of self-diffusion is described by an apparent diffusion coefficient (ADC), which is influenced by the number, permeability, and separation of barriers that act to restrict the free diffusion of water molecules (2). DW-MRI maps the ADC, and in well-controlled situations the variations in ADC have been shown to correlate inversely with tissue cellularity (3).

Since a hallmark of cancer is uncontrolled tumor growth leading to high cell density and loss of normal cytoarchitecture (4), DW-MRI could provide an early biomarker of biological abnormality. Thus, the development of DW-MRI methods that

can provide an earlier assessment of disease response is an active area of research. It has been shown, in preclinical (2,5-7) and clinical (8-10) settings, that exposure of tumors to both chemotherapy and radiotherapy consistently leads to measurable increases in water diffusion in cases of favorable response. However, before any of these methods can be employed in routine clinical care, a systematic evaluation is required, which includes the assessment of protocol reproducibility, treatment response evaluation in a variety of cancer types and treatment regimens, and development of validation methods to assist in the interpretation of the imaging findings. This Dissertation performed a systematic evaluation of DW-MRI in HER2+ breast cancer xenografts that are sensitive and resistant to trastuzumab. The study discussed in Chapter V assessed DW-MRI reproducibility and provided a measurement of protocol variability. The work discussed in this chapter explored the utility of DW-MRI to provide an early therapeutic response assessment. This study also quantified a histological correlate to help provide an interpretation of the *in vivo* imaging findings.

Materials and Methods

Cell Culture

Trastuzumab responsive (BT474) and resistant (HR6) cells were gifts from Dr. Carlos Arteaga, M.D. at Vanderbilt University. HR6 cells were harvested from BT474 xenografts as described previously (11). Briefly, female athymic mice with BT474 xenografts were treated twice per week with 20 mg/kg trastuzumab diluted in sterile saline. Tumors that initially responded completely and then recurred in the presence of maintained trastuzumab treatment were harvested, minced, and digested to generate the

HR6 cell line (11). Both cell lines were cultured in improved minimal essential medium (IMEM, Invitrogen, Carlsbad, CA) supplemented with 10% fetal bovine serum at 37°C in a humidified, 5% CO_2 incubator. To maintain trastuzumab resistance, HR6 cells were also cultured with 10 mg/ml trastuzumab as previously described (11). Trastuzumab was purchased from the Vanderbilt University Hospital Pharmacy (Nashville, TN). Cells were harvested with trypsin at approximately 85% confluence.

Tumor Xenograft Model

Our Institution's Animal Care and Use Committee approved all animal procedures. Female athymic nude mice (n = 38, 4-6 weeks, Harlan, Indianapolis, IN) were implanted with 0.72 mg, 60-day release, 17β-estradiol pellets (Innovative Research of America, Sarasota, FL). Twenty-four hours later, approximately 10^7 BT474 or HR6 cells, suspended in a 1:10 ratio of growth factor-reduced Matrigel and IMEM, were injected subcutaneously into the right flank. Tumor volumes were measured once per week *via* calipers, and experiments commenced once tumor volumes reached > 200 mm^3 (typically 4 to 6 weeks post cell injection). A 26-gauge jugular catheter was surgically implanted for radiotracer delivery. Mice were anesthetized with 2% isoflurane in pure oxygen mixture for all surgical procedures.

Trastuzumab Treatment Study

Mice bearing tumors were grouped into four cohorts: trastuzumab and vehicle treated BT474 cohorts, and trastuzumab and vehicle treated HR6 cohorts. The number of mice for each cohort and time point is displayed in Table IX-1. For treatment, mice were

administered trastuzumab (10 mg/kg) or saline vehicle by i.p. (total volume, 100 mL) twice within four days. DCE-MRI was conducted at baseline and days 1 and 4, which were 24 hours post the first and second treatments, respectively. Figure IX-1 illustrates the imaging and dosing schedule for the trastuzumab treatment study.

Table IX-1. Tabulated list of animal number for each cohort and time point

Time point	BT474 treated	BT474 control	HR6 treated	HR6 control
Baseline	11	9	9	9
Day 1	11	9	9	9
Day 4	9	8	8	9

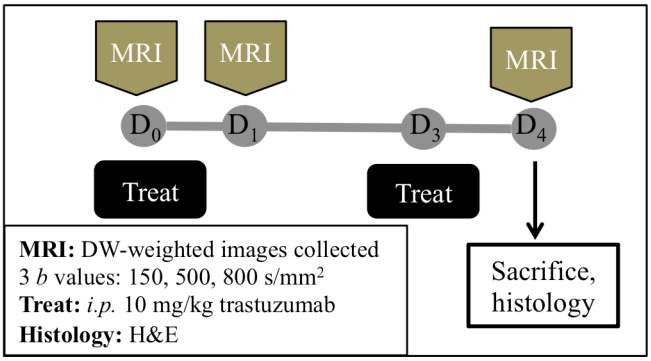

Figure IX-1. Longitudinal imaging and trastuzumab treatment study schema. Mice were treated twice in four days with either trastuzumab (10 mg/kg) or saline vehicle. DW-MRI data were acquired at baseline and 24 hours post the first and second treatments.

Volumetric Imaging and Analysis

All MRI data was collected using a 7T MRI scanner (Agilent Technologies (formally Varian), Palo Alto, CA) equipped with a 38-mm quadrature RF coil (Doty Scientific, Columbia, SC). Anesthesia was induced and maintained *via* 2% isoflurane in pure oxygen. Animal respiration rate was monitored, and animal body temperature was maintained at an external temperature of 32 ^{o}C by means of a flow of warm air directly into the bore of the magnet. Each animal was placed in a custom built restraint, and the

tumor region was first localized *via* 3D gradient echo scout images. Longitudinal tumor volume was measured from T_2-weighted images; T_2-weighted images covering the entire tumor volume were acquired using a fast spin-echo pulse sequence with the following parameters: TR = 5500 ms, effective TE = 35.6 ms, 1 mm slice thickness, and an acquisition matrix of 128 × 128 over a 28 × 28 mm^2 field of view yielding a voxel size of 0.22 × 0.22 × 1 mm^3. Data were imported into MATLAB® version R2010b (The MathWorks, Natick, MA), and tumor volumes were measured at each time point by manually drawing regions of interest (ROIs) along tumor boundaries from all slices consisting of tumor tissue. I delineated all tumor ROIs to ensure consistency.

DW-MRI Data Acquisition

After volumetric imaging, anesthesia was continued and diffusion-weighted images were acquired using a standard pulsed gradient spin echo sequence with three *b* values (150, 500, and 800 s/mm^2) and gradients applied simultaneously along the three orthogonal directions (*x*, *y*, and *z*). Scan acquisition parameters were: TR/TE = 2000/30 ms, gradient duration δ = 3 ms, gradient interval Δ = 20 ms, two signal excitations, and an acquisition matrix of 64 × 64 over a 28 × 28 mm^2 field of view yielding a voxel size of 0.44 × 0.44 mm^2. Multiple 1 mm thick slices with a 1 mm gap were acquired over the entire tumor region. Image acquisition was triggered with respiration and navigator corrected (12) to reduce image artifacts due to bulk motion.

DW-MRI Data Analysis

To construct an ADC parametric map, signal intensities from images acquired at three *b* values were fit for each image voxel using a nonlinear least squares optimization method to Eq. (IX-1):

$$S(b) = S_0 \cdot exp(-\mathrm{ADC} \cdot b), \quad \text{(IX-1)}$$

where S_0 and $S(b)$ are the signal intensities before and after application of diffusion gradients, respectively. As we did not acquire images without application of diffusion gradients (i.e., $b = 0$), S_0 was a free parameter in our optimization routine. The ROIs used for the tumor volume measurements were downsampled to match the image resolution of the DW-MRI data. Both the mean and median ADC were quantified from multiple slices across the tumor volume. To ensure DW-MRI data integrity, a water phantom was imaged simultaneously with the animal in each imaging session. If a tumor slice had a water phantom ADC value outside the range of 2.65×10^{-3} $mm^2/s \pm 15\%$ (ADC value of free water at 32^{o} C; linearly interpolated from reference (13)), then the tumor ADC slice was not used in the tumor analysis. All data analysis methods were performed in MATLAB® version R2010b.

Removing Necrosis

It is well known that regions of necrosis have increased ADC values (8,14), which will systematically bias the summary statistics (i.e., mean and median) of the whole tumor ROIs towards higher ADC values. To remove the potential affects of necrosis from the ADC measurements, necrotic regions identified as low perfused regions from contrast-enhanced MR images were removed from the ADC analysis.

Serial, contrast-enhanced MRI data were acquired using a spoiled gradient echo sequence at a temporal resolution of 12.8 seconds for ~20 minutes with the following parameters: TR/TE /a = 100 ms/TE = 2.1 ms / 25°, NEX = 2, and the same acquisition matrix and FOV as the DW-MRI data. A bolus of 0.05 mmol/kg Gd-DTPA was delivered *via* a jugular catheter using an automated syringe pump (Harvard Apparatus, Holliston, MA) at a rate of 2.4 mL/min after 11 images of baseline (~ 2 minutes) were acquired. The slope of the dynamic signal intensity time course from each voxel was calculated from the average value of the baseline images to the signal intensity value at 60 seconds post injection (see Figure IX-2). If the slope was less than 20%, the voxel is determined to be poorly perfused and removed from the tumor ADC analysis.

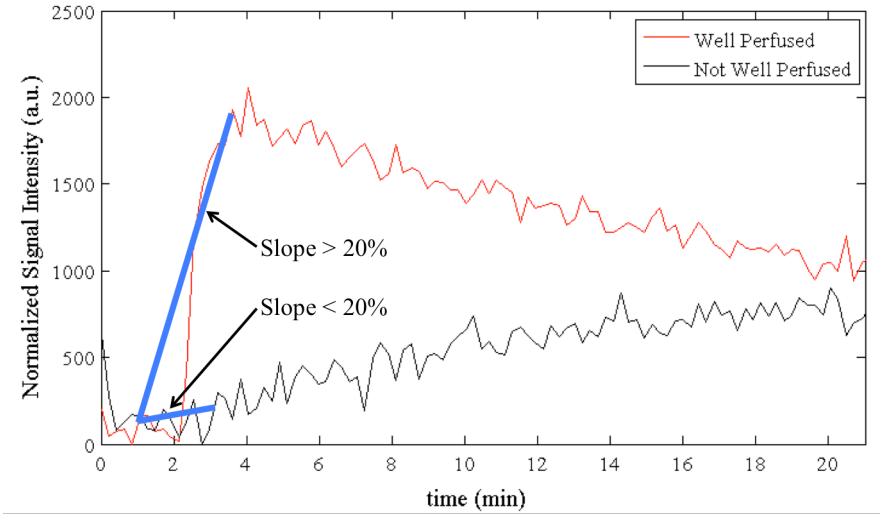

Figure IX-2. Examples of contrast-enhanced dynamic time courses of a well perfused (red line) and not well perfused (black line) voxels. The slope (blue line) is illustrated from the mean of the baseline images to the signal intensity at 60 seconds post injection.

Histological Analysis

Immediately following imaging at day 4, animals were sacrificed and excised tumors were fixed in 10% formalin for at least 24 hours. Samples were then transferred to

70% ethanol and stored in 4 °C. Samples were blocked in paraffin and sectioned with 4-micron thick slices before processing with hematoxylin and eosin (H&E). Stained sections were imaged at 20× magnification using a Leica SCN400 Slice Scanner (Leica, Buffalo Grove, IL). Unbiased and automated image analysis was performed with associated software packages that use trained algorithms based on shape and intensity of the stain. Cell density was quantified from H&E stained sections by counting the total number of cells and dividing it by the area of the tissue section.

Statistics

Three statistical comparisons were performed in this study: 1) trastuzumab versus vehicle treated BT474 cohorts, 2) trastuzumab versus vehicle treated HR6 cohorts, and 3) responders (BT474 treated) versus nonresponders (HR6 treated). Longitudinal ADC values were compared within and between cohorts at each time point. Cell density quantified from H&E data were compared between cohorts at day 4. All data are presented as mean ± standard error (SE). All statistical comparisons were evaluated using the nonparametric Wilcoxon rank sum test in MATLAB version 2010b, and differences were considered significant if $p < 0.05$.

Results

Impact of Trastuzumab on Tumor Xenograft Growth

Longitudinal tumor volumes for the trastuzumab and vehicle treated BT474 cohorts are displayed in Figure IX-3A. There was no statistically significant difference in tumor volume between these cohorts at baseline ($p = 0.76$) or day 1 ($p = 0.76$); however,

a trend towards significance was observed at day 4 (p = 0.09). In the vehicle treated group, tumor growth steadily increased over time yet differences after treatment were not statistically significant compared to baseline (day 1: p = 0.80, +1.82% ± 1.23% compared to baseline; day 4: p = 0.32, +7.67% ± 4.44% compared to baseline). While Trastuzumab treatment inhibited tumor growth, the difference in tumor volume was not statistically significant at day 1 (p = 0.60, -4.98% ± 2.19% compared to baseline), and only trended towards significance at day 4 (p = 0.09, -26.5% ± 6.02% compared to baseline).

Longitudinal tumor volumes for the trastuzumab and vehicle treated HR6 cohorts are displayed in Figure IX-3B. No statistically significant difference in tumor volume was observed between these cohorts at the measured timed points (baseline: p = 0.13; day 1: p = 0.13; day 4: p = 0.23). In the vehicle treated group, tumor growth steadily increased over time yet differences after treatment were not statistically significant compared to baseline (day 1: p = 0.60, +8.32% ± 1.94% compared to baseline; day 4: p = 0.44, +15.2% ± 3.26% compared to baseline). In the trastuzumab treated group, tumor growth also steadily increased over time yet differences after treatment were not statistically significant (day 1: p = 0.86, +3.29% ± 1.59% compared to baseline; day 4: p = 1.00, +5.61% ± 5.16% compared to baseline).

To evaluate the impact of trastuzumab on tumor xenografts with different trastuzumab sensitivities, longitudinal tumor volume within the trastuzumab treated BT474 (responder) and HR6 (nonresponder) cohorts are compared in Figure IX-3C. Similar to the other cohort comparisons, difference in tumor volume between responders and nonresponders was not statistically significant at baseline (p = 0.40) or day 1 (p = 0.22), though it trended towards significance at day 4 (p = 0.06).

DW-MRI Evaluation of Treatment Response in BT474 Xenografts

An ADC parametric map from a representative animal from each trastuzumab and vehicle treated BT474 cohort is displayed in Figure IX-4A. The median ADC values and the percent change in median ADC are displayed in Figures IX-3B and 3C, respectively. No statistical difference in median ADC was observed between the trastuzumab and vehicle treated cohorts at any measured time point (Figure IX-3B; baseline: $p = 0.22$; day 1: $p = 0.94$; day 4: $p = 0.54$). Additionally, the percent change in median ADC at either time point after baseline was not statistically different between cohorts (Figure IX-3C; day 1: $p = 0.54$; day 4: $p = 0.89$). In the trastuzumab treated group, non-significant increases in ADC were observed at day 1 ($p = 0.84$) and day 4 ($p = 0.13$). In the vehicle treated group, a non-significant increase in ADC was also observed at day 1 ($p = 0.34$) followed by another increase that trended towards significance at day 4 ($p = 0.07$). The graphical representation and results from the statistical comparisons for the mean ADC were similar to the median ADC, and thus not shown.

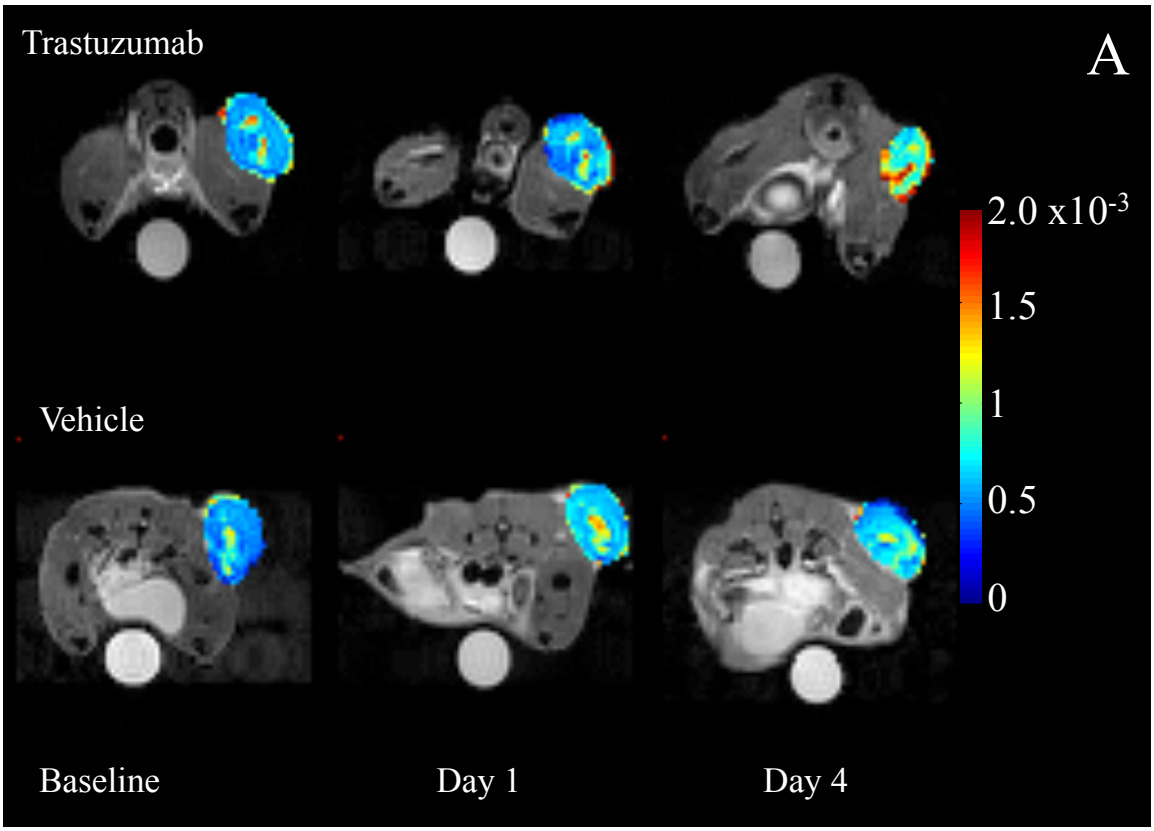

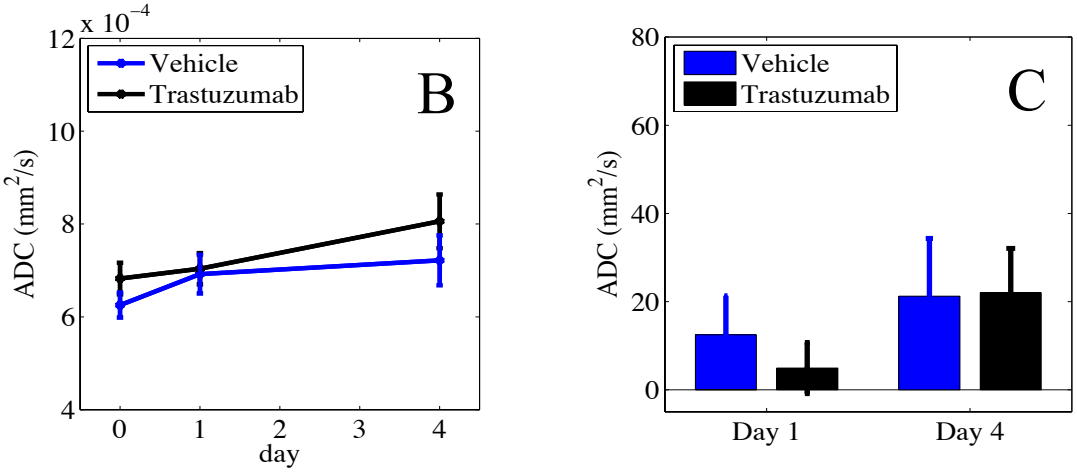

Figure IX-3. ADC parametric maps are displayed for a representative animal from each trastuzumab and vehicle treated BT474 cohort (A). No statistically significant differences in longitudinal ADC values between the cohorts (B). The percent change (compared to baseline) in ADC was not statistically significant between cohorts at day 1 or day 4 (C). The units for ADC are mm^2/s.

DW-MRI Evaluation of Treatment Response Between HR6 Xenografts

An ADC parametric map from a representative animal from each trastuzumab and vehicle treated HR6 cohort is displayed in Figure IX-4A. The median ADC values and the percent change in median ADC are displayed in Figures IX-4B and 4C, respectively. No statistical difference in median ADC was observed between the trastuzumab and vehicle treated cohorts at any measured time point (Figure IX-4B; baseline: $p = 0.13$; day 1: $p = 0.93$; day 4: $p = 0.89$). Additionally, the percent change in median ADC at either time point after baseline was not statistically different between cohorts (Figure IX-4C; day 1: $p = 0.39$; day 4: $p = 0.24$). In the trastuzumab treated group, a non-significant increase in ADC was observed at day 1 ($p = 0.19$, +11.6% ± 4.36% compared with baseline) followed by a significant increase in ADC at day 4 ($p = 0.006$). In the vehicle treated group, non-significant increases in ADC were observed at day 1 ($p = 0.67$) and day 4 ($p = 0.26$). The graphical representation and results from the statistical comparisons for the mean ADC were similar to the median ADC, and thus not shown.

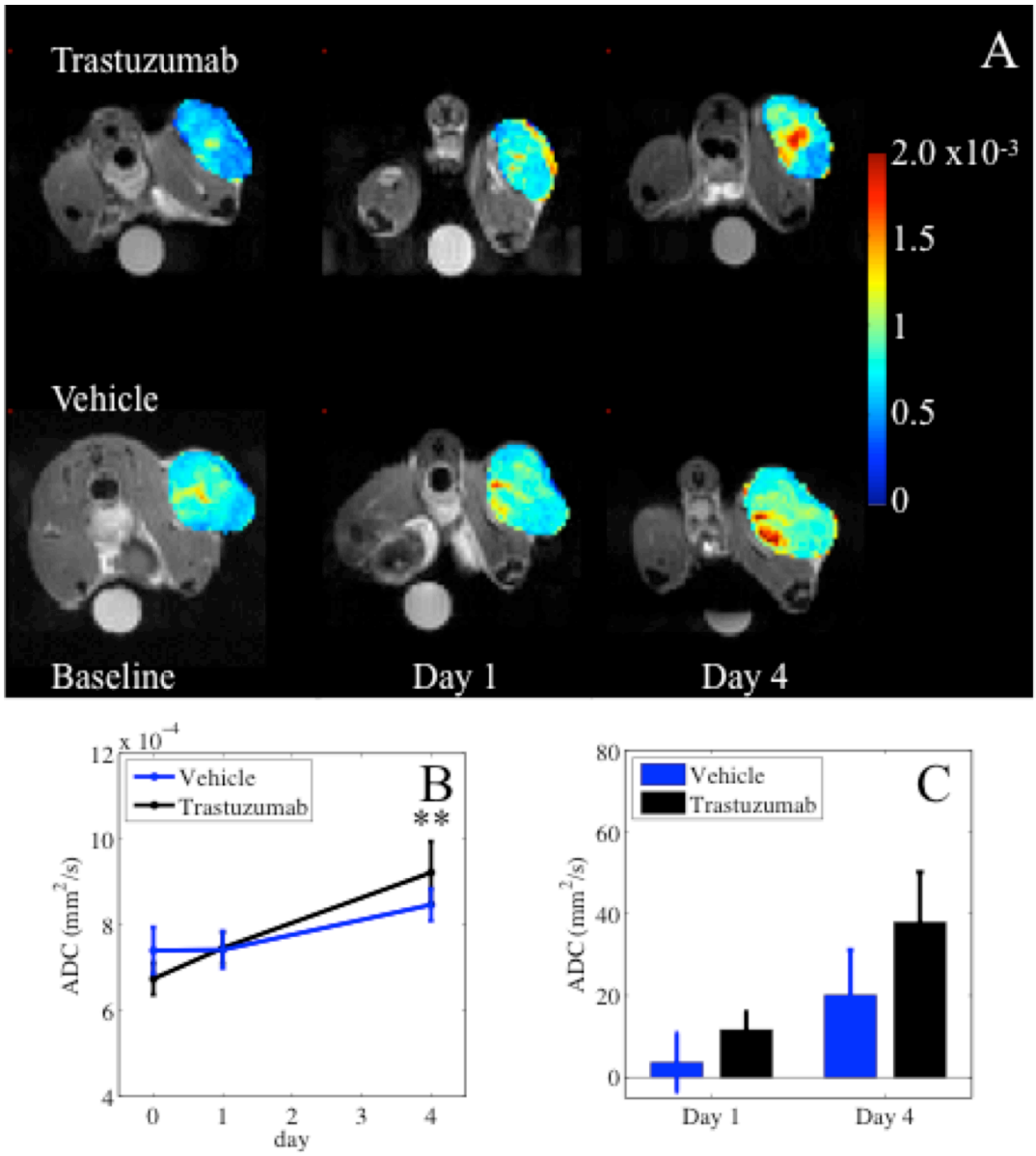

Figure IX-4 ADC parametric maps are displayed for a representative animal from each trastuzumab and vehicle treated HR6 cohort (A). No statistically significant differences in longitudinal ADC values between the cohorts (B). The percent change (compared to baseline) in ADC was not statistically significant between cohorts at day 1 or day 4 (C). The units for ADC are mm^2/s. ** $p < 0.01$

DW-MRI Evaluation of Treatment Response Between Responders and Nonresponders

No statistical difference in median ADC was observed between the trastuzumab and vehicle treated cohorts at any measured time point (baseline: $p = 0.93$; day 1: $p =$

0.45; day 4: $p = 0.28$). Additionally, the percent change in median ADC at either time point after baseline was not statistically different between cohorts (day 1: $p = 0.45$; day 4: $p = 0.54$). The results from the statistical comparisons for the mean ADC were similar to the median ADC and thus not shown.

DW-MRI Evaluation of Treatment Response After Necrosis Segmentation

It can be noted from the ADC parametric maps illustrated in Figures IX-3 and 4 that regions of necrosis develop over time in the vehicle treated BT474 group as well as both of the HR6 cohorts. Necrotic voxels that were poorly perfused (determined from the contrast-enhanced MRI data) were removed, and mean and median ADC values were again calculated from the resulting tumor voxels. Serial, contrast-enhanced MR images were not collected for all mice; thus, the number of mice used for the ADC comparison after necrosis segmentation is tabulated in Table IX-2.

Table IX-2. Tabulated list of animal number used in the ADC comparison after necrosis removal

Time point	BT474 treated	BT474 control	HR6 treated	HR6 control
Baseline	7	5	5	8
Day 1	7	5	5	8
Day 4	5	4	5	7

The median ADC values after necrosis segmentation are displayed for each cohort comparison in Figure IX-5. The longitudinal results for median ADC were relatively unchanged after necrosis segmentation; the only different result being that the median ADC between trastuzumab and vehicle treated HR6 cohorts at baseline trended towards significance ($p = 0.05$). Results from the statistical analysis are tabulated in Tables IX-3

and 4 for the within and between cohort comparison, respectively. The graphical representation and results from the statistical comparisons for the mean ADC were again similar to the median ADC, and thus not shown.

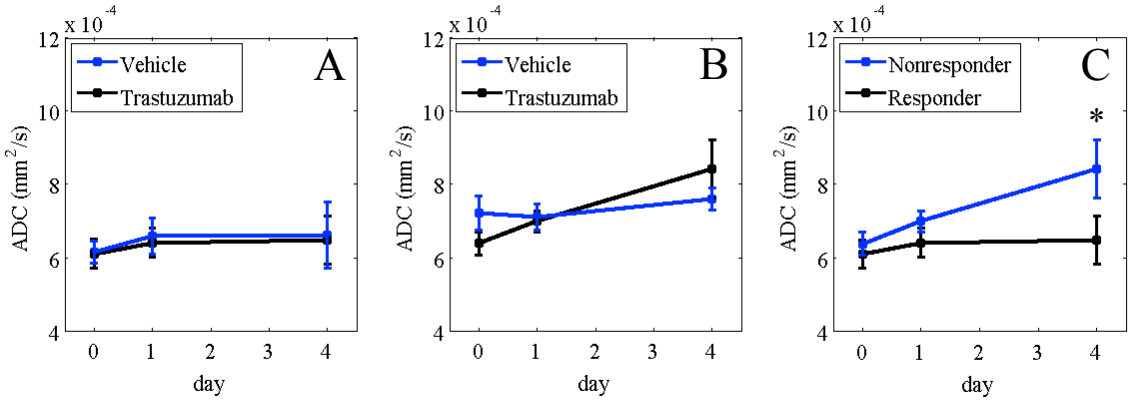

Figure IX-5. Longitudinal median ADC after necrosis segmentation for the trastuzumab and vehicle treated BT474 cohorts (A), trastuzumab and vehicle treated HR6 cohorts (B), and the responders and nonresponders (C). The median ADC of the HR6 treated cohort (i.e., nonresponder) increased significantly at day 4 compared to baseline (*$p = 0.03$).

Table IX-3. The *p* values from the statistical comparison between cohorts

Time point	BT474	HR6	Responder vs Nonresponder
Baseline	0.89	0.05	0.77
Day 1	0.70	0.78	0.86
Day 4	1.00	0.66	0.27

Table IX-4. The *p* values from the statistical comparison within each cohort

Time point	BT474 treated	BT474 control	HR6 treated	HR6 control
Day 1	0.55	0.42	0.24	0.44
Day 4	0.54	0.56	**0.03**	0.86

Histological Evaluation of Cell Density

Representative H&E stained tissues sections at 20× magnification are displayed in for a representative animal from each BT474 and HR6 cohort in the top and bottom rows,

respectively, in Figure IX-6. A significant difference in cell density was not observed between BT474 cohorts (Figure IX-7A), which supported the non-significant difference in ADC at day 4 (Figure IX-3B). Although the difference in cell density was not statistically different, the trend in the measurements appears to correlate inversely with ADC at day 4 (Figure IX-3B). A significant difference in cell density was not observed between HR6 cohorts (Figure IX-7B), which supported the non-significant difference in ADC at day 4 (Figure IX-4B). Additionally, the difference in cell density is not statistically significant between the responders (BT474 treated) and the nonresponders (HR6 treated) (Figure IX-7C), which also corresponds with the comparison the *in vivo* ADC data between these cohorts. Note from the H&E stained tissue sections that both the HR6 groups appear to have a lower number of cells than the BT474 groups; this observation is reflected in the cell density measurements displayed in the bar graphs. Furthermore, the cell density of the vehicle treated BT474 group is significantly greater than the trastuzumab and vehicle treated HR6 groups ($p = 0.01$).

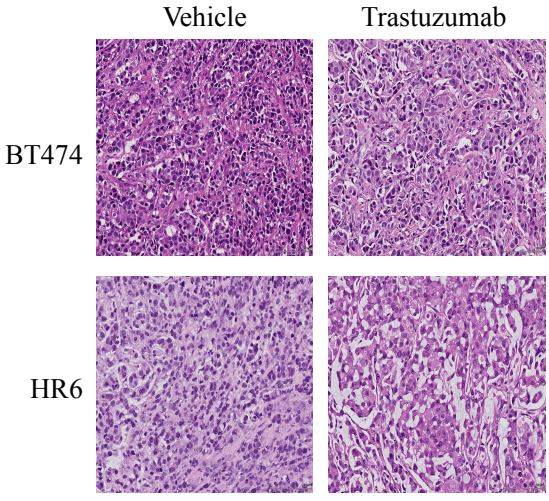

Figure IX-6. Representative examples of H&E stained tissue sections imaged at 20× magnification are displayed from one animal in each cohort. Note how the cell packing from each of the HR6 cohorts appears to be less when compared to the BT474 cohorts.

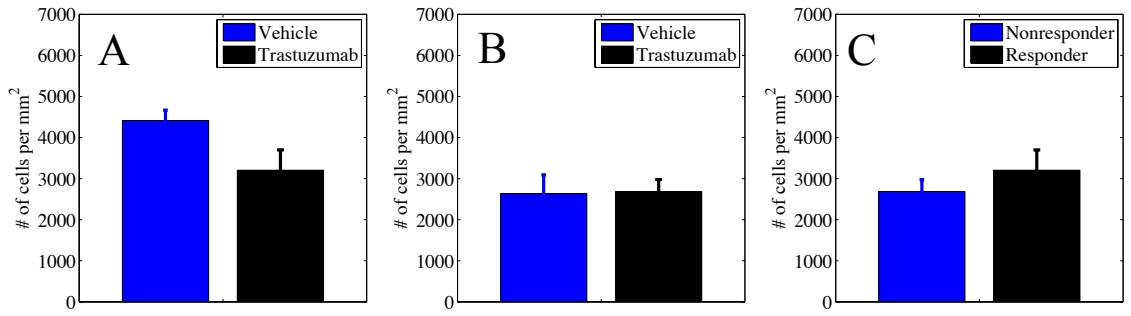

Figure IX-7. Cell density comparison between trastuzumab and vehicle treated BT474 and HR6 cohorts. A significant difference in cell density was not observed between BT474 groups (A). However, note that the trend in cell density appears to inversely correlate with ADC at day 4 (Figure IX-4B). A significant difference in cell density was not observed between HR6 groups (B). The lower cell packing of the HR6 cohorts is reflected in the lower cell density measurements of both HR6 cohorts compared to the BT474 cohorts. The significant difference in cell density between responders and nonresponders was not statistically significant (C), however the trend correlates with the longitudinal ADC illustrated in Figure IX-6C.

Discussion

In recent years, there has been considerable growth in the number of quantitative functional and molecular imaging biomarkers that are capable of providing noninvasive measurements of treatment-induced changes. DW-MRI is an emerging technique where the derived imaging parameters (e.g., ADC) have been shown to correlate with cellular density (3,15,16). As a hallmark of cancer is uncontrolled tumor growth leading to high cell density and loss of normal cytoarchitecture (4), DW-MRI could potentially provide an early biomarker of biological abnormality. However, before a biomarker, such as ADC, can be used in routine clinical assessments of disease response, a systematic evaluation in a variety of cancer models and treatment regimens are required. Thus, the objective of this study was to evaluate the utility of DW-MRI to provide an early response assessment in two HER2+ human breast cancer xenografts exposed to trastuzumab.

The results of this study indicate that DW-MRI is not sensitive to trastuzumab-induced changes in the trastuzumab-sensitive BT474 mouse model of human breast cancer. The main mechanism of action of trastuzumab is the inhibition of cell signaling pathways leading to cellular proliferation and survival. Thus, a plausible hypothesis would be that the ADC derived from DW-MRI measurements will increase with effective treatment. However, we observed practically no change (after removing necrotic voxels) in longitudinal ADC in both the trastuzumab and vehicle treated BT474 cohorts. This result could be due to two things: 1) the imaging time points employed in this study were not optimal to catch the transient nature of treatment-induced changes in ADC (14), or 2) another observed mechanism of action is the antibody-dependent cell-mediated cytotoxicity (ADCC) effect where trastuzumab interacts with specific immune cells initiating infiltration of natural killers and macrophages that cause inflammation (17).

The optimal imaging time points for this study were set based on tumor volume changes, as one of the study objectives was to evaluate ADC as an early marker of response before significant changes in tumor size are observed. However, the optimal timing window to observe trastuzumab-induced changes in tumor ADC might be earlier or later than 24 hours post one cycle of therapy. For example, Thoeny et al. quantified ADC at 1 hour, 6 hours, 2 days, and 9 days after therapy and observed significant decreases in tumor ADC at the 1 and 6 hour time points, which is indicative of increased cell swelling, respectively (18). An increase in ADC at the 2-day follow-up suggests that progressive necrosis is forming. ADC decreased at the 9-day follow-up, which is consistent with tumor relapse resulting in a reorganization of the tumor cytoarchitecture (18). If data were not acquired at any one of the imaging time points in the highlighted

study, then the transient nature of ADC in response to treatment would not be fully characterized.

The ADCC phenomenon has mainly been observed in patients (or animals) with intact immune systems. In mice with suppressed natural killers cell function, trastuzumab demonstrated only a 29% reduction in tumor growth compared to 96% reduction in control mice with intact natural killer cell function (19). Clinical data has shown a higher *in situ* infiltration of leukocytes in patients who achieved complete or partial remission with neoadjuvant trastuzumab relative to those who did not respond (20). If trastuzumab interacts with the immune cells resulting in an influx of macrophages, this would cause a decrease in tumor ADC. However, this influx of macrophages also causes inflammation resulting in an ADC increase. In this situation, the overall median (or mean) tumor ADC may not change significantly. However, one would argue that this effect is minimal in mice with compromised immune systems. The mice used in this study are athymic, meaning that they lack T-cells; the immune effect from natural killer cells remains unchanged. Thus, the ADCC phenomenon could be occurring in these animals and affecting our observed ADC measurements.

We observed very interesting results when comparing longitudinal ADC between the trastuzumab and vehicle treated cohorts, as well as, between responders (BT474 treated) and nonresponders (HR6 treated). Tumor volume and ADC increased over time in both HR6 cohorts. This result was unexpected considering that previous studies observed an inverse relationship between tumor volume and ADC (2,5,21). The volumes of some of the HR6 xenografts were quite large resulting in regions of necrosis at baseline. Additionally, the necrotic volumes increased over the course of the study (e.g.,

see Figure IX-5), thus biasing the mean or median tumor ADC toward higher values. The effect of necrosis on tumor ADC has previously been observed in xenograft studies, and the authors used the signal intensity from T_2-weighted images to remove necrotic voxels (5). Thus, we also used an additional imaging technique to remove necrosis; we removed necrosis based on tumor perfusion from contrast-enhanced MRI data.

Removing necrosis did not seem to have any effect as the tumor ADC values from both the trastuzumab and vehicle treated HR6 cohorts still increased compared to baseline. The next step was to investigate the histology to see if the observed imaging result was in fact true and representative of the underlying biology. It can be observed from Figure IX-7 that the H&E tissue sections of both the HR6 cohorts appear to be less densely packed with cells compared to the BT474 groups. This qualitative assessment is supported, as the cell density is lower in both HR6 groups compared to the BT474 groups (Figure IX-8). In fact, the cell density of the trastuzumab and vehicle treated HR6 cohorts was significantly lower than the vehicle treated BT474 group ($p < 0.05$). These results suggest that the observed *in vivo* ADC values are reflecting the underlying biology.

Study Limitations

The optimal imaging time points for this study were determined from a separate group of trastuzumab and vehicle treated mice with BT474 xenografts (see Chapter VI). Although a significant difference in tumor volume was observed at day 4 in the previous study, treatment-induced differences in tumor volume were not statistically different at day 4 in the current study. Thus, due to the variability of mouse physiology and treatment efficiency, a true study endpoint based on tumor size changes was not achieved. This is

not ideal, especially in studies that are evaluating if an imaging parameter is a biomarker of early treatment response.

The segmentation method (i.e, slope of the dynamic contrast-enhanced signal intensity time course) used in study to remove necrotic voxels may not be the most optimal technique. We assumed that if a voxel is not well perfused, that it is not viable and removed it from the ADC analysis. This may or may not be a valid assumption in tumors as voxels could contain viable cells but not functioning tumor vasculature. A more sophisticated analysis of the perfusion data would be clustering the dynamic curves into groups using, for example, a *k-mean*s clustering algorithm (22). This technique would group the voxels with similar dynamic time courses in order to provide a better means of segmentation than the wash-in slope, which was calculated in this study.

Another means of necrotic segmentation would be to compute functional diffusion maps between the imaging time points, as the change in ADC between time points should be minimal in necrotic regions (14). This method, however, requires longitudinal registration between imaging time points, which is not feasible with the current imaging set-up.

Conclusion

The results from this study suggest that DW-MRI does not provide an early biomarker of response in trastuzumab sensitive or resistant xenografts exposed to trastuzumab. However, we showed that a parameter derived from DW-MRI data (i.e., ADC) does reflect the underlying tumor biology. The latter result is just as important as the treatment response evaluation as it provides validation for the current *in vivo* imaging

technique in order to assist in the interpretation of imaging findings from future treatment response studies.

References

1. Padhani AR, Liu G, Koh DM, Chenevert TL, Thoeny HC, Takahara T, Dzik-Jurasz A, Ross BD, Van Cauteren M, Collins D, Hammoud DA, Rustin GJ, Taouli B, Choyke PL. Diffusion-weighted magnetic resonance imaging as a cancer biomarker: consensus and recommendations. Neoplasia 2009;11(2):102-125.
2. Loveless ME, Lawson D, Collins M, Nadella MV, Reimer C, Huszar D, Halliday J, Waterton JC, Gore JC, Yankeelov TE. Comparisons of the efficacy of a Jak1/2 inhibitor (AZD1480) with a VEGF signaling inhibitor (cediranib) and sham treatments in mouse tumors using DCE-MRI, DW-MRI, and histology. Neoplasia 2012;14(1):54-64.
3. Anderson AW, Xie J, Pizzonia J, Bronen RA, Spencer DD, Gore JC. Effects of cell volume fraction changes on apparent diffusion in human cells. Magn Reson Imaging 2000;18(6):689-695.
4. Li SP, Padhani AR. Tumor response assessments with diffusion and perfusion MRI. J Magn Reson Imaging 2012;35(4):745-763.
5. Aliu SO, Wilmes LJ, Moasser MM, Hann BC, Li KL, Wang D, Hylton NM. MRI methods for evaluating the effects of tyrosine kinase inhibitor administration used to enhance chemotherapy efficiency in a breast tumor xenograft model. J Magn Reson Imaging 2009;29(5):1071-1079.
6. Larocque MP, Syme A, Allalunis-Turner J, Fallone BG. ADC response to radiation therapy correlates with induced changes in radiosensitivity. Med Phys 2010;37(7):3855-3861.
7. Lee SC, Poptani H, Pickup S, Jenkins WT, Kim S, Koch CJ, Delikatny EJ, Glickson JD. Early detection of radiation therapy response in non-Hodgkin's lymphoma xenografts by in vivo 1H magnetic resonance spectroscopy and imaging. NMR Biomed 2010;23(6):624-632.
8. Thoeny HC, Ross BD. Predicting and monitoring cancer treatment response with diffusion-weighted MRI. J Magn Reson Imaging 2010;32(1):2-16.
9. Galban CJ, Chenevert TL, Meyer CR, Tsien C, Lawrence TS, Hamstra DA, Junck L, Sundgren PC, Johnson TD, Galban S, Sebolt-Leopold JS, Rehemtulla A, Ross BD. Prospective analysis of parametric response map-derived MRI biomarkers: identification of early and distinct glioma response patterns not predicted by standard radiographic assessment. Clin Cancer Res 2011;17(14):4751-4760.
10. Sun YS, Zhang XP, Tang L, Ji JF, Gu J, Cai Y, Zhang XY. Locally advanced rectal carcinoma treated with preoperative chemotherapy and radiation therapy: preliminary analysis of diffusion-weighted MR imaging for early detection of tumor histopathologic downstaging. Radiology 2010;254(1):170-178.
11. Ritter CA, Perez-Torres M, Rinehart C, Guix M, Dugger T, Engelman JA, Arteaga CL. Human breast cancer cells selected for resistance to trastuzumab in vivo overexpress epidermal growth factor receptor and ErbB ligands and remain dependent on the ErbB receptor network. Clin Cancer Res 2007;13(16):4909-4919.
12. Anderson AW, Gore JC. Analysis and correction of motion artifacts in diffusion weighted imaging. Magn Reson Med 1994;32(3):379-387.

13. Mills R. Self-Diffusion in Normal and Heavy Water in the Range of 1-45 degrees. The Journal of Physical Chemistry 1973;77(5).
14. Moffat BA, Chenevert TL, Lawrence TS, Meyer CR, Johnson TD, Dong Q, Tsien C, Mukherji S, Quint DJ, Gebarski SS, Robertson PL, Junck LR, Rehemtulla A, Ross BD. Functional diffusion map: a noninvasive MRI biomarker for early stratification of clinical brain tumor response. Proc Natl Acad Sci U S A 2005;102(15):5524-5529.
15. Zhai G, Grubbs CJ, Stockard CR, Umphrey HR, Beasley TM, Kim H. Diffusion Weighted Imaging Evaluated the Early Therapy Effect of Tamoxifen in an MNU-Induced Mammary Cancer Rat Model. PLoS One 2013;8(5):e64445.
16. Gibbs P, Liney GP, Pickles MD, Zelhof B, Rodrigues G, Turnbull LW. Correlation of ADC and T2 measurements with cell density in prostate cancer at 3.0 Tesla. Invest Radiol 2009;44(9):572-576.
17. Kohrt HE, Houot R, Marabelle A, Cho HJ, Osman K, Goldstein M, Levy R, Brody J. Combination strategies to enhance antitumor ADCC. Immunotherapy 2012;4(5):511-527.
18. Thoeny HC, De Keyzer F, Chen F, Ni Y, Landuyt W, Verbeken EK, Bosmans H, Marchal G, Hermans R. Diffusion-weighted MR imaging in monitoring the effect of a vascular targeting agent on rhabdomyosarcoma in rats. Radiology 2005;234(3):756-764.
19. Clynes RA, Towers TL, Presta LG, Ravetch JV. Inhibitory Fc receptors modulate in vivo cytotoxicity against tumor targets. Nat Med 2000;6(4):443-446.
20. Gennari R, Menard S, Fagnoni F, Ponchio L, Scelsi M, Tagliabue E, Castiglioni F, Villani L, Magalotti C, Gibelli N, Oliviero B, Ballardini B, Da Prada G, Zambelli A, Costa A. Pilot study of the mechanism of action of preoperative trastuzumab in patients with primary operable breast tumors overexpressing HER2. Clin Cancer Res 2004;10(17):5650-5655.
21. Reichardt W, Juettner E, Uhl M, Elverfeldt DV, Kontny U. Diffusion-weighted imaging as predictor of therapy response in an animal model of Ewing sarcoma. Invest Radiol 2009;44(5):298-303.
22. Fluckiger JU, Schabel MC, Dibella EV. Model-based blind estimation of kinetic parameters in dynamic contrast enhanced (DCE)-MRI. Magn Reson Med 2009;62(6):1477-1486.

CHAPTER X

CONCLUSION

The standard-of-care radiographic response assessment is based on one-dimensional changes in tumor size. With the development of anticancer therapies that induce molecular changes that would occur substantially sooner than changes in morphology, one-dimensional assessments of response may not be the most sensitive or accurate approach. Functional and molecular imaging techniques that provide quantitative assessments of tumors could have a fundamental role in oncology as they have the ability to noninvasively measure specific molecular changes of the tumor. Much progress has been made to improve the quality of information available from functional and molecular imaging techniques in order to noninvasively measure tumor growth, assess tumor status, and predict treatment response. Obstacles have inhibited translation of many functional and molecular imaging techniques into routine clinical practice; thus, a need exists to further develop quantitative imaging techniques that can report on specific characteristics of cancer in order to improve patient care.

This work has developed standardized experimental protocols for several small-animal PET and MRI techniques, as well as, assessed protocol reproducibility. This work also evaluated the application of several current and emerging PET and MRI techniques to assess early treatment response in HER2+ breast cancer models exposed to trastuzumab. The application of PET and MRI to differentiate between two HER2+ models with varying degrees of trastuzumab sensitivity was also investigated. Lastly, the

parameters derived from the image data were compared to histology in order to examine the relationship between the *in vivo* imaging data and the underlying biology.

This work has shown that small-animal imaging techniques with ^{18}F-FDG PET, ^{18}F-FLT PET, ^{18}F-FMISO PET, and DW-MRI are reproducible and can be reliably employed in treatment response studies. Furthermore, this work quantified thresholds where changes greater than this value would reflect changes in tumor physiology and not measurement error in a group or individual analysis.

With the observation that trastuzumab inhibits cell signaling pathways leading to cellular proliferation and survival, as well as, angiogenesis, this work examined the ability of ^{18}F-FLT PET, DCE-MRI, and DW-MRI to provide early response assessments of HER2+ breast cancer models that are sensitive and resistant to trastuzumab. This work showed that ^{18}F-FLT PET and DCE-MRI provided early biomarkers of response in trastuzumab sensitive xenografts. This work also showed that ^{18}F-FLT PET differentiates responders (trastuzumab-sensitive) from nonresponders (trastuzumab-resistant) when exposed to trastuzumab. In the context of this study, parameters derived from DW-MRI data were not sensitive to trastuzumab-induced changes in HER2+ xenografts.

The histological correlates for ^{18}F-FLT PET (e.g., Ki67) and DCE-MRI (e.g., microvessel density quantified *via* CD31 staining) corresponded with the *in vivo* imaging data, thereby providing some validation for the observed treatment-induced changes in the trastuzumab sensitive xenografts. The observed trend in the histological measurements corresponded with the imaging data from the responder and nonresponder comparison, however the differences in the histology measurements were not statistically significant. Although DW-MRI was not sensitive to trastuzumab response in this study,

the cell density measurements from histology corresponded with the DW-MRI data suggesting that measurements of cell density from DW-MRI reflected the underlying biology of tumor.

Overall, these contributions have aided in the development, implementation, and interpretation of future treatment response studies. This work has created a paradigm by which other imaging protocols as well as current and emerging breast cancer treatments might be evaluated.